Technische Universität München
Max-Planck-Institut für Quantenoptik

Applications of tensor networks to open problems in many-body quantum physics

Giacomo Giudice

Vollständiger Abdruck der von der Fakultät für Physik der Technischen Universität München zur Erlangung des akademischen Grades eines

Doktors der Naturwissenschaften (Dr. rer. nat.)

genehmigten Dissertation.

Vorsitzender	Prof. Dr. Rudolf Gross
Prüfende der Dissertation	Hon. Prof. Dr. J. Ignacio Cirac Prof. Dr. Michael Knap

Die Dissertation wurde am 22.09.2022 bei der Technischen Universität München eingereicht und durch die Fakultät für Physik angenommen.

Abstract

Quantum mechanics tells us how to describe systems in terms of equations, but not how to solve them. For typical many-body quantum systems, solving these equations becomes an incredibly challenging task. The number of degrees of freedom blows up exponentially with the number of constituents, which makes it extremely hard to study strongly correlated phenomena—such as high-temperature superconductivity or the fractional quantum Hall effect.

In the last decades, *tensor networks* have emerged as a new class of methods to study strongly-correlated systems in low-dimensional lattices. Tensor networks have led to powerful numerical algorithms, but also provide a language to analytically understand such systems. In this dissertation, we use the framework of tensor networks to propose new algorithmic ideas, and we apply it to numerically explore novel phenomena which arise from quantum interactions.

Tensor networks have been employed for the variational construction of ground states of one- and two-dimensional systems, but to date, no variational algorithm has been proposed for the construction of thermal states. We first propose an alternative approximation to thermal states based on the maximization of the Rényi entropies. Such ensembles can be variationally optimized with tensor network methods, combined with ideas from Riemannian manifold optimization.

We then turn our attention to non-equilibrium physics, in particular in the case of discretized evolutions. We explore alternative ways of performing numerical time-evolution in such settings using the recently-introduced Feynman–Vernon influence-matrix approach, which is known in the tensor-network community as the folding algorithm. Contrary to traditional approaches, the efficiency of this method is insensitive to the growth of the spatial entanglement entropy, and is instead related to the so-called temporal entanglement. In this thesis, we propose a conjecture on the generic logarithmic growth of the temporal entanglement in integrable systems. Based on an appealing semiclassical picture, we argue that the latter must grow sub-linearly, and provide compelling evidence of a very stark difference between the non-interacting and the interacting regime. We support these claims by tensor-network numerical calculations, as well as an analytical solution at a special point in the system parameters.

Finally, we apply tensor network methods to explore topological phases of matter. These phases of matter are intrinsically a quantum effect, as they have a form of long-range order hidden in their entanglement pattern. A plethora of distinct topological phases exists in theory. However, it is far from obvious how to embed these phases in available quantum simulators. The spin liquid state probed in one of these experiments can be understood as the quantum superposition of dimer coverings of a lattice. In this thesis, we extend this paradigm to models of trimers, which are bonds connecting three sites of a lattice. We identify the lattice geometries that yield a robust quantum spin

liquid of trimers with a novel form of topological order, and propose an experimental realization in present-day quantum simulators based on Rydberg atoms.

Zusammenfassung

Die Quantenmechanik zeigt uns, wie man Systeme in Form von Gleichungen beschreibt, aber nicht, wie man sie löst. Für typische Vielteilchen-Quantensysteme wird das Lösen dieser Gleichungen zu einer schwierigen Aufgabe. Die Anzahl der Freiheitsgrade steigt exponentiell mit der Anzahl der Bestandteile, was die Untersuchung stark korrelierter Phänomene—wie etwa Hochtemperatur-Supraleitung oder der fraktionierte Quanten-Hall-Effekt—extrem erschwert.

In den letzten Jahrzehnten haben sich *Tensornetzwerke* als eine neue Klasse von Methoden zur Untersuchung stark korrelierter Systeme in niedrigdimensionalen Gittern entwickelt. Tensornetzwerke haben zu leistungsfähigen numerischen Algorithmen geführt, bieten aber auch eine Sprache, um solche Systeme analytisch zu verstehen. In dieser Dissertation nutzen wir den Rahmen von Tensornetzwerken, um neue algorithmische Ideen vorzuschlagen, und wir wenden sie an, um neuartige Phänomene, die sich aus Quantenwechselwirkungen ergeben, numerisch zu untersuchen.

Tensornetzwerke wurden bereits für die variationeller Ansatz von Grundzuständen ein- und zweidimensionaler Systeme verwendet, aber bisher wurde noch kein variationelle Method für die Konstruktion von thermischen Zuständen entwickelt. Wir entwickeln zunächst eine alternative Annäherung an thermische Zustände vor, die auf der Maximierung der Rényi-Entropien basiert. Solche Ensembles können mit Tensornetzwerk-Methoden, kombiniert mit Ideen aus der Optimierung von Riemannschen Mannigfaltigkeiten, variationell optimiert werden.

Anschließend wenden wir uns der Nicht-Gleichgewichtsphysik zu, insbesondere im Fall von diskretisierten Entwicklungen. Wir erforschen alternative Wege zur Durchführung numerischer Zeitentwicklung in solchen Umgebungen unter Verwendung des kürzlich eingeführten Feynman-Vernon-Einflussmatrix-Ansatzes. Dieser Ansatz ist in der Tensornetzwerk-Gemeinschaft als “Folding”-Algorithmus bekannt. Im Gegensatz zu traditionellen Ansätzen ist die Effizienz dieser Methode unabhängig von der Erhöhung der räumlichen Verschränkungsentropie und hängt stattdessen von der sogenannten zeitlichen Verschränkung ab. In dieser Arbeit stellen wir eine Vermutung über das generische logarithmische Wachstum der zeitlichen Verschränkung in integrablen Systemen auf. Auf der Grundlage eines intuitiven semiklassischen Bildes argumentieren wir, dass letztere unterlinear wachsen muss, und liefern überzeugende Belege für einen deutlichen Unterschied zwischen dem nicht-interagierenden und dem interagierenden Zustand. Wir unterstützen diese Behauptungen durch numerische Berechnungen mit Tensornetzwerken sowie durch eine analytische Lösung für einen speziellen Punkt der Systemparameter.

Schließlich wenden wir Tensornetzwerk-Methoden an, um topologische Phasen zu untersuchen. Diese Phasen der Materie sind an sich ein Quanteneffekt, da sie eine Form von langreichweitiger Ordnung aufweisen, die in ihrer Verschränkungsstruktur verborgen ist. Theoretisch gibt es eine Vielzahl von unterschiedlichen topologischen Phasen. Es ist

jedoch alles andere als offensichtlich, wie diese Phasen in die verfügbaren Quantensimulatoren eingebettet werden können. Der Spinflüssigezustand, der in einem dieser Experimente untersucht wurde, kann als Quantensuperposition von Dimerabdeckungen eines Gitters verstanden werden. In dieser Dissertation erweitern wir dieses Paradigma auf Modelle von Trimeren, das sind Bindungen, die drei Stellen eines Gitters verbinden. Wir identifizieren die Gittergeometrien, die eine stabile Quantenspinflüssigkeit von Trimeren mit einer neuartigen Form der topologischen Ordnung ergeben, und schlagen eine experimentelle Umsetzung in heutigen Quantensimulatoren auf der Basis von Rydberg-Atomen vor.

List of publications

Articles included in this thesis

- G. Giudice et al., *Rényi free energy and variational approximations to thermal states*, Physical Review B **103**, 205128 (2021)
- G. Giudice et al., *Temporal Entanglement, Quasiparticles, and the Role of Interactions*, Physical Review Letters **128**, 220401 (2022)
- G. Giudice et al., *Trimer states with Z_3 topological order in Rydberg atom arrays*, 2022, arXiv:2205.10387

Other articles not included in this thesis

- E. Mascarenhas et al., *A Nonequilibrium quantum phase transition in strongly coupled spin chains*, Quantum **1**, 40 (2017)
- G. Giudici et al., *Diagnosing Potts criticality and two-stage melting in one-dimensional hard-boson models*, Physical Review B **99**, 094434 (2019)
- N. Pancotti et al., *Quantum East Model: Localization, Nonthermal Eigenstates, and Slow Dynamics*, Physical Review X **10**, 021051 (2020)

Contents

CHAPTER 1

INTRODUCTION

1.1 Motivation

The theory of quantum mechanics has been around for almost a century. Already in 1929, Dirac deemed the foundations of quantum mechanics to be mostly laid out, but that two main problems remain, namely (i) incorporating relativistic effects and (ii) understanding many-body effects. Indeed, in Ref. [7], to motivate the study of many-electron systems, he writes:

> *The underlying physical laws necessary for the mathematical theory of a large part of physics and the whole of chemistry are thus completely known, and the difficulty is only that the exact application of these laws leads to equations much too complicated to be soluble. It therefore becomes desirable that approximate practical methods of applying quantum mechanics should be developed, which can lead to an explanation of the main features of complex atomic systems without too much computation.*

Dirac's comments are incredibly prescient. The first point was one of the ingredients that contributed to the development of relativistic quantum field theories, which eventually led to the formulation of the Standard Model. The latter is the motivation behind condensed-matter physics. Indeed, one hundred years later, we are still searching for new methods to tackle many-body problems in quantum physics.

The main difficulty in describing a many-body quantum systems comes from our representation of states using the tensor product—this leads to an exponential growth of the degrees of freedom with the number of constituents. Just storing a representation of a quantum state on a computer is a problematic task. For example, the state of 26 qubits—a qubit being the smallest non-trivial local degree of freedom—would require around a gigabyte of memory[1]. Take ten times that number of qubits, and the number of bits required would be approximately the number of baryons in the universe.

[1] Assuming double-precision complex numbers, i.e. 128-bits.

Keeping track of all these degrees of freedom is clearly a hopeless task. But do we really *need* to? In physics we are often interested in some approximate, or *compressed* representation, from which we can extract relevant thermodynamic quantities, like energy and magnetization. Historically, the problem has been tackled using perturbative quantum field theory [8]. The corresponding noninteracting model is solved exactly, and perturbations around this solution are taken into account according to their order in the interaction parameter. This approach however fails when the interaction is strong, and the interactions drive the system to a different phase of matter. In one-dimensional lattice systems, certain interacting systems known as *integrable* can be solved using *Bethe ansatz* techniques [9]. These techniques are extremely powerful and have immensely contributed to our understanding of low-dimensional systems [2]. Despite these successes, integrable systems are very special, as they have an *extensive number of conservation laws*.

From a computational point of view, Monte Carlo methods have provided an alternative point of view of the problem [14]. Since the wavefunction is impossible to represent exactly, we may as well give up completely on writing it down—after all, it is not something we can directly observe. Instead, we sample from the thermal distribution to estimate local thermodynamic quantities. In certain cases, this sampling can be done in an efficient manner, and its properties are well understood with the theory of Markov chains. Much effort has been dedicated to speeding up the sampling procedure, and has proven to be a scalable solution in many situations, especially in higher dimensions. However, the sampling for certain quantum systems cannot be performed in an efficient way because of the so-called sign problem, where the integrals to be evaluated contain near-cancellations. Unfortunately, the sign problem shows up in many systems of interest. This seems to be a more fundamental problem with the method, as it is believed to be intimately related to the systems itself [15].

A direction which can be seen as complementary to the Monte Carlo approach is to insist on having an explicit model for the state of the system. Generally speaking, this is more useful in undestanding the nature of our solution and to gain a deeper physical insight beyond the ability of computing observables. Typically this model, or *ansatz* (as we like to refer to it in physics), has some free parameters that we can tune. We can then play with these parameters, or *optimize* them, in such a way that it best approximates that which we are interested in representing. For example, if we are interested in representing the ground state, we may minimize the energy with respect to our parameters. This, in a nutshell, is the *variational principle*.

Tensor networks [16–18] are a variational class of quantum states that are extremely flexible and typically allow for a systematic enrichment by increasing the number of parameters, something very appealing for tackling challenging systems, for example where perturbative approaches fail and the sign problem occurs. Tensor networks have been a topic of intense research in the last 20 years. The core ideas, somewhat remarkably, have been around for at least 50 years in different forms in quantum physics. Indeed, the ideas of matrix product states were almost completely laid out in 1968 by Baxter. When solving a diluted dimer model on the square lattice, he introduced the concept of the transfer matrix and noted [19]

[2] From a tensor network perspective, the geometric Bethe ansatz can be thought of as a class of solutions to the *Yang–Baxter* equations, which derive from imposing the associativity condition to certain tensors, see for example Refs. [10–12]. The tensor network picture also offers a potential avenue to generalize these concepts, see for example Ref. [13] and references therein.

> *In fact, if they are allowed to have infinitely great dimensionality, then the results obtained should be formally exact. Further, and more significantly, if the matrices are restricted to be of finite and quite small dimensionality, then it should still be possible to obtain good approximations to* Γ [the leading eigenvalue] *and the thermodynamic properties.*

Readers acquainted with matrix product states will probably find this remarkably familiar. Interest in tensor networks did not spark until the early 1990s, with the advent of the DMRG algorithm of White [20, 21] as a numerical method for simulating one-dimensional systems. Its connection with "finite correlated states" [22, 23] (generalizations of the AKLT state) was soon recognized and reformulated as a variational method based on MPS [24]. Refs. [17, 18] recount in more detail the key historical steps. From the beginning of the 21st century, research into tensor networks took off, in part due to the interest from the quantum information community. The intimate connection between tensor networks and *entanglement* provided additional interest in these methods, not only as a numerical tool, but as a powerful analytical *framework* to study quantum systems. Certainly the concept of entanglement was not new. Indeed, already in 1935, Schrödinger recognized that entanglement was "*the* characteristic trait of quantum mechanics, the one that enforces its entire departure from classical lines of thought" [25]. Yet, it is only in the last decades that it was promoted to a *defining* feature of different phases of matter in many-body quantum physics.

Finally, the concepts of tensor networks are certainly not unique to physics. Similar concepts have been reinvented in applied mathematics and computer science [26, 27] to tackle high dimensional problems such as stochastic partial differential equations and financial modelling. In other areas of physics they have been used to solve non-equilibrium statistical physics problems [28], and the classification of Lie groups [29]. Recently, the connection with machine learning techniques is being explored as well [30–32].

1.2 Lattice physics

In condensed matter physics, we typically try to understand how macroscopic phenomena arise from microscopic interactions. Challenging problems where strong correlations dominate are, for example, high-T_c [33, 34] superconductivity and the fractional quantum Hall effect [35]. Solving a model from first principles is generally a hard task, so in practice, an effective model is chosen. For example, the Hubbard model is believed to represent high-T_c superconductivity, while the Heisenberg model was proposed to explain quantum magnetism. These effective models try to capture the salient features of the system in question, in particular the low-energy properties.

In this thesis, we focus on the case where the degrees of freedom are spatially restricted to the sites of a *lattice*. This is a valid approximation for many systems of interests, as most solids have a crystalline order, and at low-energies, electrons typically are confined to orbit around their respective atoms. We may also consider the interactions of atoms directly. This is particularly relevant for recent experimental platforms based on Rydberg atoms, where neutral atoms are individually trapped and arranged in a desired lattice configuration [36, 37]. The excited states of these atoms can exhibit strong dipolar interactions, and can be targeted using using external laser fields. We associate a local system to each lattice site i described by a d-dimensional system; the corresponding local

Hilbert space is $\mathbb{H}_i = \mathbb{C}^d$. The total *Hilbert space* is constructed using the tensor product $\otimes$, i.e. $\mathbb{H} = \bigotimes_{i=1}^{N} \mathbb{H}_i$, equipped with the usual inner product $\langle \cdot | \cdot \rangle$. The generalization to generic graphs and different vector spaces is straightforward. The interactions are then described by a *Hamiltonian* which couples the degrees of freedom, typically in some local way. We consider *local* Hamiltonians of the form

$$H = \sum_{i=1}^{N} h_i \,, \tag{1.1}$$

where h_i acts on a lattice patch around site i. The simplest non-trivial situation is a two-site operator acting on nearest-neighbor pairs:

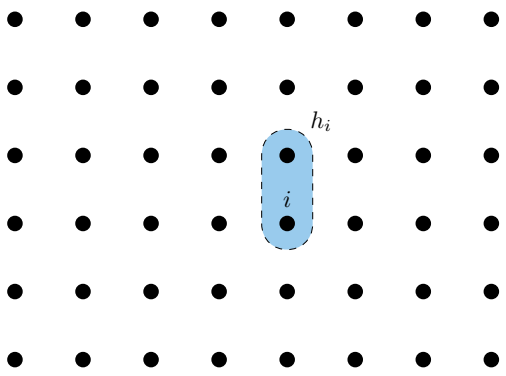

For example, the Heisenberg model is described by

$$H = J \sum_{\langle i,j \rangle} \mathbf{S}_i \cdot \mathbf{S}_j \,,$$

where $\mathbf{S}_i$ is the spin operator at site i, J is the coupling strength, and the sum runs over all nearest-neighbor pairs. Hence, each site is occupied by a spin degree of freedom, and the coupling between their dipolar moments is described by the interaction term: spins that are aligned (antialigned) are energetically favored for $J < 0$ ($J > 0$). The Heisenberg model can as well be derived from the Hubbard model at half filling in the limit of strong repulsive interaction.

The Hamiltonian is the core description of a system in condensed matter. Not only does it govern the dynamics (via the Schrödinger equation), but it also determines the equilibrium properties. For a fixed inverse temperature β, the Gibbs state at thermal equilibrium is $\rho \propto e^{-\beta H}$. This can be derived from a *maximum entropy principle*. Due to fluctuations, it is not possible to precisely give a description of a system as a particular (pure) state, but we resort to a statistical description. Hence, we define a density operator ρ as a self-adjoint ($\rho = \rho^\dagger$), positive ($\rho \succeq 0$), normalized ($\operatorname{Tr} \rho = 1$) operator, such that it returns expectation values averaged over the possible outcomes—the classical analogue is a probability distribution. We assign the density operator in the following way: we choose the positive-definite operator that maximizes the entropy, i.e. contains the least amount of information about the system. Since the only information we have is that the system is in thermal equilibrium, the energy must be constant. By including this constraint,

$$\rho_G = \arg\min_{\substack{\rho \succeq 0 \\ \operatorname{Tr}(H\rho) = \bar{E} \\ \operatorname{Tr} \rho = 1}} S(\rho) \,,$$

where $S(\rho)$ is the von Neumann entropy $S(\rho) = -\operatorname{Tr}(\rho \log \rho)$. Performing the extremization with Lagrange multipliers yields the Gibbs state

$$\rho_G = \frac{1}{Z} e^{-\beta H},$$

where $Z = \operatorname{Tr}(e^{-\beta H})$ is the partition function, and β, coming from the Lagrange multiplier, is interpreted as the inverse temperature. Note that as we send $\beta \to \infty$, we obtain the lowest energy state $|E_0\rangle$, known as the *ground state*. In fact, by expanding in the energy eigenbasis $\{E_k\}$,

$$\lim_{\beta\to\infty} \frac{1}{Z} e^{-\beta H} = \lim_{\beta\to\infty} \frac{\sum_k e^{-\beta E_k} |E_k\rangle \langle E_k|}{\sum_k e^{-\beta E_k}} = |E_0\rangle \langle E_0| ,$$

assuming for simplicity that the system does not have degenerate ground states.

Quantum effects are typically most prominent in the low-temperature regime, so we are usually interested in the low-energy subspace of the Hamiltonian, which corresponds to the eigenstates of the Hamiltonian with smallest eigenvalues. As we just saw, the ground state is particularly important as it determines all the properties of the system at zero temperature. The low-lying next eigenstates determine the properties related to excitations. If the ground state is separated from the next eigenstates by an energy gap which does not close in the thermodynamic limit, we say that the system is *gapped*. This gap has far-reaching consequences for the properties of the system. For example, if the Hamiltonian describes electrons moving in a material, the gap reveals whether the system is a conductor or an insulator: in a gapless system, arbitrarily small electric fields can produce excitations, and the system is said to be a conductor. In general, in gapped systems all correlations decay exponentially with the distance [38]. This stands in contrast to critical models, where the ground-state correlations can decay with a power law. Such properties are a manifestation of the fact that many of the low-energy properties of the system are encoded in the ground state.

The search for the ground state, central in many-body quantum physics, is not an objective *per se*, but rather as a means to compute the static properties of a system. One is typically most interested in *local* observables $\langle O_i \rangle = \langle \Psi | O_i | \Psi \rangle$ (or $\operatorname{Tr}(O_i \rho)$ in the case of density matrices), where O_i has non-trivial support on a patch around site i.

1.3 Outline

Tensor networks for quantum physics As tensor networks will be the recurring theme in this thesis, we introduce the basic concepts in Chapter 2. We present the graphical notation used throughout this thesis, and discuss the fundamental operations with tensors. We then introduce the main tensor network states used in physics, with a particular emphasis on matrix product states and projected entangled pair states. The geometric properties of the variational manifold of matrix product states are introduced as well, and will be used later on in Chapter 3. The chapters following present some applications of tensor networks to study many-body quantum systems.

Rényi free energy In Chapter 3, we propose the construction of thermodynamic ensembles that minimize the Rényi free energy, as an alternative to Gibbs states. For large systems, the local properties of these Rényi ensembles coincide with those of thermal

equilibrium, and they can be used as approximations to thermal states. We provide algorithms to find tensor network approximations to the 2-Rényi ensemble. In particular, a matrix-product-state representation can be found by using gradient-based optimization on Riemannian manifolds, or via a non-linear evolution which yields the desired state as a fixed point. We analyze the performance of the algorithms and the properties of the ensembles on one-dimensional spin chains.

Temporal entanglement In quantum many-body dynamics admitting a description in terms of *noninteracting* quasiparticles, the Feynman-Vernon influence matrix (IM), encoding the effect of the system on the evolution of its local subsystems, can be analyzed exactly. For discrete dynamics, the temporal entanglement of the corresponding IM satisfies an area law, suggesting the possibility of an efficient representation of the IM in terms of matrix-product states. A natural question is whether integrable interactions, preserving stable quasiparticles, affect the behavior of the temporal entanglement. While a simple semiclassical picture suggests a sublinear growth in time, one can wonder whether interactions may lead to violations of the area law. We address this problem in Chapter 4, by analyzing quantum quenches in a family of discrete integrable dynamics corresponding to the real-time Trotterization of the *interacting* XXZ Heisenberg model. By means of an analytical solution at the dual-unitary point and numerical calculations for generic values of the system parameters, we provide evidence that, away from the noninteracting limit, the temporal entanglement displays a *logarithmic* growth in time, thus violating the area law. Our findings highlight the non-trivial role of interactions, and raise interesting questions on the possibility to efficiently simulate the local dynamics of interacting integrable systems.

Trimer resonating-valence-bond states In Chapter 5, we study the quantum states obtained as equal-weight superpositions of all trimer coverings of a lattice, with the constraint of having a trimer on each vertex: the so-called trimer resonating-valence-bond (tRVB) states. Exploiting their tensor network representation, we show that these states can host $\mathbb{Z}_3$ topological order or can be gapless liquids with $\mathrm{U}(1) \times \mathrm{U}(1)$ local symmetry. We prove that this continuous symmetry emerges whenever the lattice is tripartite such that each trimer covers all the three sublattices. In the gapped case, we demonstrate the stability of topological order against dilution of maximal trimer coverings, which is relevant for realistic models where the density of trimers can fluctuate. Furthermore, we clarify the connection between gapped tRVB states and $\mathbb{Z}_3$ lattice gauge theories by smoothly connecting the former to the $\mathbb{Z}_3$ toric code, and discuss the non-local excitations on top of tRVB states. Finally, we analyze via exact diagonalization the zero-temperature phase diagram of a diluted trimer model on the square lattice and demonstrate that the ground state exhibits topological properties in a narrow region in parameter space. We show that a similar model can be implemented in Rydberg atom arrays exploiting the blockade effect. We investigate dynamical preparation schemes in this setup and provide a viable route for probing experimentally $\mathbb{Z}_3$ quantum spin liquids.

Conclusions and outlook We conclude in Chapter 6, and present an outlook for further research directions.

A method is more important than a discovery, since the right method will lead to new and even more important discoveries.

L. D. Landau [40]

CHAPTER 2

TENSOR NETWORKS FOR QUANTUM PHYSICS

2.1 Basics

The main purpose of tensor networks is to represent mathematical expressions involving many indices and summations in a clear and concise way. Using a graphical representation, the structure and relationship between the different parts becomes evident. As we will see later on, it is not only a handy way of writing down complicated expressions, but tensor networks become the building blocks to construct more complicated objects, such as quantum states. As we will see later on, this will come in handy to predict certain properties of the whole states, from the properties of the individual objects. In this section, we introduce the basics: tensors, the graphical rules of tensor networks, and some basic operations.

What is a tensor?

Tensors are ubiquitous in physics, mathematics and computer science, and naturally many different definitions are used. From a pratical point of view, tensors can be thought of as simply multidimensional arrays[1]. We can represent them graphically as some shape, with lines (or *legs*) coming out of it, each one corresponding to an index [16, 39]. For example, we can represent a scalar, a vector, and a matrix as

The number of indices is referred to as the *rank* of a tensor. By connecting the legs of different tensors, we can represent a summation (or *contraction*) over that index. For example in the matrix multiplication $\sum_{j,k} A_{ij} B_{jk} C_{kl}$ the contracted indices are j and k. The resulting tensor is a rank-2 tensor formed by the uncontracted indices i and l. We represent this graphically by connecting the indices of the tensors that are involved in the summation. Here are some examples of (i) a scalar product, (ii) a matrix-vector multiplication, (iii) a matrix-matrix multiplication and (iv) a more complicated

[1] Lately, in machine learning this has become the *de facto* definition.

contraction yielding a vector

(i) $\sum_i A_i B_i =$ 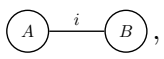

, (iii) $\sum_j A_{i,j} B_{j,k} =$ 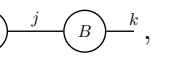

,

(ii) $\sum_j A_{i,j} B_j =$ 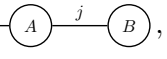

, (iv) $\sum_{i,j,k,l,n} A_{i,j} B_{i,j,k,l} C_{k,m} D_{l,n,n} =$ 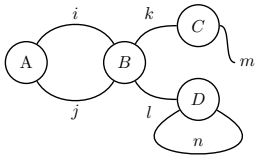

.

We see that contractions between a set of tensors can be represented as a sort of graph, that is called a *tensor network* (TN).

This definition is however limited to Euclidean spaces such as $\mathbb{R}^d$ or $\mathbb{C}^d$. To work in more general vector spaces, it is sometimes handy to generalize the definition of a tensor to be an element from the tensor product of several *vector spaces* over the same field. For example, we can write a rank-r tensor T

$$T \in V_1 \otimes V_2 \otimes \cdots \otimes V_r \,.$$

We start by representing vectors by adding an outgoing arrow on their leg

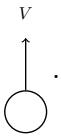

.

In order to take scalar products, we must also define dual vectors belonging to the *dual* space V^* ((or linear functionals on V). We represent these with an arrow in the opposite direction

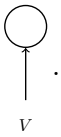

.

This notation makes it clear that we can identify a dual vector with a primal vector on the dual space, since flipping the direction of an arrow then corresponds to taking the dual space

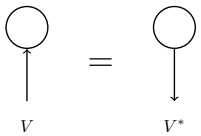

. (2.1)

Equivalently, we can identify a vector as a dual vector in the dual space (since $V^{**} = V$). The tensor product of two tensors can be seen as just placing two tensors next to each other, or viewing it trivially as a single tensor

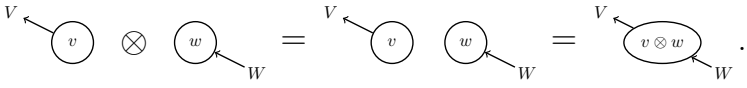

. (2.2)

This can be used to construct tensors of arbitrary rank.

Notice that in this last example the direction of the arrows suggest that we think of the tensor $v \otimes w$ as a linear functional in W which then outputs a vector in V. In other words, we can think of it as a map $W \to V$. This brings us to a second way one can think

of a tensor: as a *multilinear map* between vector spaces. We can then interpret a tensor as a mapping from a set of the spaces (the *domain*) to the set of remaining spaces (the *codomain*)

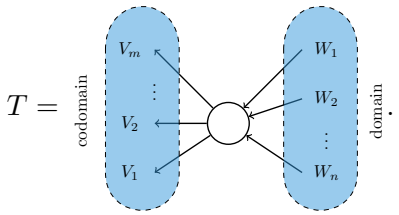

The choice of partitioning is arbitrary, and we can always freely move indices from one partition to the other, remembering to take the dual space when changing sides. Finally, we choose to represent the *adjoint* tensor with a shaded color

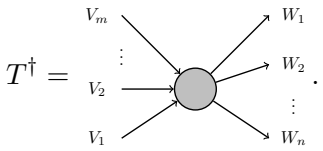

Tensor contractions are represented in the same way, as long as we can connect legs representing the same vector space, such as

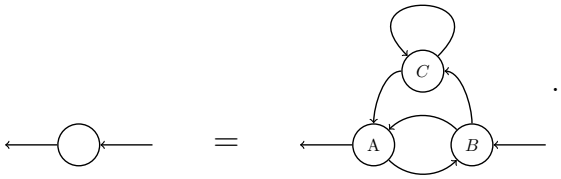

This diagrammatic approach is actually a very powerful tool. Much like Feynman diagrams for quantum field theory, tensor networks allow us to get a more intuitive and visual understanding rather than handling long equations. To illustrate this briefly, the cyclic property of the trace is immediately visible from its diagrammatic form

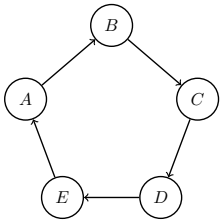

$$= \mathrm{Tr}(ABCDE) = \mathrm{Tr}(BCDEA) = \mathrm{Tr}(CDEAB) = \dots , \tag{2.3}$$

because of its symmetry the result does not change by starting to contract from another element, as long as the correct network structure is preserved [39].

We also wish to point out is that, contrary to the index notation, a tensor network does not assume any specific basis dependence on any of its contractions. Indeed we can always introduce on a link the resolution of the identity $\mathbb{1} = X^{-1}X$, where X is some invertible operator. It corresponds to performing a basis transformation on the specific leg. This leads us to an extra convention: that the identity operator $\mathbb{1}$ is represented as a simple line

. (2.4)

The introduction of arrows is useful in more complicated vector spaces to keep track of the fusion of the irreducible representations of certain symmetries. In quantum physics we often want to include some unitary symmetry group $\mathcal{G}$ which acts on the vector spaces with a certain representation. A vector space V can then be represented as the direct sum of the irreducible representations of $\mathcal{G}$, and a tensor can be restricted to the equivariant under the action of the symmetry. Because of Schur's Lemma [41], such a tensor is in block-diagonal form. If one keeps track of how the irreducible representations fuse and split, one can exploit the block-diagonal form for significant computational speedups [42]. Indeed, many Hamiltonians of interest commute with the unitary representations of some symmetry group $\mathcal{G}$: $[H, U_g] = 0$, $g \in \mathcal{G}$. If we are interested in the ground state, we can then restrict ourselves to states obeying $U_g |\Psi\rangle = |\Psi\rangle$, assuming no spontaneous symmetry breaking occurs. In the case of *local* symmetries $U_g = u_g^{\otimes N}$, where the u_g act on a single site, the symmetry constraint becomes a constraint on the local tensors. It was realized early on that the common tensor-network algorithms could be adapted to handle symmetric tensors [43–46], both for Abelian symmetries [47, 48] as well as non-Abelian ones [49, 50].

Index manipulation

Because we can freely combine vector spaces with the tensor product, we are allowed to group indices at will. For example, we can easily see that any contraction of two arbitrary tensors can be seen as a matrix multiplication after grouping the indices[2]

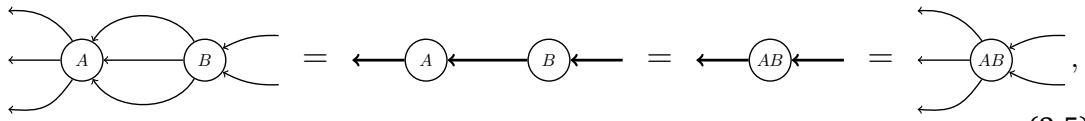

(2.5)

where the we have indicated in bold the grouped indices. This is actually how most numerical tensor contraction packages perform a contraction on a computer. Instead of doing the summation over some indices one at a time, the indices of the tensors are reshuffled such that they form two matrices. Then the matrix multiplication is performed, and the remaining indices are split up again to obtain the original ones. This strategy is employed in most numerical libraries, as typically matrix multiplication routines on modern CPU architectures are highly optimized [51]. This is also handy to place an upper bound on the time complexity of doing a contraction between the tensors by $O(\#\text{ of legs})$. [3]

For a tensor network with more than two tensors, the order of contraction becomes very important. Typically one can only contract tensors in a pairwise fashion, so the order in which we choose to perform the contraction (which we can think of as a *bracketing* of the expression) is crucial: the complexity—both in space and time—can vary wildly. Explicit examples are provided in Ref. [16]. Unfortunately there exist networks that do

[2] After performing potential traces on individual tensors.

[3] It is an upper bound since algorithms with slightly better asymptotic scalings are known, such as Strassen's algorithm [52].

not admit any efficient contraction. For example in a grid

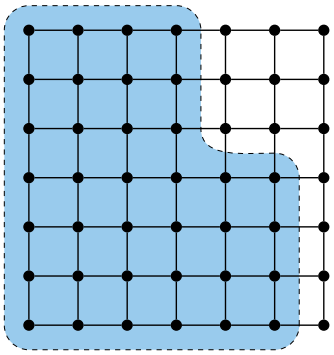

we soon realize that the contraction necessarily must store an object which has at least a number of legs equal to one of the sides, as is depicted in the shaded area. Additionally, it is possible to encode in a tensor network very difficult tasks, such as computing the number of solutions to NP-complete problems [16, 53] (known as a #P–complete problem), something that is very unlikely to be computable efficiently.

In general, even computing the optimal contraction order of an arbitrary tensor network is a hard (at least #P–complete) problem [54]. Heuristic methods exist that are able to find an approximately optimal contraction tree for several hundreds or even thousands of tensors [55, 56]. As a rule of thumb, tensor networks made of a tree-like structure are efficiently contractible, while the presence of closed cycles, or *loops*, makes the contraction much more costly.

Factorizations

We have learned that we combine tensors together by contracting them. Can we do the opposite operation? It turns out that the opposite operation can be done too, by generalizing the concept of *matrix factorizations*.

One of the common ways of factorizing a tensor is to use the *singular value decomposition* (SVD), appropriately generalized to higher ranks. An SVD splits a tensor into two isometries U and V and a diagonal tensor S. Similarly to before, we partition the legs into two sets, interpret the tensor as a matrix and perform the factorization

$$T^{i_1,\dots,i_m}_{j_1,\dots,j_n} = \sum_k U^{i_1,\dots,i_m}_k \, S^k_k \, V^k_{j_1,\dots,j_n} = \tag{2.6}$$

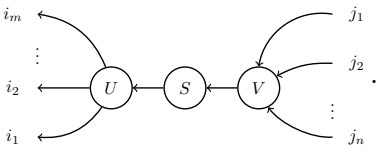

The tensor S contains the *singular values*, which are positive real numbers.

Other matrix factorizations can be similarly employed. The popularity of the SVD lies in the fact that the decomposition is *rank-revealing* (in the matrix sense). The new index created has the smallest possible dimension, which is what is most computationally advantageous.

Not only does the SVD give the factorization with the smallest possible index dimension, but it also allows one to *approximately* factorize a tensor in a controlled way. Essentially the SVD decomposition gives a way of finding the closest possible factorization (in Frobenius norm) to the original tensor with a smaller intermediate dimension. Not only that, but the approximation is controlled: all we have to do is discard the smallest

singular values. This method is known as the *Eckart–Young* theorem [57, 58], although it was previously discovered by Schmidt [59, 60].

Applications of this approximation have been applied early on for image compression [61]. By storing a factorization of an original image we are able to encode an image while retaining only a small fraction of the original data [cf. Fig. 2.1].

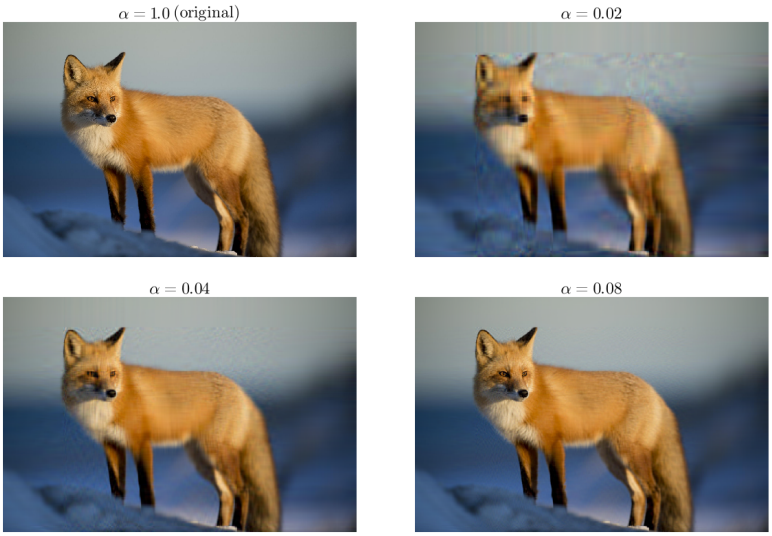

Figure 2.1: Example of SVD compression of an image. The original image (seen as a rank-3 tensor) is factorized, the first n singular values are retained and the image is reconstructed. Here, n is chosen to be 8, 16, 64. The compression ratio α is defined as the ratio between the total dimension of the compressed tensors and the dimension of the original image [62].

2.2 Tensor networks as quantum states

Tensor networks can be employed for the representation of quantum states. In this thesis we consider the case of states on a regular lattice with N sites, where each site is associated to a d-level quantum system. The associated finite-dimensional *Hilbert space* is simply the complex Euclidean space $\mathbb{H} = \bigotimes_{k=1}^{N} \mathbb{C}^d$, equipped with the usual inner product $\langle\cdot|\cdot\rangle$. Generalizations to generic graphs, different vector spaces and different dimensions at each site should be straightforward.

Hence an arbitrary pure quantum state $|\Psi\rangle \in \mathbb{H}$ can be written down in the computation basis $\vec{s} = s_1, \ldots, s_N$ as

$$|\Psi\rangle = \sum_{s_1,\ldots,s_N} \psi_{s_1,\ldots,s_N} |s_1, \ldots, s_N\rangle = \tag{2.7}$$

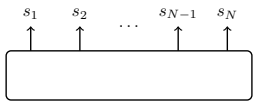

The amplitudes $\psi_{s_1,\ldots,s_N} = \langle s_1, \ldots, s_N|\Psi\rangle$ correspond to a complex number for each combination of $s_1, \ldots, s_N$. Hence, once we have chosen a basis, we can fully describe a state with the complex tensor $\psi_{s_1,\ldots,s_N}$, which we represent as a big blob with N legs. Each leg corresponds to an index s_k, which we shall often refer to the *physical indices*, as we are about to introduce many more.

The essential idea behind a *tensor network state* is to parametrize a quantum state as a contraction of low-rank tensors. For example, we can construct a one-dimensional chain

$|\Psi\rangle =$ 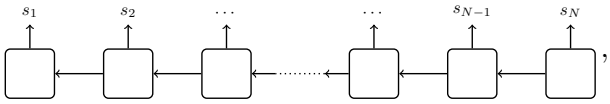

, (2.8)

which we refer to as a *matrix product state*. The newly introduced indices that are contracted are referred to as *virtual* indices. [4] Similarly, we can generalize this construction to higher dimensions,

$|\Psi\rangle =$ 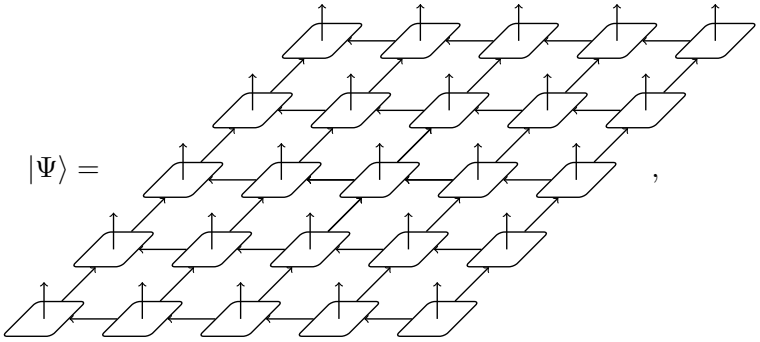 , (2.9)

which is called a *projected-entangled pair state* (PEPS).

So far, the tensor networks we considered follow very closely the geometry of the lattice. Of course, we are not constrained by this, and we are allowed to construct more complicated networks. Several constructions introduce an additional "dimension", which can be thought broadly-speaking as a renormalization dimension. For instance, *tree tensor networks* (TTN) correspond to tensor networks on tree graphs [63]. They are efficiently contractible, and, as opposed to MPS, allow for algebraically-decaying correlations [64]. It is however challenging to construct two-dimensional TTNs that can account for an area law of entanglement, which we clarify later on. Another construction introduced for representing critical states in one dimension is the *multiscale entanglement renormalization ansatz* (MERA) [65]. It is more sophisticated network of isometries[5] for which local expectation values are efficiently computable, even if it contains loops. Their higher dimensional generalization was however shown to be embeddable in PEPS [66]. In this thesis, we leave these more exotic alternatives to the side and restrict ourselves to MPS and PEPS.

[4] This is not the most general MPS. We could introduce an extra index linking the first tensor to the last tensor, such that the state becomes

$$|\Psi\rangle = \sum_{s_1,\ldots,s_N} \mathrm{Tr}\left(A_1^{s_1} A_2^{s_2} \ldots A_{N-1}^{s_{N-1}} A_N^{s_N}\right) |s_1, \ldots, s_N\rangle$$

where the trace is over the virtual degrees of freedom. However, this is typically less efficient in numerical routines. For the infinite uniform case we prefer this notation, as the choice of boundary condition should not matter, except in the case of symmetry-protected topological order (not discussed in this thesis).

[5] An isometry is a linear map such that $U^\dagger U = \mathbb{1}$ ($UU^\dagger = \mathbb{1}$), when the dimension of the codomain is larger (smaller) that the dimension of the domain. Isometricity can be seen as the generalization of unitarity to non-square matrices.

Tensor networks and area laws

At this point it is still not clear what we have gained. While any state could potentially be represented as a TN state (and constructive algorithms exist for MPS [67]), it is not necessarily an *efficient* representation. In order to have a polynomial number of parameters in system size, the dimension of each virtual index is typically upper bounded by some constant, which we call the *bond dimension*. Despite this restriction, we can represent many known and commonly used states in quantum physics [16–18]. More importantly, the bond dimension is intimately related to the concept of *entanglement entropy*. When choosing a bipartition of a pure quantum system, the entanglement entropy is defined as

$$S = -\operatorname{Tr}(\rho \log \rho) \tag{2.10}$$

where ρ is the reduced density matrix of either half of the bipartition. Informally, it corresponds to some kind of average over the *quantum correlations* between the two subsystems. It turns out that for TN states, the entanglement entropy of any bipartition is easily upper bounded by the number of virtual legs cut off by the the bipartition [68]. Consider for example the state represented in the following

$|\Psi\rangle =$ 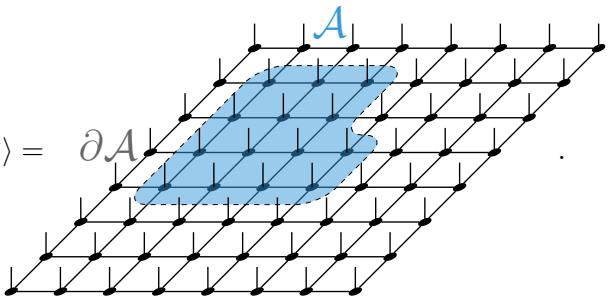

. (2.11)

We choose a subsystem $\mathcal{A}$ and trace out the degrees of freedom in the complement $\bar{\mathcal{A}}$ as

$\rho_{\mathcal{A}} = \operatorname{Tr}_{\bar{\mathcal{A}}} |\Psi\rangle\langle\Psi| =$ 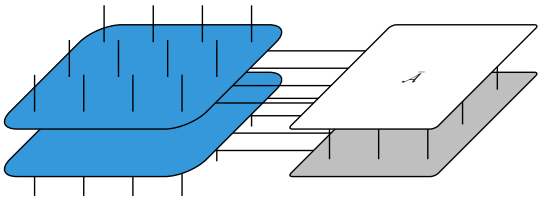

. (2.12)

The blue tensor, representing the physical degrees of freedom belonging to $\mathcal{A}$, is connected to the tensor representing the ones of $\bar{\mathcal{A}}$ with the virtual degrees of freedom in $\partial\mathcal{A}$. The partial trace is then performed over the physical degrees of freedom of $\bar{\mathcal{A}}$. Note that the number of legs in the diagram is chosen arbitrarily. Now, the matrix rank of $\rho_{\mathcal{A}}$ is effectively bounded by the dimension of the space of the boundary of $\mathcal{A}$. Denoting it by $|\partial\mathcal{A}|$, the entanglement entropy is bounded by $S \leq \log |\partial\mathcal{A}|$.

Such states are highly relevant physically. The ground state of local, gapped Hamiltonians are widely believed[6] to obey an *area law*: the entanglement entropy of a subregion scales proportionally to the boundary of the subregion, and not its volume. Indeed, as we will discuss more in detain in Sec. 2.5, efficient heuristic algorithms for finding ground

[6] This is rigorously proven in 1D [69], as well as for 2D frustration-free Hamiltonians in a recent breakthrough paper [70].

states in one dimension have spearheaded the popularity of tensor networks for quantum physics. In particular matrix product states (MPS) are arguably the most effective ansatz to represent ground states of local, gapped Hamiltonians in one dimension [69, 71–73]. For a more detailed discussion of the relationship between TN states and area laws, we refer the interested reader to Ref. [17].

On a more philosophical level, TN states reintroduce the notion of *locality* to quantum states, since each physical site is associated to a tensor. This is desirable, as our intuition suggests that the physics at one site should be mostly determined by its neighborhood. Already Feynman pointed out that in quantum field theory this notion of locality is not particularly apparent [74]:

> *Now, in field theory, what's going on here and what's going on over there and all over space is more or less the same. Why do we have to keep track in our functional of all the things that are going on over there while we are looking at the things that are going on over here?* [...] *It's really quite insane, actually: we are trying to find the energy by taking the expectation of an operator which is located here and we present ourselves with a functional which is dependent on everything all over the map. That's something wrong.*

Feynman's vision was to construct a new variational class which would account for this locality. Despite being critical of the variational principle for quantum field theories, he still has hope that

> *Maybe there is some way to surround the object, or the region where we want to calculate things, by a surface and describe what things are coming in across the surface. It tells us everything that's going on outside.*

In a way, TN provide an answer to this research program: they model the entanglement degrees of freedom that are at the interface of two regions. Since MPS and PEPS typically are chosen to have the same geometry of the underlying system, they naturally represent this interface in a lower dimension, and by construction represent states which obey a corresponding area law.

Finally, tensor networks are a useful constructive class. A bit like stacking Lego bricks together, we can construct complicated states from elementary tensors. From the properties of the individual tensor we can then predict certain properties of the full state, like symmetries and unconventional orders. Simply repeating the same tensor over and over, we can costruct nontrivial translationally-invariant states directly in the thermodynamic limit. As we will see in Sec. 2.4, we can then optimize this class of variational states, for example to approximate the ground state.

2.3 Operators

We can easily generalize the construction of TN states to operators as well. A *matrix product operator* (MPO) [75–77] is graphically represented as

$O =$ 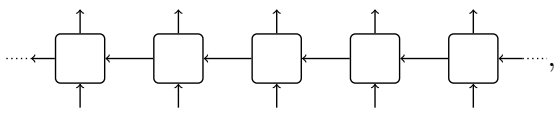 , (2.13)

and a *projected entangled pair operator* (PEPO) reads

$O =$ 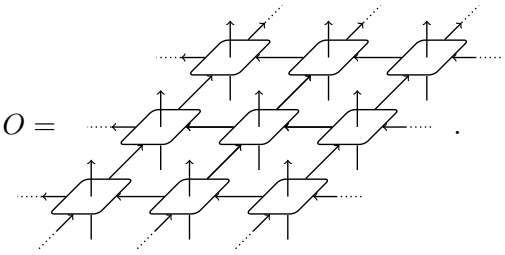 . (2.14)

These constructions are convenient to efficiently represent local Hamiltonians [67, 78][7].

TN operators have also been employed as an ansatz representing mixed states, especially thermal states. In general, thermal states with exponentially decaying correlations obey an area law [79, 80], so one expects that an efficient tensor network representation exists. Indeed theoretical work has bounded the bond dimension necessary for an approximate PEPO representation of a thermal state to $(N/\epsilon)^{O(\beta)}$ [38, 81] and subsequently a better bound $D \sim \exp\left[O\left(\sqrt{\beta \log(N/\epsilon)}\right)\right]$ was found [80]. Despite these theoretical results, on the numerical side, algorithms as effective as DMRG are still lacking. Yet, several numerical algorithms for constructing thermal TN states exist, and are discussed more in detail in Chapter 3.

MPOs also appear as the transfer matrix of two-dimensional statistical-mechanics models. Indeed, the partition function of many models on a 2D square lattice can be formulated as grid of rank-4 tensors,

$Z =$ 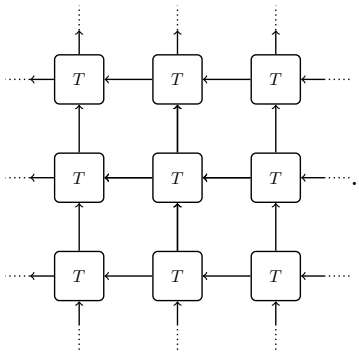 . (2.15)

For example, the partition function of the 2D classical Ising model can be constructed as follows

$$Z = \sum_{\vec{\sigma}} e^{\beta \sum_{\langle i,j \rangle} \sigma_i \sigma_j} =$$ 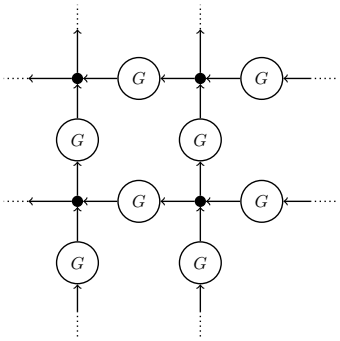 (2.16)

[7] In one dimension these correspond to finite-state automata, in higher dimensions to weighted finite signalling agents, cf. Ref [78].

where

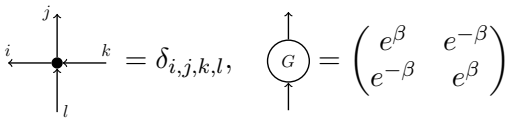

(2.17)

The idea is that the δ-tensors represent each spin degree of freedom, and G encodes the Bolzmann weights, which gives a contribution e^{β} ($e^{-\beta}$) to the partition function if the neighboring spins are aligned (anti-aligned). This can then be recast in the form of Eq. (2.15). Such formulations of the partition function can then be studied by considering taking one row of the partition function, seen as an MPO. This is commonly referred to as the *transfer operator*

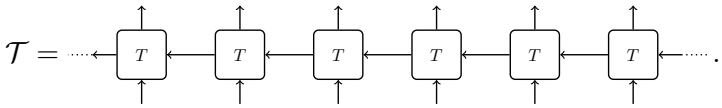

(2.18)

The leading eigenvector of this MPO can then be estimated—for finite sizes or using a uniform MPS approximation—to extract the properties of the model. This method is, in essence, the modern formulation of Baxter's method mentioned in Chapter 1. Of course, for the specific case of the Ising model, the partition function was famously solved exactly by Onsager in 1944 [82], but this formalism can be generalized to tackle many different models. Such techniques are reviewed in detail in Ref. [11], and are used extensively in Chapter 5.

These techniques are useful for contracting PEPS as well. When computing an overlap, or an expectation of a local operator on states that are uniform PEPS, the network becomes very similar to Eq. (2.15), where the local tensor is

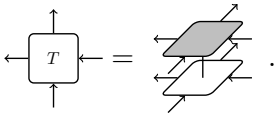

(2.19)

As a side note, we remark that we can construct a PEPS representation of a state $|\Psi\rangle$ such that its norm $\langle\Psi|\Psi\rangle$ corresponds to the partition function of the 2D classical Ising model[83]. This model undergoes a thermal transition for a finite temperature $\beta_c = \ln(1+\sqrt{2})/2$, at which point the model displays an algebraic decay of correlations. Therefore PEPS can describe states with an *algebraic* decay of correlations. This is somewhat surprising, as MPS cannot describe these types of correlations, as we argue in Sec. 2.4.

2.4 MPS manifolds

Uniform MPS

We now turn our attention to the states described by MPS of a fixed bond dimension. As we already saw, these states are characterized by a low entanglement entropy. We now explore their properties from the point of view of differential geometry, by viewing them as a manifold embedded in the total Hilbert space.

We focus on the case of a uniform MPS generated by a tensor $A \in \mathbb{C}^D \otimes \mathbb{C}^d \otimes \mathbb{C}^D$, which describes a state directly in the thermodynamic limit:

$|\Psi(A)\rangle =$ 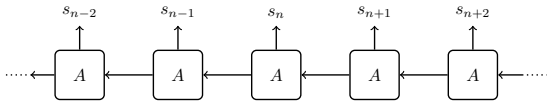 $= \sum_{\vec{s}} \mathrm{Tr}\left(\ldots A^{s_{n-1}} A^{s_n} A^{s_{n+1}} \ldots\right) |\vec{s}\rangle\,.$ (2.20)

The discussion can readily be generalized to the case of finite MPS, as well as generic vector spaces.

The parametrization of the state in Eq. (2.20) has an inherent redundancy, since we can perform a gauge transformation on the virtual degrees of freedom of the form

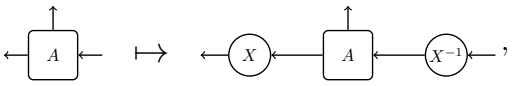 (2.21)

for any invertible matrix X. This gauge redundancy of the MPS parametrization allows us to choose the tensors to fulfill the left-gauge condition without loss of generality

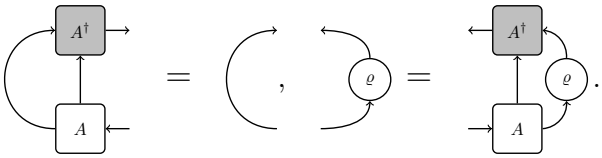 (2.22)

The tensor ϱ is the (positive-semidefinite) right fixed point of the transfer matrix[8]

$\mathbb{E} =$ 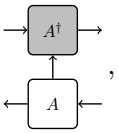 , (2.23)

which encodes the Schmidt values [67]. Hence, we can view the tensor A as a linear map from the right virtual leg to the left virtual and physical legs, which is *isometric*. We will use W to denote this specific mapping, so we can use the notation $W^\dagger W = \mathbb{1}$ to unambiguously specify the isometricity condition.

Hence the tensors A belong the Stiefel manifold [84],

$$\mathrm{St}(n,p) = \left\{ W \in \mathbb{C}^{n\times p} \,\middle|\, W^\dagger W = \mathbb{1} \right\}\,. \tag{2.24}$$

In reality, since there is a unitary freedom remaining in Eq. (2.22)—namely, $A^s \mapsto U^\dagger A^s U$—one can restrict the manifold even further to the Grassmann manifold. The Grassmann manifold should be understood as a quotient manifold, namely all W satisfying the isometricity condition up to a basis rotation, and it is often denoted as $\mathrm{Gr}(n,p) = \mathrm{St}(n,p)/\mathrm{U}(p)$ [84].

Tangent space

This parameter redundancy gives the manifold the structure of a principal fiber bundle [85]. The associated metric is induced by the scalar product in the embedding Hilbert

[8] This assumes the leading eigenvalue of the transfer matrix is unique. This condition is typically known as *injectivity* [75], and excludes all macroscopic superpositions of different MPS. In the rest of this thesis we implicitly assume injectivity of the MPS considered.

space

$$\langle \Psi(\tilde{A}) | \Psi(A) \rangle =$$

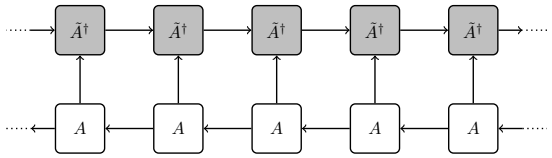

. (2.25)

Notice that this implies the normalization $\|\Psi(A)\|^2 = \operatorname{Tr} \varrho$, since the transfer matrix has the leading eigevectors

$$\lim_{n\to\infty}$$

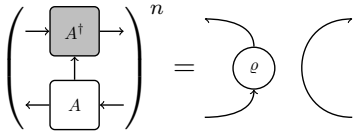

$$= |\varrho\rangle\!\rangle\langle\!\langle \mathbb{1}| \,. \tag{2.26}$$

The transfer matrix gives information about correlations in the system. Indeed, the magnitude of the second leading eigenvalue is related to the *correlation length*, which gives an upper bound on the decay of all possible correlation functions in the system. As a consequence, MPS always have an exponential decay of correlation functions.

To each state $|\Psi(A)\rangle$ we can associate a vector space generated by the infinitesimal variations of the tensor. This is known as the *tangent space*. A generic tangent vector to a uniform MPS is a linear combination of the partial derivatives of the individual tensor components. This can be seen as a vector embedded in Hilbert space, composed of an (infinite) sum of MPS vectors

$$|\Delta(B)\rangle = B\frac{\partial}{\partial A}|\Psi(A)\rangle = \sum_n$$

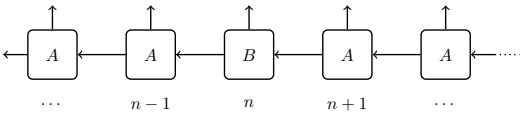

(2.27)

where B contains the coefficients associated to linear combination of partial derivatives and the sum runs over all physical sites.

A tangent vector parametrized by a tensor B also has an inherent gauge freedom to it. The explicit transformation that leaves the vector invariant is

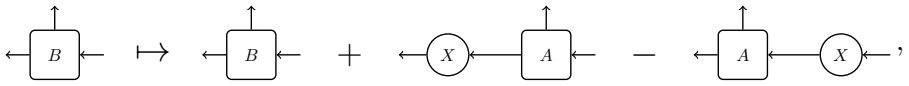

, (2.28)

for any $D \times D$ matrix X. Indeed, the set of derivatives $\partial_A |\Psi(A)\rangle$ form an overcomplete basis. Hence, by introducing the orthogonal complement of A [86], such that

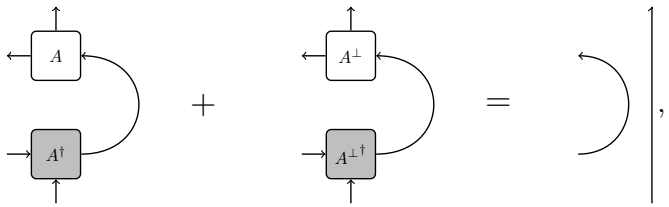

, (2.29)

we can parametrize the tangent vectors as

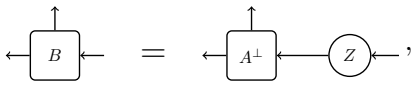

, (2.30)

where Z is a $D(d-1) \times D$ matrix. This parametrization arises quite naturally if one considers the tangent vectors to be embedded in the original Hilbert space. In this case,

the choice of Eq. (2.30) corresponds to imposing orthogonality of the tangent space, $\langle\Psi(A)|\Delta(B)\rangle = 0$. We remark that Eq. (2.30) is exactly the parametrization of the tangent space for Grassmann manifolds, as derived traditionally [84].

This framework is very interesting, as it allows to write evolution equations in the manifold of MPS. Take for example the Schrödinger equation

$$\frac{\partial}{\partial t}|\Psi(A)\rangle = -iH\,|\Psi(A)\rangle$$

for some Hamiltonian H. In general, for some initial state belonging to the MPS manifold, the evolution will immediately yield a state outside of it, making the problem intractable. We can however project into the tangent space, by finding the optimal approximation of the variation $\partial_t|\Psi(A)\rangle$ onto the tangent space

$$\frac{\partial A}{\partial t} = \arg\min_B \big\| \,|\Delta(B)\rangle - iH\,|\Psi(A)\rangle\,\big\|^2 .$$

This leads to a corresponding nonlinear differential equation for A. In analogy to the method developed for Hartree–Fock theory, this technique has introduced the *time-dependent variational principle* (TDVP) [87, 88] in the context of MPS. Using the correct gauge choices, this yields local equations involving the tensor A which can be solved numerically to simulate time-evolution of quantum states.

The projector onto the tangent space is also useful to construct excitation ansätze which can be thought of as a generalization of spin waves to MPS. These states correspond to the eigenstates of an effective projected Hamiltonian, and have been used succesfully to approximate the dispersion relation of the full Hamiltonian. These techniques are reviewed in detail in Ref. [88].

More generally, we can use this formalism to optimize any differentiable function $f(A) \to \mathbb{R}$. As we explain later on, the gradient $\partial_A f(A)$ can be projected onto the tangent plane, and this prescribes a direction to move in the manifold. Any gradient-based optimization can then be adapted to work on Riemannian manifolds. In general it should also be faster than simply constraining the parameters, as we follow the evolution in parameter-space more uniformly, as we know the local metric of our manifold.

The optimization of differentiable functions on Riemannian manifolds has been the object of extensive studies in mathematics and recently these techniques have been applied to TNs [86]. In what follows, we look into some ingredients necessary to optimize a generic function $f(A)$: $\mathrm{Gr}(Dd, D) \to \mathbb{R}$ using gradient-based optimization.

Projection

One particularity arises from the choice of metric in the tangent space. In a general setting it is not always obvious what the correct choice should be, as there is not necessarily a straighforward physical interpretation of the tangent space. In Riemannian manifold optimization, one usually chooses the Euclidean metric [84]:

$$\langle\Delta_1(B_1)|\Delta_2(B_2)\rangle_{\text{Eucl}} = \mathrm{Re}\,\mathrm{Tr}(B_1^\dagger B_2) = \mathrm{Re}$$

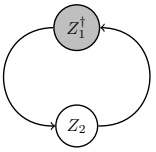

. (2.31)

However, this is not the most natural choice in this setting, since the underlying physical Hilbert space prescribes the metric

$$\langle \Delta_1(B_1)|\Delta_2(B_2)\rangle_{\text{Hilb}} \propto \operatorname{Re}\operatorname{Tr}(B_1^\dagger B_2 \varrho) = \operatorname{Re}$$

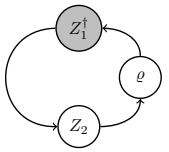

. (2.32)

Note that, as opposed to Eq. (2.31), this metric depends on the current point $|\Psi(A)\rangle$ of the manifold.

Regardless of our choice, the metric allows us to project arbitrary Hilbert space vectors onto the tangent space. For the Euclidean metric in Eq. (2.31), the projection of a tensor Y onto the tangent space of A reads [89]

$$\mathcal{P}_A(Y) =$$

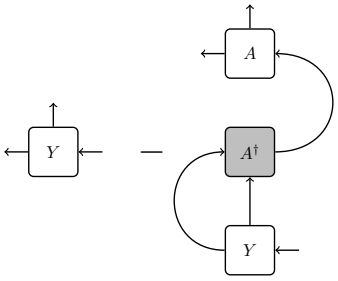

. (2.33)

The projection operator for the Hilbert metric requires inverting the fixed point ϱ, which might lead to numerical instabilities if its singular values are very small.

For the optimization of a generic function $f(A)$, we can compute the gradient $\partial_A f(A)$ without taking into account the isometricity condition and then project onto the tangent space [84]. This projected gradient $\operatorname{grad} f(A) := \mathcal{P}_A\left[\partial_A f(A)\right]$, can be considered as the direction of steepest ascent on the manifold, while its magnitude can be used as a convergence criterion.

Retraction and transport

The last ingredient necessary for a gradient descent algorithm is defining a *retraction*. Loosely speaking, we need to define a curve on the manifold such that we can move in a direction specified by a tangent vector Δ by a step size α. Hence a retraction $\mathcal{R}_A(\alpha\Delta)$ can be any smooth curve such that it (i) starts at A, $\mathcal{R}_A(0) = A$ and (ii) is consistent with $\mathrm{d}\mathcal{R}(\alpha\Delta)/\mathrm{d}\alpha = \Delta$. Different choices of retraction exist, but the most natural choice is a retraction that follows the manifold geodesics, i.e., the shortest path that connects two points on the manifold. Remarkably, the geodesic retraction on a Grassmannian manifold relative to the Euclidean metric is known and is relatively efficient to compute [89]: Given some point A, the retraction of some tangent vector $\Delta = A^\perp Z$ [see Eq. (2.30)] is

$$\mathcal{R}_A(\alpha\Delta) = e^{\alpha Q} A, \tag{2.34}$$

where

$$Q = \begin{pmatrix} A & A^\perp \end{pmatrix} \begin{pmatrix} 0 & -Z^\dagger \\ Z & 0 \end{pmatrix} \begin{pmatrix} A^\dagger \\ A^{\perp\dagger} \end{pmatrix}. \tag{2.35}$$

This constitutes the bare minimum to define a gradient descent algorithm on the Grassmann manifold. In practice, the convergence of gradient descent can be very slow,

and, in Euclidean space, several methods exist that just use first-order information. For example, conjugate gradient adjusts the gradient with the previous search direction, and quasi-Newton methods—notably l-BFGS [90, 91]—uses the previous iterations to create a low-rank approximation of the inverse Hessian. To adapt these methods to optimization on manifolds, it is sufficient to define a *vector transport*, a way of transporting a tangent vector at a previous point of the manifold to the current one. In other words, for a retraction $A' = \mathcal{R}_A(\Delta)$, a vector transport $\mathcal{T}_\Delta(\Omega)$ maps a tangent vector Ω at A to a tangent vector at A'. A typical way of defining transport is via differentiated retraction, i.e.,

$$\mathcal{T}_\Delta(\Omega) = \frac{\mathrm{d}}{\mathrm{d}\alpha}\mathcal{R}_A(\Delta + \alpha\Omega)\Big|_{\alpha=0}. \tag{2.36}$$

Using Eq. (2.34), we obtain

$$\mathcal{T}_{\alpha\Delta}(\Omega) = e^{\alpha Q}\Omega\,. \tag{2.37}$$

2.5 Overview of algorithms

As tensor networks are a language to describe quantum physics, a plethora of algorithms have been introduced in the last years. Nonetheless, there are relatively few algorithms that are well-established, and yet these few have led TNs to obtain some of the state-of-the-art results in many-body quantum physics. In this section we briefly overview some of these algorithms, referring the interested reader to Refs. [92, 93] for an overview of the different methods, and Refs. [16, 39, 67] for a more in-depth discussion on practical implementations.

Ground states

Undoubtedly, the most well-known and successful algorithm for tensor networks is the *density-matrix renormalization group* (DMRG), used for approximating ground states in one dimension as MPS. The name is admittedly a bit of a misnomer, as its original formulation by White [20, 21] was only much later understood in the framework of tensor networks [24, 94]. In its modern formulation, it is a *variational* optimization of the MPS tensors. The variational principle transforms the ground state eigenvalue problem to an optimization of the ground state energy ε_0

$$\varepsilon_0 = \min_\Psi \frac{\langle\Psi|H|\Psi\rangle}{\langle\Psi|\Psi\rangle}\,,$$

where the extremization is performed over some class of ansatz states.

In DMRG, tensors in the chain are sequentially visited, and optimized to minimize the energy keeping all the other tensors fixed. The process is then repeated until convergence. The power of this algorithm lies in the fact that the local optimization is quadratic, and can be solved efficiently with time complexity $O\left(D^3\right)$, where D is the bond dimension. Generalizations to the case of uniform MPS in the thermodynamic limit have been proposed as well [95–97].

One may also wonder how DMRG compares to the manifold optimization in Sec. 2.4. The DMRG method can be interpreted from the manifold perspective as an effective evolution in imaginary time: the evolution equations for each tensor are taken separately and each tensor is evolved sequentially with an infinitely-large time step [87]. Hence it

is a heuristic algorithm, as it optimizes one tensor at a time, as opposed to considering the global energy function. This is discussed in the infinite case in Ref. [86]. Despite this, DMRG has proven to be a very robust and effective method to find ground states of local Hamiltonians. More generally, it can be used to find extremal eigenvalues of operators written as MPOs.

Dynamics

Simulating the dynamics of quantum systems is essential for exploring out-of-equilibrium phenomena, understanding thermalization, as well as constructing thermal states (using imaginary time evolution). Several different approaches exist, and are reviewed in more detail in the Ref. [98]. The most standard approach is known as *time-evolving block decimation* (TEBD) [67, 99] and relies on the decomposition as a series of gates of the time-evolution operator $U = e^{-i\delta t H}$ for some short time step δt. Repeatedly applying these gates to an MPS leads to an exponential increase of the bond dimension, so the state must be *truncated* back down. This truncation can be performed with SVD or other methods described in Ref. [67].

Another method based on the tangent space is TDVP, already mentioned in Sec. 2.4. This method does not require explicit truncation during the evolution, as one is performing the evolution directly on the MPS manifold. While this method has some theoretical advantages, like preserving conserved quantities, in practice it has other disadvantages, as discussed in Ref. [98].

While these methods work well for simulating short-time dynamics, they are all subject to a fundamental limitation, the so-called *entanglement barrier*. In a typical setting, a global quench of a system leads to a linear growth of the entanglement entropy [100, 101], which results in an exponential growth of the required bond dimension [102]. To circumvent this problem, alternative contraction strategies have been proposed in Ref. [103], and have been developed in several subsequent works. This direction is further explored and discussed in Chapter 4.

Higher dimensions

So far, the discussion of algorithms has been focused mostly on MPS. Indeed, the attempt to generalize these methods to two or more dimensions has proved to be very challenging. Early on in the history of DMRG, attempts were made at adapting MPS to two-dimensional problems by wrapping it around the lattice sites in a periodic fashion. This leads however to a more costly representation of the Hamiltonian as an MPO, and generally the bond dimension required grows exponentially with the system size, even in representing area-law states (c.f. Sec. 2.2). PEPS seems to be the right ansatz, but, contrary to MPS, PEPS have the inherent difficulty of not being efficiently contractible, and are typically related to hard computational problems [104]. Nonetheless, over the last ten years, considerable effort has been dedicated to adapting the one-dimensional methods to PEPS, and some methods are becoming the state-of-the-art in tackling two-dimensional problems [105] or even more [106].

In all practical PEPS algorithms, one must find a way of performing an approximate partial contraction of the network to estimate the *environment* around a few sites, i.e. the tensor at the virtual level that is associated with the contraction of an expectation value. This is typically achieved by performing an MPS approximation of the boundary

tensor [107] (typically for finite PEPS) or using the *corner-transfer matrix renormalization group* (CTMRG) [108] for infinite PEPS. In all these methods, the environment is approximated as a TN, so it can be improved on arbitrarily, at the price of a higher computational cost.

Once the environment is calculated, both a variational optimization as well as time-evolution can be performed on local tensors. The gradient of the energy with respect to the local tensor is typically very nonlinear and complicated to calculate, so other heuristics which mimic imaginary time evolution have traditionally been employed [109–113]. Direct variational optimization schemes were introduced in 2016 with two breakthrough papers in Refs. [114, 115]. The direct environment resummation which was introduced is a special case of a more general technique employed in computer science and machine learning, known as *automatic differentiation* [116]. This technique has recently been introduced into the tensor network community [117, 118], and is a versatile tool for computing gradients of tensor networks in a more general setting, and with less coding effort. The development of tensor network algorithms for two (or possibly more) dimensions is still a work in progress, but we expect more exciting breakthroughs and results in the near future.

This chapter is based on the following publication

G. Giudice et al., *Rényi free energy and variational approximations to thermal states*, Physical Review B **103**, 205128 (2021)

CHAPTER 3

RÉNYI FREE ENERGY

3.1 Introduction

From the point of view of thermodynamics, thermal states describe the equilibrium properties of a system. Given a Hamiltonian H, the Gibbs state

$$\rho_G = \frac{1}{Z_G} e^{-\beta H}, \quad Z_G = \operatorname{Tr} e^{-\beta H} \tag{3.1}$$

describes the state of the system at a given temperature $1/\beta$. On the other hand, thermal states arise from the principle of maximum entropy [119, 120]: for a given energy, the thermal ensemble is the one that maximizes the von Neumann entropy $S_G(\rho) = -\operatorname{Tr}(\rho \log \rho)$. Equivalently, this can be formulated as the minimization of the free energy

$$F_G(\rho) = \operatorname{Tr}(H\rho) - \frac{1}{\beta} S_G(\rho), \tag{3.2}$$

so that

$$\rho_G(\beta) = \arg \min_{\substack{\rho \succeq 0 \\ \operatorname{Tr} \rho = 1}} F_G(\rho), \tag{3.3}$$

for some fixed value of β. To keep the notation light, we do not explicitly write the dependence of ρ_G on this parameter. One should keep in mind that the minimum is taken with respect to density operators, i.e. positive-semidefinite operators $\rho \succeq 0$ with a chosen normalization, typically $\operatorname{Tr}(\rho) = 1$. This optimization is not very convenient in practice, since the entropy S_G is often difficult to compute, as it requires information about the entire spectrum of ρ. In a quantum many-body setting, this would require diagonalizing an exponentially large operator, because of the inherent tensor product structure of the Hilbert space.

In the quantum many-body setting, numerical approaches to thermal equilibrium do not try to explicitly solve the optimization above, but resort to different approaches to approximate Eq. (3.1). Monte Carlo methods use sampling to estimate very efficiently the physical properties from Eq. (3.1), but they encounter difficulties in scenarios where

a sign problem appears, as can happen for fermionic models or frustrated systems. A different approach is based on tensor networks (TNs), where the total state corresponds to the contraction of low-rank tensors and allows for a local description of the physics. This is motivated by the fact that thermal states for a local Hamiltonian obey an area law for the mutual information [79, 80], and hence there is strong theoretical evidence that a tensor network description should be efficient at approximating thermal states [38, 72, 80, 81, 121].

In practice, TNs are extremely successful for studying thermal equilibrium. In one spatial dimension, matrix product states (MPSs) can be used to construct a representation of the (mixed) Gibbs state [75, 76, 122–124] or, combined with sampling, to construct minimally-entangled thermal states [125, 126]. Alternatively, the partition function can be represented as a two-dimensional TN, and its contraction can be approximated using tensor renormalization group approaches, for instance, as originally proposed in Refs. [127–129]. The algorithms can also be generalized for two-dimensional systems [130–132].

In this chapter, we study alternative thermodynamic ensembles that, instead of the von Neumann entropy, maximize the α-Rényi entropy [133],

$$S_\alpha(\rho) = \frac{1}{1-\alpha} \log \operatorname{Tr} \rho^\alpha \tag{3.4}$$

at a fixed energy. In the limit $\alpha \to 1$, S_α reduces to the von Neumann entropy. By replacing the von Neumann entropy in Eq. (3.2) by a Rényi entropy, we define the *Rényi free energy*:

$$F_\alpha(\rho) = \operatorname{Tr}(H\rho) - \frac{1}{\beta_\alpha} S_\alpha(\rho). \tag{3.5}$$

We would like to stress that, in general, the extremizer ρ_α of this function is not the thermal ensemble. However, as we will show in Sec. 3.2, this ensemble nonetheless reproduces all local expectation values in the thermodynamic limit. The parameter β_α is not, in general, related to the conventional inverse temperature β, but should be treated as a constant for the optimization.

From a TN perspective, the definition in Eq. (3.5) offers the possibility of directly performing a minimization, since the Rényi entropies in Eq. (3.4) are efficiently computable—at least for small integer values of $\alpha > 1$. In this chapter, we analyze the properties of such ensembles, in particular, how they approximate the thermal properties, and present several variational algorithms which can be used to compute them.

For practical purposes, we will often consider the most convenient case $\alpha = 2$, for which Eq. (3.5) becomes

$$\rho_R = \arg\min_{\rho \succeq 0} F_R, \quad F_R(\rho) = \operatorname{Tr}(H\rho) + \frac{1}{\beta_R} \log \operatorname{Tr} \rho^2, \tag{3.6}$$

where the subscript R represents $\alpha = 2$. In other words, optimizing Eq. (3.6) is equivalent to finding the most mixed state at a chosen energy. In applied mathematics, the optimization of such a function is known as a non-linear semi-definite programming and can be tackled with interior-point methods. However, in many-body quantum physics, the dimension of ρ increases exponentially with the system size, making such approaches impractical for large systems.

This chapter is organized as follows. In Sec. 3.2, we provide an analytical solution to Eq. (3.6), expressed in the eigenbasis of the Hamiltonian. Since the eigenbasis of a

many-body system is not always accessible, we propose an optimization strategy based on uniform MPSs, to approximate the purification of ρ_R directly in the thermodynamic limit. This non-linear optimization can be accelerated using state-of-the-art techniques [86] by restricting it to the Grassmann manifold. This is discussed in detail in Sec. 3.3, and accompanying numerical experiments to benchmark the algorithm are presented. Moreover, we present an alternative technique, based on a non-linear evolution of the density operator in Sec. 3.3, which flows toward the desired ensemble. To conclude, we discuss possible developments in Sec. 3.4.

3.2 Theoretical framework

Maximal Rényi ensemble

We now show the analytical form of the extremizer of Eq. (3.5), which has been previously derived for classical distributions [134–136]. We can use this result in the quantum case, noticing that the state that minimizes Eq. (3.5) must be diagonal in the energy eigenbasis $\{|E_k\rangle\}$ and its eigenvalues are equivalent to a probability distribution.

To find the coefficients $\{p_k\}$ in the density operator $\rho = \sum_k p_k |E_k\rangle \langle E_k|$, $\rho \succeq 0$ which maximizes the Rényi entropy Eq. (3.4) under the constraints $\operatorname{Tr}\rho = 1$ and $\operatorname{Tr}(H\rho) = \bar{E}$, we introduce the Lagrange multipliers β_α and γ_α. The functional $\mathcal{L}$ is then

$$\mathcal{L}(\rho) = \frac{1}{1-\alpha} \log \sum_k p_k^\alpha - \gamma_\alpha \left(\sum_k p_k - 1 \right) - \beta_\alpha \left(\sum_k E_k p_k - \bar{E} \right). \tag{3.7}$$

At the stationary point, the parameter γ_α can be eliminated [134], and we obtain the *maximal Rényi ensemble* (MRE)

$$\rho_\alpha = \frac{1}{Z_\alpha} \Pi_{E_\perp} \left(1 - \beta_\alpha \frac{\alpha - 1}{\alpha} (H - \bar{E}) \right)^{\frac{1}{\alpha-1}} \Pi_{E_\perp}, \tag{3.8}$$

where Z_α is a normalization factor and $\Pi_{E_\perp}$ is a projector onto the eigenvalues below a cutoff energy $E_\perp = \frac{\alpha}{\beta(\alpha-1)} + \bar{E}$ [1]:

$$\begin{aligned} \Pi_{E_\perp} &= \Theta(E_\perp - H), \\ Z_\alpha &= \operatorname{Tr}\left[\Pi_{E_\perp} \left(1 - \beta_\alpha \frac{\alpha - 1}{\alpha} (H - \bar{E}) \right)^{\frac{1}{\alpha-1}} \right], \end{aligned} \tag{3.9}$$

where $\Theta(\cdot)$ is the Heaviside function.

To illustrate the behavior of Eq. (3.8), we show in Fig. 3.1 some characteristics of the different ensembles in a particular finite case. In Figs. 3.1(a) and 3.1(b), we show the distribution of ρ relative to the eigenbasis. The MRE has a distinctive cutoff energy, beyond which the distribution is zero and therefore fairly different from the case of the canonical ensemble. However, in a many-body system, we have to consider that the density of states is not uniform but becomes increasingly peaked in the middle of the spectrum. Then the energy distributions, weighted by the density of states, become much more similar, as seen in Fig. 3.1(b).

[1] Symmetrically, there is also a solution with a projector onto energies above the cutoff energy: $E > E_\perp$. It is the Rényi equivalent of negative temperatures.

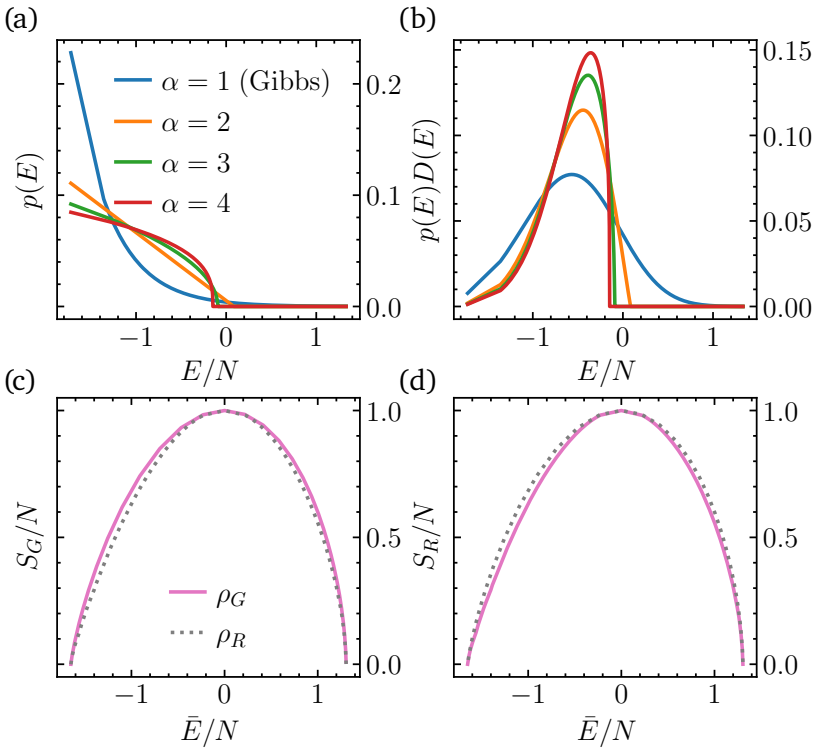

Figure 3.1: (a) Distribution $p(E)$ of the maximal Rényi and Gibbs ensembles for different values of α for the Ising model in Eq. (3.18), with longitudinal and transverse fields, respectively, $h_x = 0.5$ and $h_z = -1.05$ and system size $N = 10$ (PBC). The mean energy $\bar{E}$ is fixed at $-1/4$ of the width of the spectrum. (b) The same distributions weighted with the corresponding density of states $D(E)$, from the approximation in Ref. [137]. Below, the von Neumann (c) and 2-Rényi (d) entropies for the canonical (solid line) and 2-Rényi (dotted line) ensembles are compared at a given mean energy density, for the same system size and Hamiltonian. In both cases, the asymptotic behaviors $\lim_{\beta\to 0} S_G = \lim_{\beta_R\to 0} S_R = N \log 2$ and $\lim_{\beta\to\pm\infty} S_G = \lim_{\beta_R\to\pm\infty} S_R = 0$ are recovered. The branch with negative (positive) mean energy density corresponds to a $\beta > 0$ ($\beta < 0$), corresponding to a solution with a projector onto energies below (above) the cutoff energy $E_\perp$.

Another way of visualizing the relation between the canonical and the Rényi ensembles is to compare their entropies for the same mean energy $\bar{E}$. In Figs. 3.1(c) and 3.1(d), we explicitly show the comparison of von Neumann and 2-Rényi entropies for the ensembles that maximize each of them over the whole energy range for a small system size. While the behavior is qualitatively similar, both ensembles only coincide in the limiting cases $\bar{E} = 0$, when the state is maximally mixed (corresponding to the Gibbs ensemble at infinite temperature $\beta = 0$) and $\bar{E} = E_{\min}$ ($E_{\max}$), when the ensemble reduces to the ground (maximally excited) state, corresponding to $\beta \to +\infty$ ($-\infty$).

To study the behavior at large system sizes, we chose to examine an exactly solvable case, the results of which are in Fig. 3.2. For this Hamiltonian, the density of states becomes Gaussian and the arguments in App. 3.A hold. While we expect that local observables for both ensembles coincide as the system size increases, the same does not

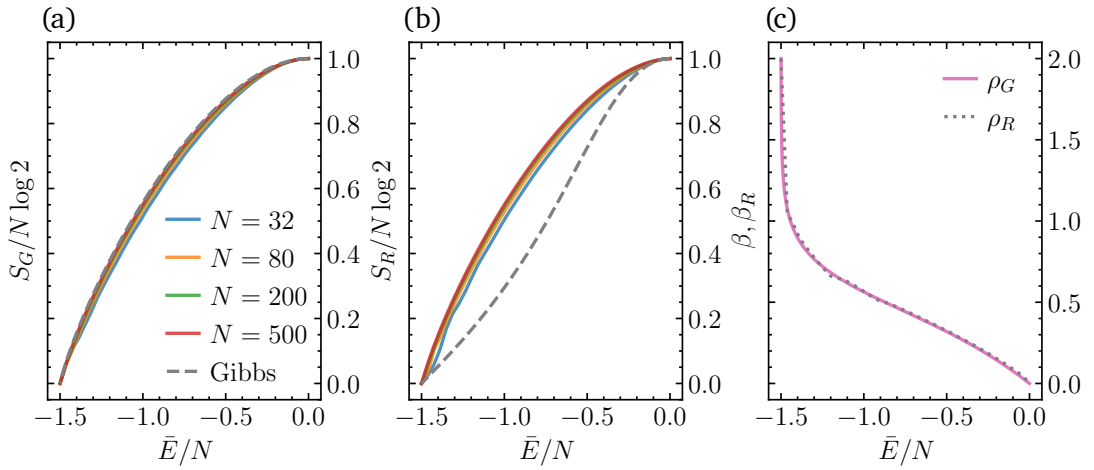

Figure 3.2: (a), (b) Von Neumann and 2-Rényi entropies of ρ_R as a function of mean energy density, for the (classical) Ising model with $h_x = 1/2$, $h_z = 0$. Since there is no visible difference in the curves for ρ_G, only the largest size ($N = 500$) is shown (dashed line). The von Neumann entropy density of the Rényi ensemble approaches that of the Gibbs ensemble, as the system size increases. The two ensembles, however, exhibit a difference at intermediate values of the energy density when comparing their 2-Rényi entropy. (c) Comparison of β and β_R as a function of the mean energy density for the largest size. The correspondence is discussed further in Sec. 3.3.

need to hold for non-local quantities, such as the entropies. It is interesting to notice that the Rényi ensemble has a von Neumann entropy which approaches that of the Gibbs state, and hence will have a free energy—see Eq. (3.2)—which increasingly approaches its minimal value. However, in Fig. 3.2(b), it seems that the same cannot be said when comparing the 2-Rényi entropy of the two ensembles.

Equivalence of local observables

We now consider a one-dimensional quantum system described by a local Hamiltonian H, an operator in the complex Hilbert space $\mathbb{H}$. This total Hilbert space is formed by the tensor product of N local Hilbert spaces:

$$\mathbb{H} = \bigotimes_{n=1}^{N} \mathbb{H}_n \,. \tag{3.10}$$

The Hamiltonian is restricted to be ℓ local, i.e. it can then be written in the form

$$H = \sum_{n=1}^{N} h_n, \tag{3.11}$$

where each h_n acts non-trivially only on sites $n, \ldots, n+\ell-1$, and has finite operator norm. Additionally, we will assume that almost all local terms satisfy $\|h_n\|_{\text{op}} > 0$, such that the spectrum of H is extensive. We mostly consider infinitely large systems, but, when considering finite systems, we specify either open boundary conditions (OBC) or periodic boundary conditions (PBC).

In this setting, it is straightforward to see that the *density of states*

$$D(E) = \frac{1}{|\mathbb{H}|} \operatorname{Tr} \delta(H - E) \tag{3.12}$$

has a variance which scales as $O(\sqrt{N})$. The dimension of the total Hilbert spaces is denoted as $|\mathbb{H}|$. For specific models, such as strictly one-local Hamiltonians, it can be shown that $D(E)$ becomes Gaussian in the thermodynamic limit. Under the assumption of a Gaussian density of states, we can then compute the variance of the energy when we take into account the energy distribution of the ensemble. In the case of the 2-Rényi entropy, it turns out that this can be computed exactly. As described in App. 3.A, the variances $\langle (\Delta H)^2 \rangle_G$ and $\langle (\Delta H)^2 \rangle_R$ both scale as $O(N)$. Hence, if we think about the normalized energy spectrum, both distributions will be increasingly peaked around the same $\bar{E} = \langle H \rangle$ with a standard deviation $O(1/\sqrt{N})$ for large N. Hence, the expectation values of local observables become equivalent in the thermodynamic limit. This derives from the correspondence between microcanonical and canonical ensembles [138]. While there exist counterexamples to this correspondence, a sufficient condition for it to hold is that the mean energy per site converges to a constant [139, 140]. Note that while this argument has been carried out for a Gaussian density of states, we believe that it can be extended to the general case as long as the Hamiltonian is local.

We now turn our attention to the corresponding parameters characterizing the two ensembles. At least in the case of $\alpha = 2$, we find a correspondence $\beta_R \to \beta$ which holds in the thermodynamic limit. This holds asymptotically for large β_R and the range of validity of this approximation increases with system size. Hence, *in the thermodynamic limit*, the β_R for which the Rényi ensemble has the same energy density $\bar{E}$ as a Gibbs ensemble turns out to be the same as the inverse temperature β. This can be shown in the case of a Gaussian density of states (see App. 3.A), and is observed numerically in both integrable and non-integrable models (see Sec. 3.3). This is somewhat surprising, since *a priori* there is no connection between the parameters describing the two different ensembles. From a practical point of view, however, this correspondence is convenient to approximate a thermal ensemble of a sufficiently large system, since we may as well take β_R to be the inverse temperature.

3.3 Variational algorithms for approximating the Rényi ensemble

In this section, we introduce two different possibilities to numerically obtain the Rényi ensemble in Eq. (3.8). Although we have a closed form for the exact solution, its use in a many-body setting is impractical because it would require knowledge of the full energy eigenbasis or of the projector in Eq. (3.8). This motivates the formulation of methods compatible with TN techniques. In Sec. 3.3, we explore how uniform MPSs can be used to form a purification which represents the density matrix, and its individual tensors can be optimized directly by using techniques from Riemannian optimization. In Sec. 3.3, instead, we propose a non-linear evolution which has Eq. (3.8) as a fixed point, so any arbitrary state can be brought to the desired one by simulating this evolution for a sufficient amount of time.

Minimization on the MPS manifold

The optimization problem in Eq. (3.6) can be restricted to the manifold of states described by some class of tensor networks. We consider the class of uniform MPS as in Eq. (2.20), since we can handle states directly in the thermodynamic limit. The method can be applied to finite MPSs as well.

As we saw in Chapter 2, we might consider representing density matrices with an MPO [cf. Eq. (2.13)]

$O =$ 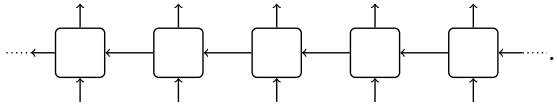 . (3.13)

The issue with this construction is that it is hard to ensure positivity (if the tensors are over the field $\mathbb{C}$ or $\mathbb{R}$), which is a necessary and physical property for objects like density operators. The problem is that positivity is a global property, which cannot be captured in the local tensors [141–143]. Although an MPO ansatz has been used successfully to approximate the stationary points of dissipative dynamics [144, 145], it is problematic for a variational method since there is no way to vary the local tensors without compromising positivity.

An alternative is to introduce a *locally purified state* [75, 141, 146], which guarantees the positivity of the operator for any local tensor. The construction goes as follows. One considers a pure state, where each site has twice the degrees of freedom, which we call *system* and *ancilla*, so the local tensor is

$A =$ 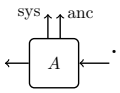

. (3.14)

By tracing out the ancillary degrees of freedom, we obtain a ladder-like TN, which represents the density matrix $\rho = \mathrm{Tr}_{\mathrm{anc}} |\Psi\rangle \langle\Psi|$, or, graphically:

$\rho =$ 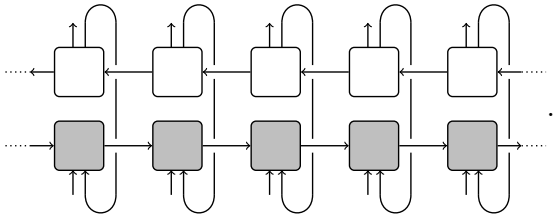 . (3.15)

It is simple to see that this TN is positive semidefinite by construction. The price to pay is that we have introduced a non-linearity in ρ with respect to the local tensors, so even if the objective function is quadratic in ρ, as in Eq. (3.6), it will be quartic in the local tensors. Hence we cannot use linear algebra to iteratively optimize the local tensors, as in the case of the density matrix renormalization group (DMRG) [67]. Nonetheless, we can consider the problem in Eq. (3.6) a non-linear optimization over the tensors of an MPS.

Using the techniques introduced in Sec. 2.4, we can then restrict the purification tensors to the Grassmann manifold, and perform a non-linear optimization. For our application, the objective function is given by Eq. (3.6). For the uniform MPS of Eq. (2.20), it reduces to

$$f_R = \frac{F_R}{N} = \varepsilon + \frac{1}{\beta_R} \log \eta, \tag{3.16}$$

where $\varepsilon = \mathrm{Tr}(H\rho)/N$ is the energy per site and $\eta = \left(\mathrm{Tr}\,\rho^2\right)^{1/N}$ is the purity per site. Both these terms are computable with standard TN routines in polynomial time, for uniform MPSs as well as finite MPSs. The gradient of Eq. (3.16) with respect to A is

$$\frac{\partial f_R}{\partial A} = \frac{\partial \varepsilon}{\partial A} + \frac{1}{\beta_R \eta}\frac{\partial \eta}{\partial A}. \tag{3.17}$$

Both these quantities $\partial\varepsilon/\partial A$ and $\partial\eta/\partial A$ are simple to obtain, as described in App. 3.B. We thus use this gradient information to perform the optimization on the Riemannian manifold using the l-BFGS algorithm [90, 91]. An open-source implementation of the non-linear optimization in JULIA is available online [2].

To conclude, we note that gradient methods cannot guarantee in any way convergence toward the global minimum, but only some local minimum. While Eq. (3.6) has a unique solution in the cone of the positive operators, the same cannot be said on a uniform MPS manifold of fixed bond dimension.

Numerical experiments

For our numerical experiments, we consider the Ising model:

$$H = -\sum_k \left(\sigma_k^x \sigma_{k+1}^x + h_z \sigma_k^z + h_x \sigma_k^x\right). \tag{3.18}$$

When the parallel field vanishes ($h_x = 0$), the model is integrable, and local observables and correlations have a closed form [147, 148]. We use this model to perform the optimization of Eq. (3.6) as described in Sec. 3.3. The parameter β_R is fixed to different values in the interval $\beta_R \in [0, 2]$, and the uniform MPS is optimized until the gradient is sufficiently small [3].

The results of the optimization are shown in Fig. 3.3, where we plot some local observables such as the magnetization $\langle\sigma_i^z\rangle$ and next-neighbor correlation $\Gamma^{a,b} = \langle\sigma_i^a\sigma_{i+1}^b\rangle - \langle\sigma_i^a\rangle\langle\sigma_{i+1}^b\rangle$ as a function of the mean energy density of the ensemble. By increasing the bond dimension, we increase the number of the free parameters, and the numerical results converge toward the thermal ones. Additionally, the comparison of the thermal observables by setting $\beta_R = \beta$ is shown in Fig. 3.3(e). Up to $\beta_R \lesssim 2$, we observe that there is a correspondence between the two ensembles at $\beta_R = \beta$. For $\beta_R \gtrsim 2$, the optimization of Eq. (3.16) converges to the ground space exactly, especially at small bond dimensions. To study the physics of low temperatures, it is therefore more convenient to reexpress the optimization problem in Eqs. (3.6) by introducing a Lagrange multiplier:

$$\rho_* = \arg\min_{\rho\succeq 0}\left\{\ln \mathrm{Tr}\,\rho^2 + \frac{\lambda^2}{2}\left(\mathrm{Tr}(H\rho) - \bar{E}\right)^2\right\}. \tag{3.19}$$

The gradient (see App. 3.B) can be modified accordingly, and the non-linear optimization can be performed in a similar way. This objective function gets rid of the dependence on β_R, and one can directly choose an energy to target, since $\lim_{\lambda\to\infty}\mathrm{Tr}(H\rho_*) = \bar{E}$. However, if one wishes to explore the behavior of some observable with respect to $\bar{E}$, it is not necessary to perform the extrapolation with $\lambda \to \infty$, but a finite λ is sufficient to obtain an energy in the vicinity of the desired value [4].

[2] https://github.com/giacomogiudice/RenyiOptimization.jl

[3] The optimization halts after the norm of the gradient vector in tangent space is smaller than 10^{-6}.

[4] In our simulations, we set $\lambda = 10$. Since the purity per site $0.5 \leq \eta \leq 1$ is order 1, we expect deviations in energy density around $O(1/\lambda^2)$.

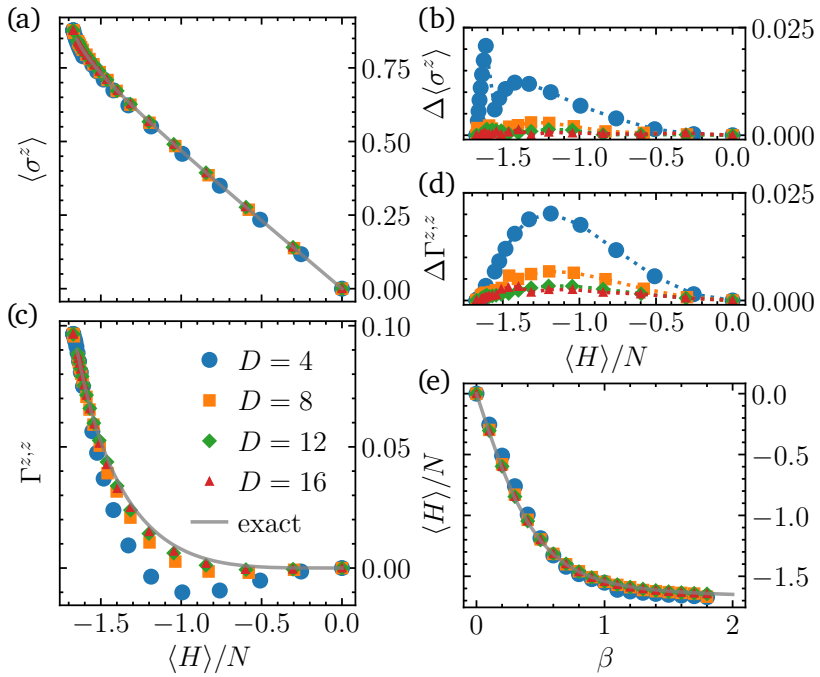

Figure 3.3: Magnetization (a) and next-neighbor correlation $\Gamma^{z,z}$ (b) versus the mean energy density for the Ising model with $h_x = 0$, $h_z = 3/2$, for different bond dimensions D. The dotted line corresponds to the exact results with the same mean energy density. In (c) and (d), the absolute errors to the exact solution are compared. (e) Average energy, choosing $\beta_R = \beta$. No spontaneous symmetry breaking can occur at finite temperature in one-dimensional systems with local interactions—we therefore explicitly enforce the $\mathbb{Z}_2$ symmetry in the tensors.

We also wish to remark that the method is completely general and does not depend on whether the system is integrable or not. To complete our benchmarks, we present in Fig. 3.4 a comparison in the case where a parallel field is introduced, making the system non-integrable. In this case, exact results are not known, but our results are compared to those of an MPS approximation to the Gibbs state purification obtained with a traditional imaginary time evolution method [75, 99]. Since the model does not have a finite-temperature phase transition, the method will behave similarly for any value of the fields. If one chooses $h_x = 0$ and $h_z = 1$, we expect that the required bond dimension increases when $\beta \to \infty$, as the critical ground state is approached [149–152]. In this regime, the cost function in Eq. (3.6) will be dominated by the energy term. Hence the algorithm is reduced to an energy minimization, and we expect it to behave equivalently to other variational methods, such as the one proposed in Ref. [86].

Non-linear evolution

In Ref. [153], the authors introduced a non-linear evolution for approximating the thermal ensemble with Gaussian states. Here we generalize this idea for the Rényi entropies, which gives rise to an evolution that is efficiently computable with TN techniques. We consider a non-linear evolution of a density operator ρ_τ which depends on a real

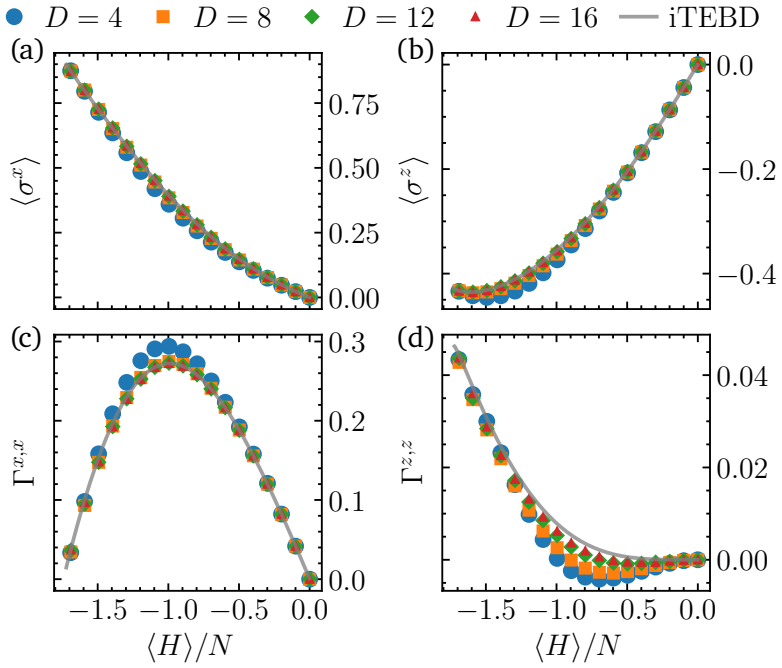

Figure 3.4: (a)–(d) Different observables as a function of the mean energy density for the nonintegrable case with $h_x = 0.5$, $h_z = -1.05$. The dotted line corresponds to the results given by the iTEBD algorithm.

parameter τ

$$\dot{\rho}_\tau = \frac{\partial \rho_\tau}{\partial \tau} = -\frac{1}{2} \left\{ \mathcal{J}_\tau - \langle \mathcal{J}_\tau \rangle , \rho_\tau \right\} . \tag{3.20}$$

The operator $\mathcal{J}_\tau$ can be chosen such that the fixed point of this evolution gives rise to the MRE. For example, the choice

$$\mathcal{J}_\tau[\rho_\tau] = \beta_R H + \frac{2}{\operatorname{Tr} \rho_\tau^2} \rho_\tau \tag{3.21}$$

gives rise to the same density operator as Eq. (3.6). The proof follows similarly from Ref. [153], and it is sufficient to show that the operator $\mathcal{J}_\tau$ in Eq. (3.21) satisfies the following criteria:

$$\operatorname{Tr} \rho_\tau = 1, \ \forall \tau \in \mathbb{R} \qquad \text{trace conservation,} \tag{3.22a}$$

$$\rho_\tau \succeq 0, \ \forall \tau \in \mathbb{R} \qquad \text{positivity conservation,} \tag{3.22b}$$

$$\partial f_R \left(\rho_\tau \right) / \partial \tau \leq 0 \qquad \text{free-energy decrease.} \tag{3.22c}$$

Hence, choosing an appropriate density operator ρ_0 and integrating Eq. (3.20) over a sufficiently long interval, we obtain the solution to Eq. (3.6), since its value can only decrease with time. There is no guarantee of reaching the global minimum—and indeed any eigenstate of H does not evolve under Eq. (3.20)—but a random choice of the initial state should be sufficient in most cases.

We present some numerical experiments on small system sizes in Fig. 3.5, where the energy eigenbasis is available. In all cases, the numerically integrated density operator

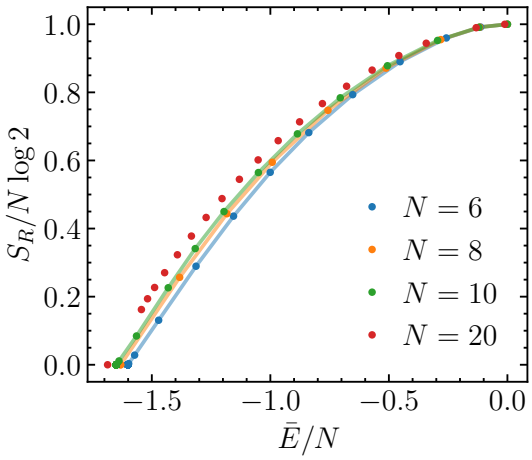

Figure 3.5: 2-Rényi entropy of the maximal Rényi ensemble obtained with the analytic solution (solid lines) and nonlinear evolution (points). Results are for the Ising model (OBC) in Eq. (3.18) with longitudinal and transverse fields, respectively, $h_x = 0.5$ and $h_z = -1.05$. We also show numerical results for $N = 20$ obtained using the non-linear evolution with MPS.

converges to the ensemble in Eq. (3.8). The evolution is discretized by expanding Eq. (3.20) to first order:

$$\rho_{\tau+\delta\tau} \approx e^{-\frac{\delta\tau}{2}(\mathcal{J}_\tau - \langle \mathcal{J}_\tau \rangle)} \rho_\tau e^{-\frac{\delta\tau}{2}(\mathcal{J}_\tau - \langle \mathcal{J}_\tau \rangle)}. \tag{3.23}$$

If the time step is chosen to be sufficiently small, then this evolution will converge to the desired fixed point. This is witnessed by the fact that the Rényi entropy reaches the theoretical maximum for each mean energy, as shown in Fig. 3.5. As a proof of concept, we also perform the integration using MPSs, in particular, using the TDVP scheme [87, 88] to update the state at each time step. In practice, however, we observe that the time step required to obtain accurate results scales unfavourably with the system size, and we have yet to fully understand if the evolution becomes ill-conditioned for large system sizes. Notwithstanding, it is possible that different integration schemes allow for large time steps without compromising the stability of the evolution. We leave this as a venue for future work.

3.4 Outlook

In this chapter, we have introduced an approach to compute thermal expectation values. Instead of attempting to approximate the minimum of the free energy, we construct an ensemble that maximizes the 2-Rényi entropy for the same mean energy, and—in the thermodynamic limit—reproduces local observables of the corresponding Gibbs ensemble.

We have shown that this ensemble can be efficiently approximated using TNs and have presented variational algorithms to obtain such an approximation. It is possible to work directly in the thermodynamic limit and use an MPS representation of the ensemble, which optimizes the objective function in Eq. (3.6). Despite the simple

form of this function, the optimization is non-linear and must be tackled with gradient-based methods. The fundamental reason is that the positivity constraint in TNs is highly non-local, and one way of enforcing it is via a purification. The convergence can be accelerated with techniques from manifold optimization, but a fundamental limitation is the high contraction cost. Indeed, for a purification of bond dimension D, the time complexity involved in computing the purity (see App. 3.B) is $O(D^5)$, which is significantly higher than the typical $O(D^3)$ for other popular MPS algorithms, such as time evolution or ground-state search. Coincidentally, the former is the same leading cost of the original formulation of DMRG with PBCs [154]. Although the time complexity is higher, we observe that a moderate bond dimension captures well the ensemble and its local properties, both in integrable and nonintegrable models.

As an alternative to gradient-based optimization, we also propose an alternative method based on a non-linear evolution of the density operator. Under this evolution, the objective function in Eq. (3.6) is monotonically decreasing, and hence flows to the MRE.

Despite these limitations, we believe more efficient cost functions could be devised. Additionally, the ideas outlined here could be applied to other wave-function ansätze. For example, in recent works [155–158], neural networks have been optimized with variational Monte Carlo to describe the steady state of dissipative dynamics. Such techniques could be adapted to perform the optimization described in this chapter.

Appendices

3.A Calculation of the variance for a Gaussian density of states

In this Appendix, we compute the mean energy $\langle H\rangle$ and variance $\langle(\Delta H)^2\rangle = \langle H^2\rangle - \langle H\rangle^2$ for the Gibbs and 2-Rényi ensembles, assuming the density of states is a Gaussian of the form

$$D(E) \propto \exp\left(-\frac{(E-E_{\text{mid}})^2}{2\sigma^2 N}\right), \tag{3.24}$$

where N is the system size and σ is a constant independent of N. Additionally, without loss of generality, let us assume it is centered at $E_{\text{mid}} = 0$.

For local Hamiltonians as Eq. (3.11), it was shown that the density of states weakly converges to a Gaussian in the thermodynamic limit, as a consequence of Lyapunov's central limit theorem [159–161]. As an alternative proof, one can take an ancillary copy of the system, and consider the state $|\Xi\rangle$, which is the tensor product of maximally entangled pairs between system and ancilla:

$$|\Xi\rangle = \bigotimes_n \frac{1}{\sqrt{|\,\mathbb{H}_n\,|}} \sum_{i=1}^{|\,\mathbb{H}_n\,|} |i\rangle_{\text{sys}}\,|i\rangle_{\text{anc}}\,. \tag{3.25}$$

In the doubled system, the state $|\Xi\rangle$ is a product state, and one can apply directly the Theorem in Ref. [159] to obtain the desired result.

However, the rate of convergence to the central limit theorem is larger than $O(1/\sqrt{N})$, and one should take into account the finite-size corrections when computing expectation values. Hence, we can think of Eq. (3.24) as a toy model of actual local Hamiltonians, and derive results under this assumption.

For the Gibbs ensemble, we have that the partition function is

$$Z_G = \int_{-\infty}^{+\infty} e^{-\beta E} D(E)\,\mathrm{d}E. \tag{3.26}$$

This leads to

$$\langle H\rangle_G = -\frac{\partial}{\partial\beta}\log Z_G = -\beta\sigma^2 N, \tag{3.27a}$$

$$\langle(\Delta H)^2\rangle_G = \frac{\partial^2}{\partial\beta^2}\log Z_G = \sigma^2 N. \tag{3.27b}$$

Working under the assumption of a Gaussian density of states, this results only hold in the region around the peak of the Gaussian, and break down when one tries to take the limit of $\beta \to \infty$.

For the 2-Rényi distribution, we cannot use the trick of deriving the partition function with respect to β, since we cannot interpret it as a generating function. We can however express everything in terms of the truncated moments:

$$\Phi_m = \int_{-\infty}^{E_\perp} E^m D(E)\,\mathrm{d}E. \tag{3.28}$$

The upper integration limit is related to the mean energy and β_R as $E_\perp = \bar{E} + \frac{2}{\beta_R}$. These moments enjoy a recurrence relation of the form $\Phi_{m+2} = \sigma^2\partial\Phi_m/\partial\sigma$. Additionally, Φ_1

is analytical because the integrand is the derivative of a Gaussian. This allows us to establish the identities

$$\Phi_2 = \sigma^2 N \Phi_0 + E_\perp \Phi_1, \tag{3.29a}$$
$$\Phi_3 = \left(2\sigma^2 N + E_\perp^2\right) \Phi_1. \tag{3.29b}$$

By dividing the partition function by $\beta/2$, we can then compute the mean energy for this ensemble as

$$\langle H \rangle_R = \frac{E_\perp \Phi_1 - \Phi_2}{E_\perp \Phi_0 - \Phi_1} = -\sigma^2 N \frac{\Phi_0}{E_\perp \Phi_0 - \Phi_1}. \tag{3.30}$$

Equating this result to $\bar{E}$ allows us to express Φ_0 in terms of Φ_1:

$$\Phi_0 = \frac{\bar{E}}{\bar{E} E_\perp + \sigma^2 N} \Phi_1. \tag{3.31}$$

Using this last relation, we can write the variance as

$$\langle (\Delta H)^2 \rangle_R = \bar{E} E_\perp + 2\sigma^2 N - \bar{E}^2 = 2\sigma^2 N + \frac{2\bar{E}}{\beta_R}. \tag{3.32}$$

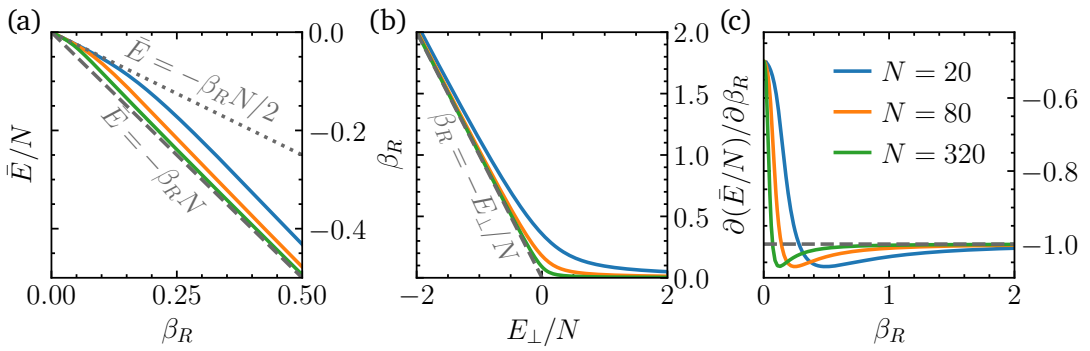

Figure 3.A.1: (a) The energy density of the MRE for a Gaussian density of states as a function of the parameter β_R, for increasing system sizes. For clarity, in all plots we set $\sigma^2 = 1$. In the high-temperature limit ($\bar{E} \to 0$), the behavior $\bar{E} = \beta N/2$ (dotted line) indicates that $\beta_R \approx 2\beta$. However, as the system size is increased, at non-zero energy density the equation of state approaches $\bar{E} = \beta N$, which is analogous to the Gibbs ensemble. Hence, in the limit of $N \to \infty$ we can identify $\beta_R \approx \beta$. This can be understood in (b), for which $\beta_R \approx \max(E_\perp/N, 0) + O(1/\sqrt{N})$. (c) The derivative $\partial(\bar{E}/N)/\partial\beta_R$ has an initially fast-varying regime, corresponding to $E_\perp < 0$, and a second regime at $E_\perp > 0$ approximately constant around -1.

For the Gibbs ensemble, notice that β and $\bar{E}$ are collinear, $\bar{E} = -\beta\sigma^2 N$. At infinite temperature ($\bar{E} = 0$), we have trivially $\beta = \beta_R = 0$. Expanding ρ_G around $\beta = 0$, we obtain $\rho_G \approx 1 - \beta H$. Comparing this with the form of the MRE, we can easily conclude that in this limit $\beta_R \approx 2\beta$. However, one should take into account the thermodynamic limit. Indeed, as shown in Fig. 3.A.1, at non-zero $\bar{E}$, increasing the system size leads to an equation of state which asymptotically approaches $\bar{E} = -\beta_R \sigma^2 N$. This is due to the fact that the cutoff $E_\perp$ becomes proportional to β_R. Indeed, at $E_\perp = 0$, one has that

$\beta_R(E_\perp = 0) = O(1/\sqrt{N})$. The point $E_\perp = 0$ also corresponds to a stationary point of $\partial\bar{E}/\partial\beta_R$. Taking derivatives, one obtains a relation between $\bar{E}$ and β only

$$\frac{\partial \bar{E}}{\partial \beta_R} = \frac{\partial \bar{E}}{\partial E_\perp}\frac{\partial E_\perp}{\beta_R} = \frac{\sigma^2 N}{\beta_R^2}\frac{1 + 2\frac{\bar{E}}{\beta_R \sigma^2 N}}{1 + \frac{\bar{E}}{\beta_R \sigma^2 N}}. \tag{3.33}$$

As the system size is increased, the derivative converges toward a constant, as shown in Fig. 3.A.1. This allows us to conclude that, for a Gaussian density of states and $\beta_R \gg 1/\sqrt{N}$, we have $\beta_R \approx \beta$.

3.B Calculation of the gradient

For simplicity, we assume that the Hamiltonian is two-local and $h_n = h\ \forall N$, but the algorithm can be readily generalized to a non-trivial unit cell and any Hamiltonian which has an MPO form [97]. Once the leading fixed point ϱ is computed, the energy density reduces to the following network:

$\varepsilon =$ 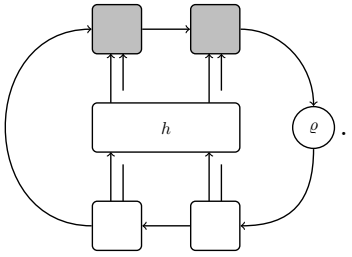

. (3.34)

To compute the derivative $\partial\varepsilon/\partial A^\dagger$ of Eq. (3.34) it is useful to define the left and right environments corresponding to the geometric sum of the terms in the Hamiltonian over each half-infinite chain:

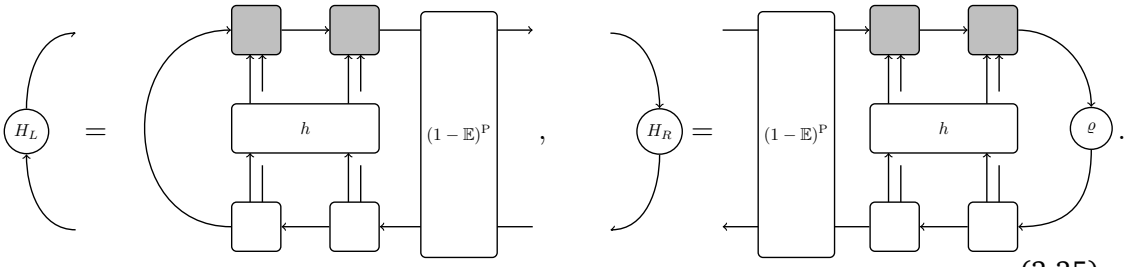

(3.35)

The notation $(1-\mathbb{E})^{\mathrm{P}} = (1-\mathbb{E}+|\varrho\rangle\rangle\langle\langle\mathbb{1}|)^{-1}$ is used to denote the geometric where the divergent part—corresponding to the leading eigenpair—is subtracted [97] [c.f. Eq. (2.23)]. Hence the gradient $\partial\varepsilon/\partial A^\dagger$, without accounting for the constraint, is

$\frac{\partial \varepsilon}{\partial A^\dagger} =$ 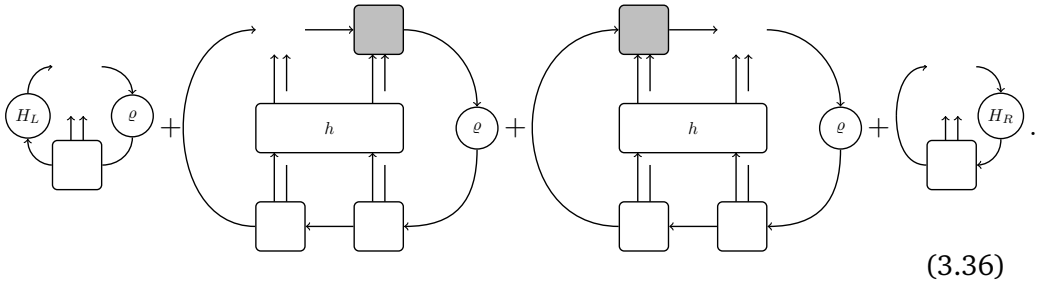

(3.36)

When computing the purity, we can retain the leading eigenvalues and eigenvectors of the transfer element of ρ^2:

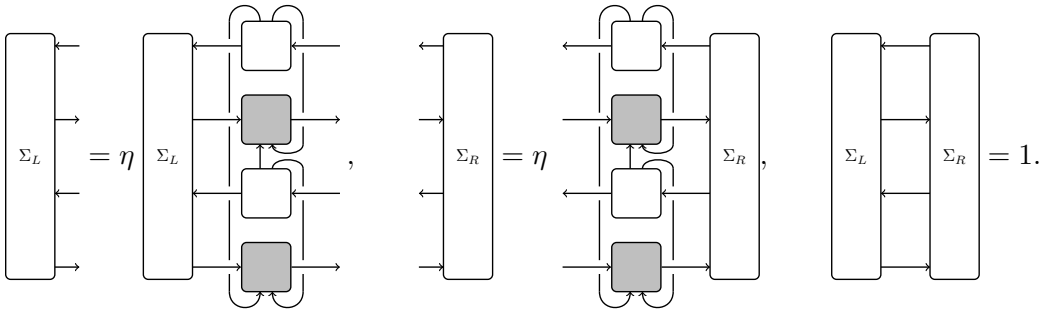

(3.37)

This is by far the costliest computational step relative to the bond dimension D, since it scales as $O(D^5)$, as opposed to the other steps which are all $O(D^3)$. The gradient $\partial\eta/\partial\bar{A}$ becomes

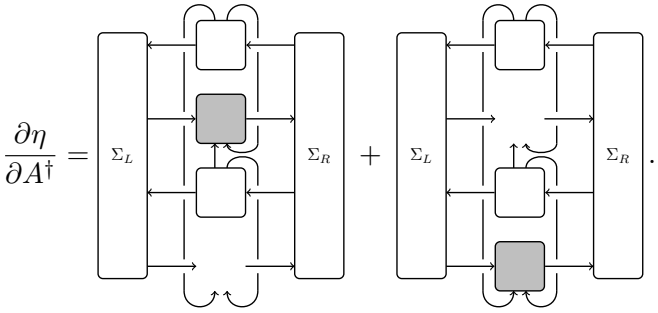

(3.38)

We can then put together Eq. (3.36) and Eq. (3.38) to obtain the gradient $\partial f_R/\partial A^\dagger$ in Eq. (3.17). To compute the gradient on the Grassmann manifold, we must then project the unconstrained gradient using Eq. (2.33).

In practice, we notice that the choice of the metric is not very important for the optimization, and the Euclidean metric poses the advantage of not having to invert a potentially ill-conditioned fixed point ϱ when projecting onto the manifold[5].

[5]Additionally, the use of the Euclidean metric is not necessarily deleterious since, compared to Eq. (2.32), it will magnify the importance of small Schmidt values of the state $|\Psi(A)\rangle$. In Ref. [86], the authors have proposed a non-linear preconditioner that acts as a compromise between these two metrics.

This chapter is based on the following publication

G. Giudice et al., *Temporal Entanglement, Quasiparticles, and the Role of Interactions*, Physical Review Letters **128**, 220401 (2022)

CHAPTER 4

TEMPORAL ENTANGLEMENT

4.1 Introduction

While computing the exact properties of many-body quantum systems out of equilibrium remains a formidable problem, the past decades have witnessed the development of powerful numerical techniques allowing for accurate approximations. This is especially true in one dimension, where the dynamics can be simulated using algorithms based on matrix-product states (MPSs) [67, 103, 162–166]. Even in this case, however, the generic linear growth of the entanglement entropy [100, 167, 168] poses a major obstacle for the MPS representation of the time-evolving state [67].

When one is interested in the dynamics of local observables, it is natural to expect that much of the information encoded in the wave function is irrelevant, and that alternative approaches can be devised retaining only the data needed to reconstruct the local physics. A promising idea in this direction was put forward in Ref. [103] (see also Refs. [169–171]), which proposed an MPS algorithm to describe the dynamics induced on local subsystems. Crucially, the efficiency of the method is insensitive to the growth of the standard entanglement entropy. Instead, it is related to the so-called *temporal entanglement* (TE) [172], which is naturally understood as the entanglement generated along a space-time rotated direction [103]. This approach has recently received renewed interest in connection to the study of space-time dualities in Floquet-kicked Ising chains [173, 174] and dual-unitary quantum circuits [175–179]. In addition, similar ideas motivated related constructions exploiting space-time rotation in generic quantum-circuit dynamics [180–185].

Recently, the approach developed in Ref. [103] has been understood in more physical terms based on the so-called Feynman–Vernon Influence Matrix (IM) approach [172, 186], where one views the system as an environment for its local subsystems. Complete information on the local dynamics is encoded in the IM, which can be thought of as a wave function in a multitime Hilbert space. The TE is the bipartite entanglement entropy of the IM. For time-discrete evolution, it has been argued that the scaling of the TE provides valuable information about the nature of the dynamics [187–190], displaying,

for instance, a slow growth in many-body localized phases [189]. Still, despite a few interesting examples [178, 191–194], our understanding of the TE scaling remains largely incomplete.

As an exception, a detailed characterization of the TE was achieved for *noninteracting* systems, as exemplified by infinite-temperature states in the transverse-field kicked Ising chain [187]. Here, the IM was computed analytically, displaying a Bardeen–Cooper–Schrieffer-like structure, and the corresponding TE entropy was shown to obey an *area-law* scaling. Since the analysis of Ref. [187] relies on a quasiparticle description, it is natural to ask about the fate of the TE area law in the presence of *integrable* interactions, preserving the stable quasiparticles. Besides its interest *per se*, this question has implications for the possibility of efficiently simulating the (discrete) dynamics of interacting integrable models, a task known to be difficult from the analytical viewpoint [195–197].

We tackle this question by studying a family of dynamics corresponding to the Trotterization of the *interacting* XXZ Heisenberg model [198, 199]. We focus on quenches from generic initial states, extending the setting of Ref. [172] to nonequilibrium situations. Based on a quasiparticle picture [100, 101, 195, 200–202], we argue that the TE scaling is sublinear in time. We provide evidence that, while the area law is preserved for a large class of initial states in the noninteracting case, the TE exhibits a typical *logarithmic* growth in the presence of interactions, violating the area law. We conjecture this to be a generic feature of interacting integrable systems, and discuss some interesting questions raised by our results.

4.2 Setup

The model

We consider a spin-$1/2$ chain with L sites and periodic boundary conditions. The discrete dynamics is driven by $\mathcal{U} = \mathcal{U}_{\text{odd}}\,\mathcal{U}_{\text{even}}$, with

$$\mathcal{U}_{\text{odd}} = \prod_{n=1}^{L/2} U_{2n,2n+1}, \quad \mathcal{U}_{\text{even}} = \prod_{n=1}^{L/2} U_{2n-1,2n}\,, \tag{4.1}$$

where

$$U_{n,n+1} = e^{-iJ_x\sigma_n^x\sigma_{n+1}^x - iJ_y\sigma_n^y\sigma_{n+1}^y - iJ'\left(\sigma_n^z\sigma_{n+1}^z - \mathbb{1}\right)} \tag{4.2}$$

is a two-site gate expressed in terms of Pauli matrices. We denote by $|0\rangle_j$, $|1\rangle_j$ the states in the local computational basis. Unless stated otherwise, we will set $J_x = J_y = J$. This model was introduced in Refs. [198, 199] as a paradigmatic example of an integrable, periodically driven spin chain and can be thought of as a Trotterized XXZ Heisenberg evolution. These Floquet dynamics can be represented as a brickwork circuit, cf. Fig. 4.2.1(a). For $J' = 0$, the model reduces to the XY spin chain, mappable to free-fermion dynamics by a Jordan–Wigner transformation, while for $J_x = J_y = \pi/4$ the circuit generated by repeated application of the Floquet operator $\mathcal{U}$ is *dual unitary* [175].

This means that the two-site gate is not only unitary in the conventional sense

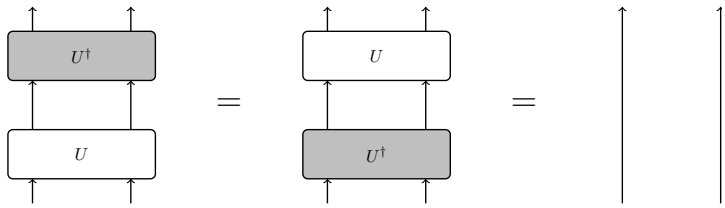

(4.3)

but is unitary under permutation of the legs as well

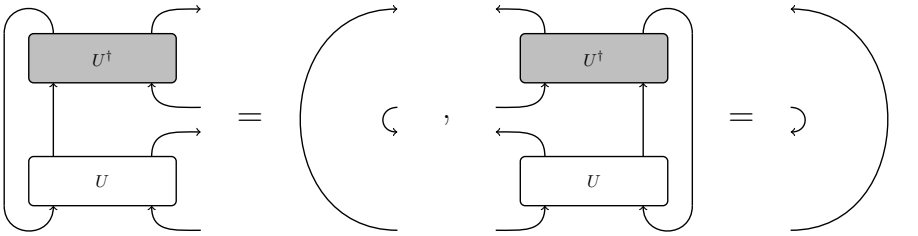

(4.4)

This property is exploited for solving the dynamics at this fine-tuned point. For arbitrary J, J', the system displays an extensive number of local conservation laws [198, 199] and the Floquet spectrum may be obtained exactly via the Bethe ansatz [203, 204]. The corresponding quasiparticle structure bears similarities to that of the well-known XXZ Heisenberg Hamiltonian [203, 205].

The quench protocol and the influence matrix

We study a quench, where the system is initialized in product states (either pure or mixed), and analyze the subsequent evolution in the thermodynamic limit $L \to \infty$. The IM formalism [172, 186] may be introduced starting from the time-evolved expectation value $\mathrm{Tr}\left[\rho(t)O_j\right] = \mathrm{Tr}\left[\rho_0(\mathcal{U}^\dagger)^t O_j \mathcal{U}^t\right]$ of a local observable O_j at site j. Taking for simplicity an initially uncorrelated state, $\rho_0 = \bigotimes_k \rho_0^{(k)}$, the parts of the system to the left and right of j will be treated as *environments*. The IMs associated with them arise from integrating out the environment degrees of freedom, treating the trajectory of spin j as an external parameter. Focusing on the right environment $k > j$, we can write down the IM as a Keldysh path integral, where forward and backward spin trajectories are "folded" on a closed time contour. We introduce a subsystem-environment decomposition $\mathcal{U} = \mathcal{U}_{\mathrm{int}}\mathcal{U}_E$, where $\mathcal{U}_{\mathrm{int}}$ is the gate acting on spins j and $j+1$, and $\mathcal{U}_E$ acts only on spins $k > j$, which can be done in a natural way exploiting the brickwork structure, cf. Fig. 4.2.1(a). Defining the partial matrix elements of $\mathcal{U}_{\mathrm{int}}$ as the operators $[\mathcal{U}_{\mathrm{int}}]_{s,\bar{s}} = [U_{j,j+1}]^s_{\bar{s}}$ acting on spin $j+1$ only (where s, $\bar{s}$ are the input and output states of spin j), the IM $|\mathcal{F}_t\rangle$ is the vector with coordinates depending on the trajectories $\{s_\tau^\pm, \bar{s}_\tau^\pm\}$ as

$$\mathcal{F}_t\left[\bar{s}_\tau^\pm, s_\tau^\pm\right] = \mathrm{Tr}_E\left([\mathcal{U}_{\mathrm{int}}]_{s_t^+,\bar{s}_t^+}\mathcal{U}_E\cdots\mathcal{U}_E[\mathcal{U}_{\mathrm{int}}]_{s_1^+,\bar{s}_1^+}\mathcal{U}_E\rho_0^E\mathcal{U}_E^\dagger\left[\mathcal{U}_{\mathrm{int}}^\dagger\right]_{\bar{s}_1^-,s_1^-}\mathcal{U}_E^\dagger\cdots\mathcal{U}_E^\dagger\left[\mathcal{U}_{\mathrm{int}}^\dagger\right]_{\bar{s}_t^-,s_t^-}\right), \tag{4.5}$$

where $\mathrm{Tr}_E \equiv \mathrm{Tr}_{k>j}$ and $\rho_0^E \equiv \bigotimes_{k>j}\rho_0^{(k)}$, cf. Fig. 4.2.1(a). The superscript $\pm$ labels the forward and backward branch on the Keldysh contour.

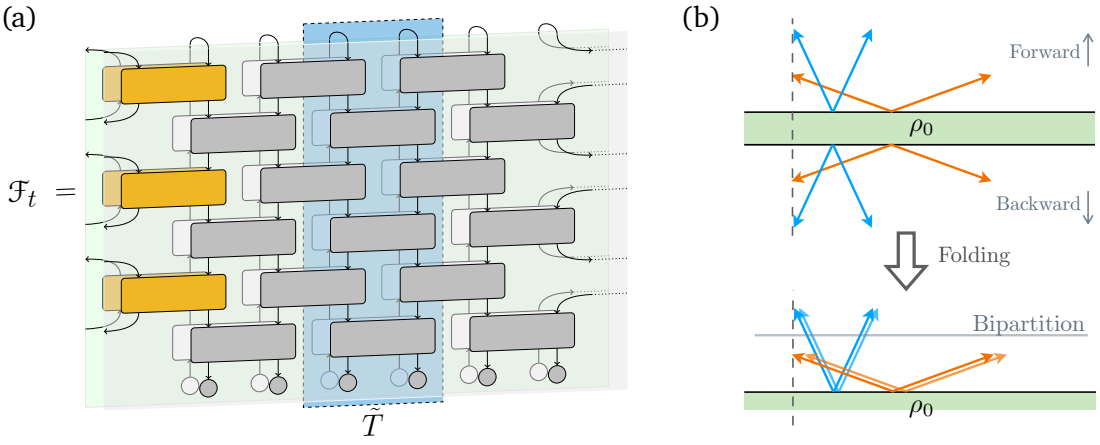

Figure 4.2.1: (a) A system of L qubits is initialized in a product state and evolved via a brickwork quantum circuit, with two-site gate defined in Eq. (4.2). "Folding" the circuit, the left and right IMs determine the evolution of local subsystems. Fixing a site j, the Floquet operator decomposes into $\mathcal{U} = \mathcal{U}_{\text{int}}\mathcal{U}_E$, cf. the main text. In the figure, $\mathcal{U}_{\text{int}}$ consists of the highlighted gates, while the gray and white gates are part of $\mathcal{U}_E$. The operator $\tilde{T}$ defines the dual transfer matrix. (b) Cartoon of the quasiparticle picture for the TE. After folding, backward and forward world lines for each quasiparticle are superimposed, leading to the prediction of sublinear growth for the TE.

The IM of a longer environment can be computed from that of a shorter one, leading to an exact self-consistency equation in the thermodynamic limit [103, 172]. As depicted in Fig. 4.2.1(a), this can be formalized by introducing a dual transfer matrix $\tilde{T}$ generating the evolution in a "rotated direction": the self-consistency equation reads $\tilde{T}\,|\mathcal{F}_t\rangle = |\mathcal{F}_t\rangle$ [103, 169, 172] and completely determines $|\mathcal{F}_t\rangle$.

Temporal entanglement and the quasiparticle picture

The quantity of interest in this chapter is the TE entropy, denoted by $S_\tau(t)$. In order to define it, we consider a bipartition of the multitime Hilbert space of spin trajectories, cut into two regions with time labels $0 \le t' \le \tau$ and $\tau + 1/2 \le t'' \le t$. Here $t', t'' \in (0, t)$ are half integers, as each time step consists of two layers of gates. The TE is the von Neumann entanglement entropy [206] of the state $|\mathcal{F}_t\rangle$ associated with this bipartition across both contours.

We recall that the growth of the standard entanglement entropy after a quantum quench in integrable systems is captured by a well-known quasiparticle picture [100, 101, 195, 200–202]. In essence, one postulates that the quench can be modeled as a process creating at each point in space uncorrelated pairs of entangled quasiparticles spreading through the system with opposite momenta. Given two disjoint regions A and B, their entanglement then grows proportionally to the number of pairs with one quasiparticle in A and the other in B. When supplemented with model-dependent data, this results in a quantitative prediction for the linear growth of the entanglement entropy, which has been proved analytically for noninteracting chains [101] and extensively tested numerically in interacting models [201, 202, 207–209].

Heuristically, we may apply this picture to the TE, cf. Fig. 4.2.1(b). Now for each pair we have to keep track of both the forward and backward evolution. Although these trajectories are correlated, they end up being superimposed in the folded spacetime. As a consequence, given a "space slice", all correlated quasiparticles occupy the same temporal position on the Keldysh contour and quasiparticles are not able to transport entanglement at different time sites. One concludes that no TE is generated between disjoint temporal regions after the quench [1].

A similar heuristic argument already appeared in Ref. [103]. However, there it was stated in terms of noninteracting localized excitations and supported by the analysis of a circuit of swap gates [169]. In contrast, we insist that the picture presented here is in terms of the stable collective quasiparticles of integrable models. As such, it is expected to hold in the scaling limit of large times and to only provide predictions for the leading-order behavior of the TE. That is, the above argument suggests that the TE in integrable systems must asymptotically grow *sublinearly* in time. This prediction is consistent with the TE area law scaling found in Ref. [187] for the infinite-temperature kicked Ising chain

$$\max_{\tau}[S_{\tau}(t)] \leq c\,, \qquad \forall\, t\,, \tag{4.6}$$

where c is a constant. This result was derived by mapping the system to noninteracting fermions and constructing a gapped quasilocal parent Hamiltonian for $|\mathcal{F}_t\rangle$. The area law Eq. (4.6) has been numerically confirmed exploiting a covariance-matrix approach for efficient evaluation. A similar analysis can be carried out in our model for $J' = 0$, for which Eq. (4.1) is mapped onto a free-fermion evolution. In addition, although Eq. Eq. (4.6) was originally shown for infinite-temperature states [187], the covariance-matrix approach can be generalized to any *Gaussian* initial state [cf. App. 4.A], allowing us to confirm Eq. (4.6) for different values of J_x, J_y and various quenches. An example of our data is shown in Fig. 4.2.2.

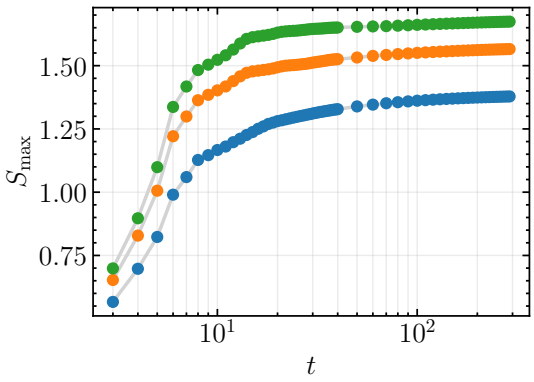

Figure 4.2.2: Growth of the TE for the noninteracting case. In the plot we set $J_x = 0.3, J_y = 0.5, J' = 0$, while the initial state is $\rho_0 = \bigotimes_k \rho_0^{(k)}$, with $\rho_0^{(k)} = e^{-\beta\sigma_k^z}/\mathcal{Z}$ and $\mathcal{Z} = 2\cosh\beta$.

[1] The assumption of the quasiparticles being created in pair is crucial. While this can be justified rigorously for the two-site shift invariant product states considered in this chapter [210, 211], fine-tuned examples are known for which this is not the case [212, 213].

Next, our goal is to test the prediction of the quasiparticle picture and scaling in Eq. (4.6) in the presence of interactions. We provide evidence that, while the TE growth is indeed sublinear in time, interactions bring about logarithmic violations of the area law.

4.3 Results

Exact solution at the dual-unitary point

In principle, integrability allows one to diagonalize the rotated transfer matrix $\tilde{T}$ via the Bethe ansatz and obtain an explicit expression for the IM [214, 215]. However, the resulting wave function is too complicated, and it is not known how to extract the corresponding entanglement.

In order to get some analytical insight, we consider $J = \pi/4$, for which the dynamics is dual unitary [175]. While in this case the TE is vanishing for a class of fine-tuned initial states [178], here we are interested in its behavior for generic ones. To be concrete, we consider a product state $|\Psi_0\rangle = |+\rangle^{\otimes L}$, with $|+\rangle = (|0\rangle + |1\rangle)/\sqrt{2}$, although our results generalize to arbitrary two-site shift invariant states $|\Psi_0\rangle = |\psi\rangle_{1,2} \otimes |\psi\rangle_{3,4} \otimes \cdots \otimes |\psi\rangle_{L-1,L}$.

The Bethe ansatz description remains nontrivial at $J = \pi/4$ [203]. Nonetheless, the form of the gate in Eq. (4.2) becomes simple, allowing us to obtain an exact MPS expression for the IM. Interestingly, we do this avoiding Bethe ansatz techniques and relying instead on methods borrowed from analytical tensor-network theory [11, 193]. We consign the details to App. 4.B, while here we simply report the final result of our analysis. Setting $J' = \pi/4 + K$, we find that the left IM is an MPS of the form

$\langle \mathcal{F}_t| =$ 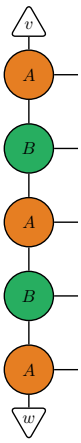

$= \langle v|A^{[1]}B^{[2]}A^{[3]}B^{[4]}\dots A^{[2t-1]}|w\rangle\ .$ (4.7)

Here, A, B are tensors with four physical indices labeled by $00, 01, 10, 11$ and bond dimension $2t+1$. The corresponding matrices are defined by the elements

$$[A^{00}]_{\alpha,\beta} = \delta_{\alpha,\beta} \cos[2K\alpha], \tag{4.8a}$$
$$[A^{01}]_{\alpha,\beta} = \delta_{1,\alpha-\beta} \cos[2K(\alpha-1)], \tag{4.8b}$$
$$[A^{10}]_{\alpha,\beta} = \delta_{1,\beta-\alpha} \cos[2K\beta], \tag{4.8c}$$
$$[A^{11}]_{\alpha,\beta} = [A_{00}]_{\alpha,\beta}, \tag{4.8d}$$

and

$$[B^{00}]_{\alpha,\beta} = \delta_{\alpha,\beta} \exp[2Ki\alpha], \tag{4.9a}$$
$$[B^{11}]_{\alpha,\beta} = \delta_{\alpha,\beta} \exp[-2Ki\alpha], \tag{4.9b}$$
$$[B^{01}]_{\alpha,\beta} = [B_{10}]_{\alpha,\beta} = 0. \tag{4.9c}$$

Here $\alpha, \beta = -t, -(t-1), \ldots, t$. In addition, the boundary vectors are defined by the elements $|v\rangle_\alpha = \delta_{\alpha,0}$ and $|w\rangle_\alpha = 1$. A similar expression holds for the right IM, cf. App. 4.B. As an immediate consequence, we obtain

$$\max_\tau [S_\tau(t)] \leq \ln(2t+1) \sim \ln(t)\,, \tag{4.10}$$

yielding a rigorous proof for the sublinear growth of the TE. Here we employed the fact that the bipartite entanglement entropy of an MPS with bond dimension D is bounded by $\ln D$ [67]. Despite the simplicity of the solution, the TE displays interesting features. First, we find that the asymptotic behavior at large times is not continuous as a function of K. In order to see this, we take $K = \frac{n\pi}{m}$, with n, m coprime integers. In this case, it is easy to see that the MPS in Eq. (4.7) can be *compressed* to one with finite bond dimension: because of the periodicity of the trigonometric functions, the infinite matrices $A^{[i]}$ and $B^{[i]}$ can be truncated to the first m lines and columns, so that the TE is bounded. However, this compression is not possible when K/π is irrational, suggesting a logarithmic growth.

In order to verify this, we evaluated numerically the TE for irrational values of K/π, which can be done efficiently since the MPS form of the IM is known exactly. An example of our data is reported in Fig. 4.3.1(a), providing evidence of a logarithmic growth. We also show the TE corresponding to rational values approximating K/π [2].

To evaluate the entanglement entropy of the exact solution in Eq. (4.39), we resort to numerical calculations with MPS of finite size. While the times accessible with this method are of the order of 10^5, we notice that there can be very large finite-size effects that make the extrapolation of the asymptotic behavior sometimes challenging. As shown in Fig. 4.3.1(b), plateaux of arbitrarily long times can occur when an irrational K is close to a rational approximation with small denominator. Indeed, if an irrational K/π is ϵ-close to a rational number K_{rat}/π with small denominator, the TE for K/π will approximately follow the behavior of K_{rat}/π until a time which increases with $1/\epsilon$. If ϵ is sufficiently small, the curve for K_{rat} may well have saturated before that time, so that the curve for K will display a long initial plateau. An example of this behavior is shown in Fig. 4.3.1(b) for $K/\pi = \sqrt{2}$. In this case, despite an initial plateau, we clearly see an eventual growth for the TE for increasingly better rational approximations of K.

This example shows that, because of the highly fine-tuned nature of the dual-unitary point, the behavior of the TE is extremely irregular in this case. Therefore, our numerical evidence at the dual unitary point should be taken *cum grano salis*. Still, for the accessible time scales, our data consistently point to an indefinite growth of the TE for generic values of J.

Nonetheless, for the accessible timescales, our data consistently point to an indefinite growth of the TE for generic J, thus violating the area law [3].

[2] Increasingly better rational approximations are obtained via a continued-fraction expansion of K/π.

[3] Away from the "singular" dual-unitary point, we find that the TE behaves in a much more regular way (for instance, no area law appears for rational K/π), and we expect that the behavior observed within the accessible time scales is representative of the asymptotic one.

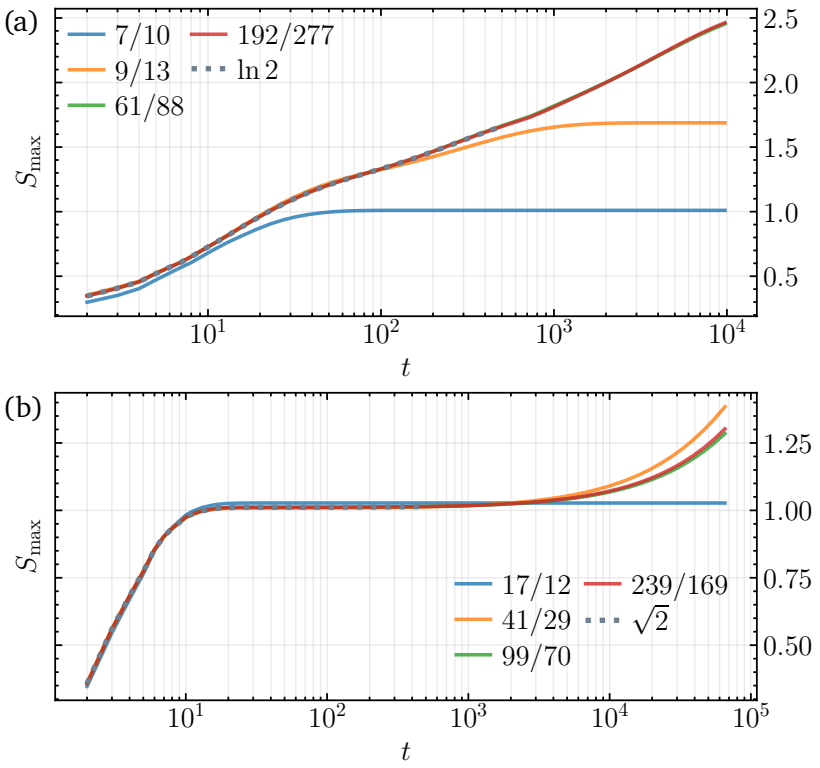

Figure 4.3.1: Maximum TE $S_{\max} = \max_\tau[S_\tau(t)]$ as a function of time at the dual-unitary point $J_x = J_y = \pi/4$ and $J' = \pi/4 + K$ for $K/\pi = \ln(2)$ (a) and $K/\pi = \sqrt{2}$ (b), quenching from $|\Psi_0\rangle = |+\rangle^{\otimes L}$. The plot is obtained evaluating the entanglement entropy of the analytical MPS solution Eq. (4.7). We also show the TE for rational approximations of K/π.

Generic interactions

Away from the dual-unitary point, the IM may be obtained using MPS numerical methods. Following Refs. [103, 169, 172], we represent $\tilde{T}$ as a matrix product operator (MPO), and compute its leading eigenvector using either the density-matrix renormalization group (DMRG) [67], or power methods [103]. In order to push the available simulation times, we focus on initial states displaying $\mathrm{U}(1)$ symmetry, allowing us to enforce it explicitly in the local tensors [216]. Finally, throughout our simulations we used the bond dimension D as a control parameter, checking convergence with respect to it.

We first consider the infinite-temperature state for different values of J, J'. Away from $J = \pi/4$, we find no evidence of a TE area law for rational values of K/π. In general, we observe an initial linear increase of the TE, followed by an eventual logarithmic growth. Our data are shown in Fig. 4.3.2(a): for the available times, curves corresponding to increasing D are seen to converge to a straight line in logarithmic scales.

Next, we turn to the TE from non-equilibrium initial states. In order to preserve $\mathrm{U}(1)$ symmetry, we have chosen the Néel state $|\Psi_0\rangle = |01\rangle^{\otimes L/2}$. Here we observe that the TE is large compared to the infinite-temperature state and increasing as we move away from

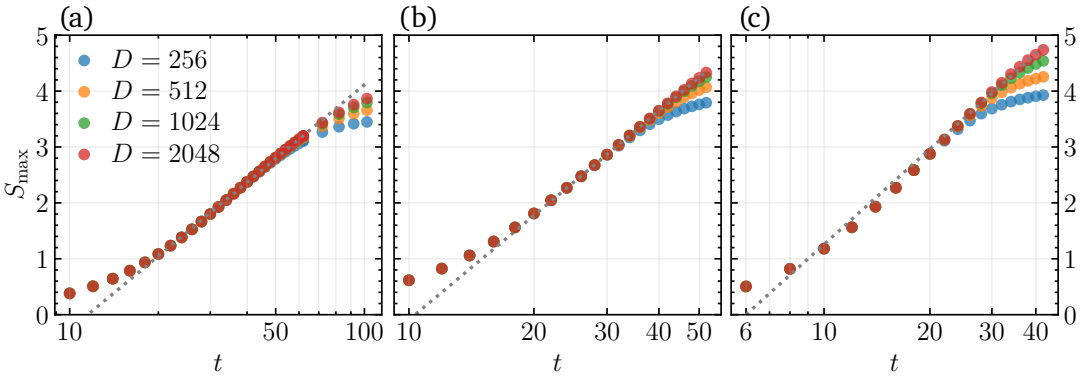

Figure 4.3.2: TE for different values of $J_x = J_y = \pi/4 + \epsilon$ and $J' = 1$. (a) Quench from the infinite-temperature state at $\epsilon = 0.05$. (b)–(c) Same plot for the Néel state $|\Psi_0\rangle = |01\rangle^{\otimes L/2}$ at $\epsilon = 0.05$ (b), $\epsilon = 0.08$ (c). Dotted lines are a guide to the eye to emphasize the logarithmic growth.

the dual-unitary point. The TE is not symmetric around $t/2$, with its maximum generally attained at later times between $t/2$ and t. Its precise location varies with the initial states and parameters. Our numerical data are shown in Figs. 4.3.2(b) and 4.3.2(c). Although simulation times are limited, we observe a convincing logarithmic growth emerging after an initial short-time regime. Altogether, our results consistently point to a typical logarithmic violation of the area law in the presence of interactions, which we conjecture to be a general feature of interacting integrable systems.

4.4 Outlook

We have studied the TE in integrable discrete dynamics. Starting from a heuristic quasi-particle picture and based on analytical and numerical evidence in the XXZ Heisenberg model, we have put forward that the TE generically grows logarithmically in time, violating the area law scaling away from the noninteracting regime.

Our findings raise several questions. First, it would be interesting to put our conjecture on rigorous grounds away from the dual-unitary point. From the computational point of view, instead, it would be important to understand whether and how the sublinear growth of the TE may be exploited for an efficient computation of the IM and its approximation in terms of MPS.

A natural question pertains to the relation between the growth of the TE and the operator-space entanglement entropy (OSEE) of local observables [217, 218]. In fact, the latter was also conjectured to grow logarithmically in integrable systems [218–220]; see Refs. [207, 221–224] for a proof in special cases. However, at the dual-unitary point of Eq. (4.2), the OSEE was shown to satisfy an area law [223]. Therefore, our results suggest that the OSEE is not directly related to the TE: this is consistent with the intuition that the IM bears information beyond the Heisenberg evolution of local observables, see e.g. Refs. [192, 193].

Finally, while we have focused on discrete dynamics, it would be interesting to study the Trotter limit of continuous-time evolution. Preliminary results suggest that the TE

could be *vanishing* in this limit, similarly to the noninteracting case studied in Ref. [187]. This would indicate that a continuous MPS ansatz [225, 226] could be successfully employed in this limit.

Appendices

4.A Computation of the temporal entanglement for free fermions

In this section, we extend the analysis of Ref. [187] to the case of non-equilibrium initial states. We consider the XY-model, defined by Eq. (4.2) with $J' = 0$. In this case the evolution can be mapped to free fermion dynamics and the IM can be computed exactly. We outline this calculation in the following.

As a first step, the spin model is rewritten in terms of fermionic creation and annihilation operators by means of a Jordan-Wigner transformation,

$$\sigma_j^+ = e^{i\pi \sum_{l<j} c_l^\dagger c_l} c_j \qquad \sigma_j^- = c_j^\dagger e^{-i\pi \sum_{l<j} c_l^\dagger c_l} \qquad \sigma_j^z = (1 - 2c_j^\dagger c_j).$$

Making these substitutions in Eq. (4.5), one obtains a trace expression over exponentials with quadratic fermionic operators in the exponent. For its evaluation, it is convenient to cast it into a Grassmann path integral such that Gaussian integration techniques can be applied. To this end, we substitute resolutions of the identity in terms of Grassmann coherent states between all operator products in Eq. (4.5) [187]. In the environment, we introduce the Grassmann fields $\bar{\boldsymbol{\xi}}_\tau^\pm = (\bar{\xi}_{\tau,n=1}^\pm, \bar{\xi}_{\tau,2}^\pm, \dots, \bar{\xi}_{\tau,N}^\pm)^T$ and $\boldsymbol{\xi}_\tau^\pm = (\xi_{\tau,n=1}^\pm, \xi_{\tau,2}^\pm, \dots, \xi_{\tau,N}^\pm)^T$ at all sites n of the environment at time steps $\tau \in \{0, \frac{1}{2}, \dots, t\}$. The superscript $\pm$ labels the forward and backward branch on the Keldysh contour, respectively. Moreover, we define Grassmann fields $\bar{\eta}_\tau^\pm, \eta_\tau^\pm$ with $\tau \in \{1, \dots, t\}$ that analogously describe the degrees of freedom of the system. With this, the IM becomes:

$$\begin{aligned}
&\mathcal{F}_t\left[\{\bar{\eta}_\tau^\pm, \eta_\tau^\pm\}\right] = \\
&\left[\prod_{\tau=0,1/2,\dots}^{t} \mathrm{d}\bar{\boldsymbol{\xi}}_\tau^\pm \mathrm{d}\boldsymbol{\xi}_\tau^\pm\right] e^{+\bar{\boldsymbol{\xi}}_t^+ \bar{\boldsymbol{\xi}}_t^-} \Big(\langle \bar{\eta}_t^+, \bar{\boldsymbol{\xi}}_t^+ | \mathcal{U}_{\text{int}} \mathcal{U}_{\text{odd}} | \eta_t^+, \boldsymbol{\xi}_{t-1/2}^+ \rangle \, e^{-\bar{\boldsymbol{\xi}}_{t-1/2}^+ \boldsymbol{\xi}_{t-1/2}^+} \, \langle \bar{\boldsymbol{\xi}}_{t-1/2}^+ | \mathcal{U}_{\text{even}} | \boldsymbol{\xi}_{t-1}^+ \rangle \\
&\times \langle \bar{\eta}_1^+, \bar{\boldsymbol{\xi}}_1^+ | \mathcal{U}_{\text{int}} \mathcal{U}_{\text{odd}} | \eta_1^+, \boldsymbol{\xi}_{1/2}^+ \rangle \, e^{-\bar{\boldsymbol{\xi}}_{1/2}^+ \boldsymbol{\xi}_{1/2}^+} \, \langle \bar{\boldsymbol{\xi}}_{1/2}^+ | \mathcal{U}_{\text{even}} | \boldsymbol{\xi}_0^+ \rangle \, e^{-\bar{\boldsymbol{\xi}}_0^+ \boldsymbol{\xi}_0^+} \, \langle \bar{\boldsymbol{\xi}}_0^+ | \rho_0^E | \boldsymbol{\xi}_0^- \rangle \, e^{-\bar{\boldsymbol{\xi}}_0^- \boldsymbol{\xi}_0^-} \\
&\times \langle \bar{\boldsymbol{\xi}}_0^- | \mathcal{U}_{\text{even}}^\dagger | \boldsymbol{\xi}_{1/2}^- \rangle \, e^{-\bar{\boldsymbol{\xi}}_{1/2}^- \boldsymbol{\xi}_{1/2}^-} \, \langle \bar{\eta}_1^-, \bar{\boldsymbol{\xi}}_{1/2}^- | \mathcal{U}_{\text{odd}}^\dagger \mathcal{U}_{\text{int}}^\dagger | \eta_1^-, \boldsymbol{\xi}_1^- \rangle \\
&\times \langle \bar{\boldsymbol{\xi}}_{t-1}^- | \mathcal{U}_{\text{even}}^\dagger | \boldsymbol{\xi}_{t-1/2}^- \rangle \, e^{-\bar{\boldsymbol{\xi}}_{t-1/2}^- \boldsymbol{\xi}_{t-1/2}^-} \, \langle \bar{\eta}_t^-, \bar{\boldsymbol{\xi}}_{t-1/2}^- | \mathcal{U}_{\text{odd}}^\dagger \mathcal{U}_{\text{int}}^\dagger | \eta_t^-, \boldsymbol{\xi}_t^- \rangle \Big).
\end{aligned} \tag{4.11}$$

To evaluate the single terms in Eq. (4.11), we first note that

$$\langle \bar{\eta}, \bar{\boldsymbol{\xi}} | \mathcal{U}_{\text{int}} \, \mathcal{U}_{\text{odd}} | \eta, \boldsymbol{\xi} \rangle = \langle \bar{\eta}, \bar{\xi}_{n=1} | \mathcal{U}_{\text{int}} | \eta, \xi_{n=1} \rangle \, \langle \bar{\tilde{\boldsymbol{\xi}}} | \mathcal{U}_{\text{odd}} | \tilde{\boldsymbol{\xi}} \rangle \ , \tag{4.12}$$

where $\bar{\tilde{\boldsymbol{\xi}}}$ and $\tilde{\boldsymbol{\xi}}$ contain only Grassmann variables for $n > 1$. Next, the Grassmann kernel of the two-site gates need to be evaluated. For the XY-model with $U_{n,n+1} = \exp\left(-iJ_x \sigma_n^x \sigma_{n+1}^x - iJ_y \sigma_n^y \sigma_{n+1}^y\right)$, they read

$$\begin{aligned}
&\mathcal{F}(\bar{\xi}_n, \bar{\xi}_{n+1}, \xi_n, \xi_{n+1}) = \langle \bar{\xi}_n, \bar{\xi}_{n+1} | U_{n,n+1} | \xi_n, \xi_{n+1} \rangle \\
&= \cos(J_x - J_y) \exp\Big[- i \tfrac{\sin(J_x+J_y)}{\cos(J_x-J_y)} (\bar{\xi}_n \xi_{n+1} + \bar{\xi}_{n+1} \xi_n) \\
&+ i \tan(J_x - J_y)(\bar{\xi}_{n+1} \bar{\xi}_n + \xi_n \xi_{n+1}) - 2 \tfrac{\sin J_x \sin J_y}{\cos(J_x-J_y)} (\bar{\xi}_n \xi_n + \bar{\xi}_{n+1} \xi_{n+1}) \Big] e^{\bar{\xi}_n \xi_n + \bar{\xi}_{n+1} \xi_{n+1}},
\end{aligned} \tag{4.13}$$

where we have suppressed the labels for the time index and Keldysh branch. Furthermore, for a thermal initial state of the form $\rho_0^E = \bigotimes_{n=1}^N e^{-\beta\sigma_n^z}$ (we neglect normalization here since it is not relevant for our purpose), we find for the Grassmann kernel of the initial state: $\langle\bar{\boldsymbol{\xi}}|\rho_0^E|\boldsymbol{\xi}\rangle = e^{-\beta}\exp\left(e^{2\beta}\sum_{n=1}^N \bar{\xi}_n\xi_n\right)$. Making the appropriate substitutions in Eq. (4.11), one arrives at an integral of the form

$$\mathcal{F}_t(\{\bar{\eta}_\tau,\eta_\tau\}) \sim \left[\prod_{\tau=0,1/2,\ldots}^{t} \mathrm{d}\bar{\boldsymbol{\xi}}'_\tau \mathrm{d}\boldsymbol{\xi}'_\tau\right]\left(\exp\left[\frac{1}{2}\sum_{\tau,\tau'=0,1/2,\ldots}^{t}\begin{pmatrix}\bar{\boldsymbol{\xi}}'_\tau\\ \boldsymbol{\xi}'_\tau\end{pmatrix}^T \boldsymbol{A}_E^{(\tau,\tau')}\begin{pmatrix}\bar{\boldsymbol{\xi}}'_{\tau'}\\ \boldsymbol{\xi}'_{\tau'}\end{pmatrix}\right]\right.$$
$$\left.\times\exp\left[\sum_{\tau,\tau'=1}^{t}\begin{pmatrix}\bar{\boldsymbol{\eta}}_\tau\\ \boldsymbol{\eta}_\tau\end{pmatrix}^T \boldsymbol{A}_S^{(\tau,\tau')}\begin{pmatrix}\bar{\boldsymbol{\eta}}_{\tau'}\\ \boldsymbol{\eta}_{\tau'}\end{pmatrix}\right]\exp\left[\sum_{\substack{\tau=1\\ \tau'=0,1/2,\ldots}}^{t}\begin{pmatrix}\bar{\boldsymbol{\eta}}_\tau\\ \boldsymbol{\eta}_\tau\end{pmatrix}^T \boldsymbol{A}_{\mathrm{int}}^{(\tau,\tau')}\begin{pmatrix}\bar{\boldsymbol{\xi}}'_{\tau'}\\ \boldsymbol{\xi}'_{\tau'}\end{pmatrix}\right]\right), \tag{4.14}$$

where we defined $\boldsymbol{\xi}'_\tau \equiv (\boldsymbol{\xi}^+_\tau, \boldsymbol{\xi}^-_\tau)^T$ and $\boldsymbol{\eta}_\tau \equiv (\eta^+_\tau, \eta^-_\tau)^T$ (and analogously for the variables with a bar). The matrices $\boldsymbol{A}$ come from rewriting Eq. (4.13) as a quadratic form. Using standard relations for Gaussian Grassmann integrals, Eq. (4.14) can be rewritten as:

$$\mathcal{F}_t(\{\bar{\eta}_\tau,\eta_\tau\}) \sim \exp\left[\sum_{\tau,\tau'=0}^{t}\begin{pmatrix}\bar{\boldsymbol{\eta}}_\tau\\ \boldsymbol{\eta}_\tau\end{pmatrix}^T \boldsymbol{B}^{(\tau,\tau')}\begin{pmatrix}\bar{\boldsymbol{\eta}}_{\tau'}\\ \boldsymbol{\eta}_{\tau'}\end{pmatrix}\right], \tag{4.15}$$

with

$$\mathbf{B}^{(\tau,\tau')} = \mathbf{A}_S^{(\tau,\tau')} + \frac{1}{2}\left(\mathbf{A}_{\mathrm{int}}\mathbf{A}_E^{-1}\mathbf{A}_{\mathrm{int}}^T\right)^{(\tau,\tau')}. \tag{4.16}$$

The state in Eq. (4.15) can be represented as BCS wavefunction of the form $|\mathcal{F}_t\rangle \propto \exp(\sum_{i,j} B_{ij}\hat{c}_i^\dagger\hat{c}_j^\dagger)\,|\emptyset\rangle$, from which we can infer the correlation matrix Λ that uniquely determines the IM. The correlation matrix Λ depends only on the matrix $\mathbf{B}$ and is independent of the normalization of $|\mathcal{F}_t\rangle$ in particular. By defining a bipartition of the system in temporal direction and viewing one part as subsystem, one can compute the TE from the reduced correlation matrix of that subsystem [227]. In Fig. 4.2.2, we show the *maximal* TE, i.e. for each physical evolution time t, we choose the temporal cut in such a way that the TE is maximized.

4.B Exact solution at the dual-unitary point

Here we outline the calculations leading to the exact MPS representation for the IM at the dual-unitary point. We consider the following parametrization for the two-site gate

$$U_{1,2}[K] = e^{-i\left[\frac{\pi}{4}\sigma_1^x\sigma_2^x + \frac{\pi}{4}\sigma_1^y\sigma_2^y + \left(\frac{\pi}{4}+K\right)\sigma_1^z\sigma_2^z\right]}. \tag{4.17}$$

This can be rewritten as

$$U_{1,2}[K] = S\exp\left[-iK\sigma_1^z\sigma_2^z\right] = \exp\left[-iK\sigma_1^z\sigma_2^z\right]S, \tag{4.18}$$

where S is the swap operator. We focus on quantum quenches from two-site shift invariant product states $|\Psi_0\rangle = |\psi\rangle_{1,2}\otimes|\psi\rangle_{3,4}\otimes\cdots\otimes|\psi\rangle_{L-1,L}$. Although the method presented

in the following can be extended to generic $|\psi\rangle_{j,j+1}$, here we consider the simplest case where $|\Psi_0\rangle$ is one-site shift invariant, and choose for concreteness $|\Psi_0\rangle = |+\rangle^{\otimes L}$, where $|+\rangle = (|0\rangle + |1\rangle)/\sqrt{2}$.

We start by analyzing the folded circuit, which we represent pictorially (for $t = 2$) as

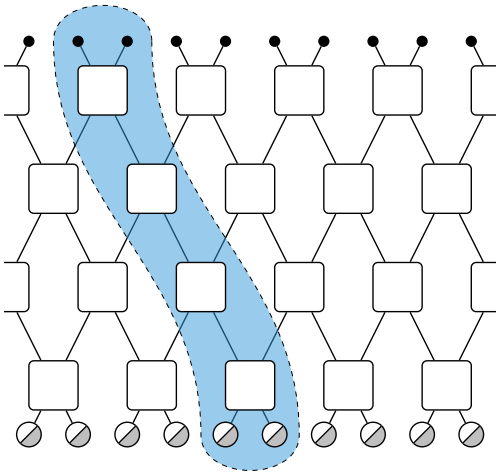

(4.19)

where black dots denote the folded identity, while two-tone circles correspond to the folded product state $|+\rangle\,|+\rangle$. Before tackling the computation of the IM, it is convenient to analyze the so-called light-cone transfer matrix, indicated in Eq. (4.19) by a shaded area. It was introduced in Ref. [228] and it is easy to see that its right fixed point is always a product state of maximally entangled Bell pairs.

In order to compute the left fixed point, we will make use of a graphical "zipper-equation", which appeared in Ref. [11] in the context of the classical asymmetric exclusion process. There, it was presented as a tensor-network reformulation of the solution found in Ref. [28]. In the literature of quantum quenches, zipper equations of similar form were previously exploited to obtain analytical results in interacting quantum cellular automata [192–194].

As a starting point, we first look for a solution of the fixed-point equation for a formally infinite transfer matrix. Supposing that the time direction has no boundaries, we may interpret the transfer matrix as obtained by sequential application of the dual gates as

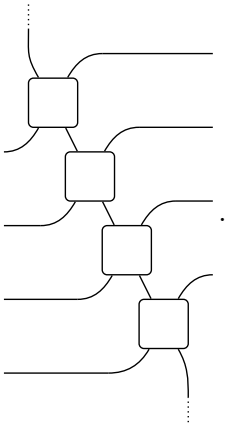

(4.20)

We assume that in the bulk the fixed point can be written as an MPS with the same tensor A at each site (its graphical form is given in Eq. (4.33) below). Following [11],

we observe that a sufficient condition to find a solution is that there exists a tensor B which satisfies the zipper equation

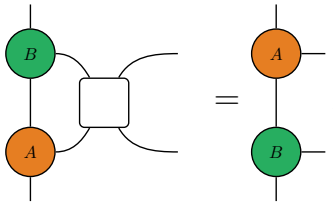

(4.21)

Of course, for a finite time t, the light-cone transfer matrix has boundaries, which have to be taken into account. Denoting by $\langle v|$ and $|w\rangle$ the boundary vectors of the MPS, one can see that the following give a sufficient condition for the MPS to be a left fixed point

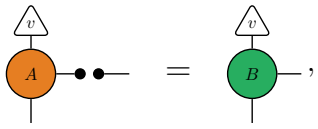

(4.22a)

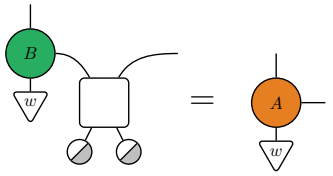

(4.22b)

In the following, we use k to label the four local basis states in the folded picture, i.e. $k = 00, 01, 10, 11$. We will find a solution to the bulk and boundary equations Eqs. (4.21) and (4.22), automatically yielding an MPS solution for the left fixed point.

We note that the first of the boundary conditions in Eq. (4.22) does not depend on the initial state. It states that $\langle v| B_k = 0$ for $k \neq 00, 11$. We thus set $B_{01} = B_{10} \equiv 0$, for which it is automatically satisfied. Next, we introduce

$$f(k,\ell) = \begin{cases} 0 & \text{if } \ k,\ell \in \{00,11\} \\ & \text{or } \ k,\ell \in \{01,10\} \\ (-1)^{s(k)+s(\ell)} & \text{otherwise}\,, \end{cases}$$

where $s(00) = s(10) = 1$, $s(01) = s(11) = 0$. Eq. (4.21) can be rewritten as

$$A_k B_\ell = B_\ell A_k e^{2iKf(k,\ell)}\,. \tag{4.23}$$

Let λ_0 be an eigenvalue of B_{00} with eigenvector $|\lambda_0\rangle$. Assuming $\lambda_0 \neq 0$, $A_{00}^r |\lambda_0\rangle \neq 0$, we have that $A_\alpha^r |\lambda_0\rangle$ is an eigenstate of B_{00} with eigenvalue e^{-2iKr}. Excluding the special case where K/π is a rational number, the eigenvalues e^{-2iKr} are all different, implying that B_{00} must be infinite dimensional. We thus introduce the ansatz

$$B_{00} = \mathrm{diag}(\ldots, e^{-4iK}, e^{-2iK}, 1, e^{2iK}, e^{4iK}, \ldots)\,. \tag{4.24}$$

Now, A_{00} and A_{11} commute with B_{00}, and since all its eigenvalues are different, they must be diagonal in the same basis, namely

$$A_{00} = \mathrm{diag}(\ldots, a_{-1}, a_0, a_1 \ldots)\,, \tag{4.25a}$$
$$A_{11} = \mathrm{diag}(\ldots, a'_{-1}, a'_0, a'_1 \ldots)\,. \tag{4.25b}$$

On the other hand, A_{00} and A_{11} also commute with B_{11}, which we can thus take diagonal in the same basis

$$B_{11} = \mathrm{diag}(\ldots, b_{-1}, b_0, b_1 \ldots)\,, \tag{4.26}$$

where b_k must be determined. Next, using that A_{01}, and A_{10} permute the eigenvectors of B_{00} cyclically [which follows from Eq. (4.23)] they must take the form

$$[A_{01}]_{\alpha,\beta} = \delta_{1,\alpha-\beta}\tilde{a}_\beta\,, \qquad \alpha,\beta \in \mathbb{Z}\,, \tag{4.27a}$$
$$[A_{10}]_{\alpha,\beta} = \delta_{1,\beta-\alpha}\tilde{a}'_\alpha\,, \qquad \alpha,\beta \in \mathbb{Z}\,. \tag{4.27b}$$

Eq. (4.27), together with the commutation relations Eq. (4.23), allow us to fix the coefficients b_α in Eq. (4.26), yielding

$$B_{11} = b_0\,\mathrm{diag}(\ldots, e^{4iK}, e^{2iK}, 1, e^{-2iK}, e^{-4iK}, \ldots)\,.$$

where b_0 is an overall constant. As will be manifest later on, for the initial state chosen we can set $b_0 = 1$.

It remains to fix the constants in Eqs. (4.25) and (4.27) and the vectors $\langle v|$, $|w\rangle$. Using Eq. (4.22b) for $k = 00, 11$, we obtain

$$[A_{00}]_{\alpha,\beta} = [A_{11}]_{\alpha,\beta} = \frac{1}{2}\cos(2K\alpha)\delta_{\alpha,\beta}\,. \tag{4.28}$$

Next, using Eq. (4.22a), we get

$$|v\rangle = (\ldots, 0, 0, 1, 0, 0 \ldots)\,. \tag{4.29}$$

Now, Eq. (4.22b) for $k = 10$ reads

$$\frac{1}{4}(B_{00}e^{2iK} + B_{11}e^{-2iK})\,|w\rangle = A_{10}\,|w\rangle\ .$$

Using Eq. (4.27) and after a little guess work, we immediate see that a solution is given by

$$|w\rangle = (\ldots, 1, 1, 1, \ldots)\,, \tag{4.30}$$

and

$$[A_{10}]_{\alpha,\beta} = \frac{1}{2}\delta_{1,\beta-\alpha}\cos[2K\beta]\,. \tag{4.31}$$

Similarly, repeating the same steps for $k = 01$, we have

$$\frac{1}{4}(B_{00}e^{-2iK} + B_{11}e^{2iK})\,|w\rangle = A_{01}\,|w\rangle\ ,$$

which straightforwardly yields

$$[A_{01}]_{\alpha,\beta} = \frac{1}{2}\delta_{1,\alpha-\beta}\cos[2K(\alpha-1)]\,, \tag{4.32}$$

completely fixing the tensors of left fixed point.

Although the MPS solution which we have found is defined in terms of infinite-dimensional matrices, it is immediate to see that the boundary conditions allow one to

truncate them at each finite time t. Putting all together, for a given time t, we have that the left fixed point of the light-cone transfer matrix is given by the MPS

$\langle L_{\mathrm{LC}}| =$ 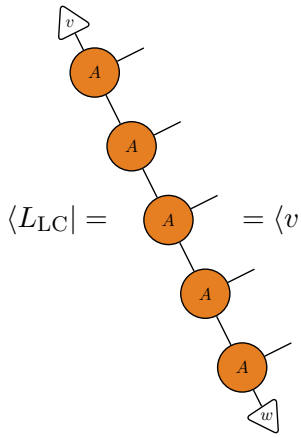 $= \langle v| \underbrace{AA\ldots A}_{2t-1} |w\rangle \ ,$ (4.33)

where $v_\alpha = \delta_{\alpha,0}$, $w_\alpha = 1$ and (dropping an overall factor $1/2$)

$$[A_{00}]_{\alpha,\beta} = \delta_{\alpha,\beta} \cos[2K\alpha] \,, \tag{4.34a}$$
$$[A_{01}]_{\alpha,\beta} = \delta_{1,\alpha-\beta} \cos[2K(\alpha-1)] \,, \tag{4.34b}$$
$$[A_{10}]_{\alpha,\beta} = \delta_{1,\beta-\alpha} \cos[2K\beta] \,, \tag{4.34c}$$
$$[A_{11}]_{\alpha,\beta} = [A_{00}]_{\alpha,\beta} \,, \tag{4.34d}$$

with $\alpha, \beta = -(2t-1), -(2t-2), \ldots, 2t-2, 2t-1$. We will use the above result to obtain the left IM. We start by the explicit representation for the left fixed point of the light-cone ($\langle L_{\mathrm{LC}}|$) and standard ($\langle L|$) transfer matrices in terms of the two-site gates, reading (for $t = 3$)

$\langle L_{\mathrm{LC}}| =$ 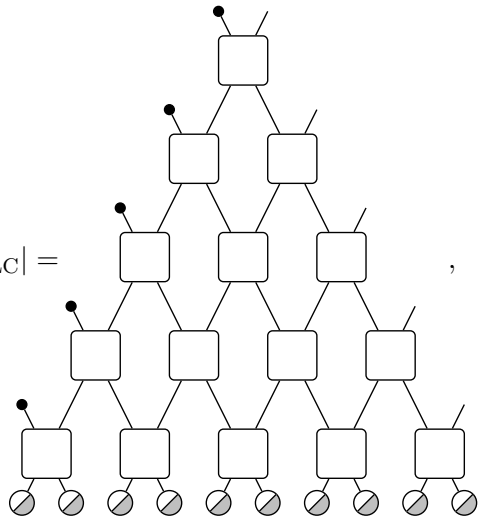 , $\langle L| =$ 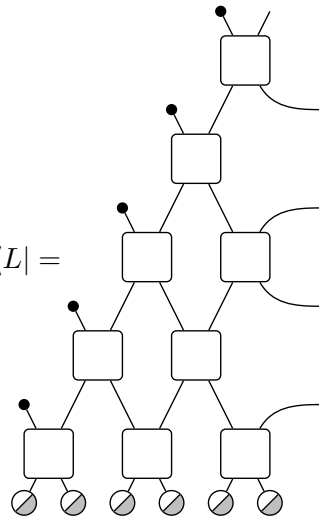 . (4.35)

We recognize that the bottom-left corner of $\langle L|$ is the fixed point of the light-cone transfer

matrix for a shorter time. Therefore, using our previous result, we have

$\langle L| =$ 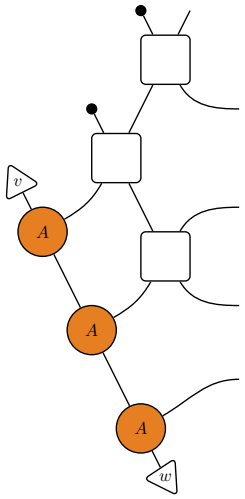

. (4.36)

It is straightforward to see that the tensor B satisfies the identity

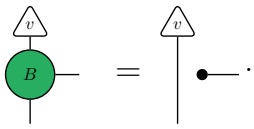

. (4.37)

Applying it to Eq. (4.21), this yields

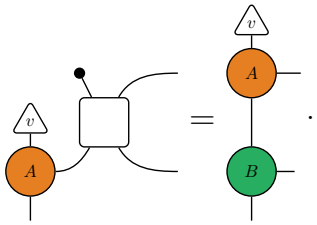

. (4.38)

Finally, we can use Eq. (4.38) to simplify Eq. (4.36): Starting from the leftmost corner, and applying iteratively Eq. (4.38) and the zipper condition Eq. (4.21), we get

$\langle L| =$ 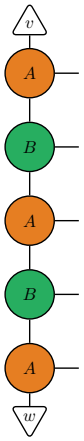

$= \langle v| \underbrace{ABAB\ldots BA}_{2t-1} |w\rangle$. (4.39)

Now, because the only non-zero matrices B_k are diagonal, it is immediate to see that the infinite matrices A_k and B_k can be truncated to be square matrices with $\alpha, \beta = -t, -t+1, \ldots t-1, t$.

Eq. (4.39) holds for arbitrary values of K, yielding an MPS solution whose bond dimension increases linearly with t. However, it can be compressed to an MPS with finite bond dimension when K/π is a rational number

$$K/\pi = n/m\,,$$

with $n, m \in \mathbb{Z}$. In this case, because of the periodicity of the trigonometric and exponential functions in the tensors A and B, it is easy to show that the corresponding matrices can be truncated to the first m lines and columns. After reshaping, we obtain

$$[A_{00}]_{\alpha,\beta} = \delta_{\alpha,\beta} \cos[2K(\alpha-1)]\,, \tag{4.40a}$$
$$[A_{11}]_{\alpha,\beta} = [A_{00}]_{\alpha,\beta}\,, \tag{4.40b}$$
$$[A_{01}]_{\alpha,\beta} = \delta_{1,\alpha-\beta \bmod m} \cos[2K(\beta-1)]\,, \tag{4.40c}$$
$$[A_{10}]_{\alpha,\beta} = \delta_{1,\beta-\alpha \bmod m} \cos[2K\alpha]\,, \tag{4.40d}$$

and

$$[B_{00}]_{\alpha,\beta} = \delta_{\alpha,\beta} \exp[2Ki(\alpha-1)]\,, \tag{4.41a}$$
$$[B_{11}]_{\alpha,\beta} = \delta_{\alpha,\beta} \exp[-2Ki(\alpha-1)]\,, \tag{4.41b}$$
$$[B_{01}]_{\alpha,\beta} = [B_{10}]_{\alpha,\beta} = 0\,, \tag{4.41c}$$

with $1 \leq \alpha, \beta \leq m$.

Here we have illustrated the derivation for the left IM. A similar computation can be carried out for the right one, starting from the SW-NE light-cone transfer matrix, yielding

$$|R\rangle = \langle v| \underbrace{B^* A^* B^* A^* \dots A^* B^*}_{2t-1} |w\rangle\ . \tag{4.42}$$

This chapter is based on the following preprint

G. Giudice et al., *Trimer states with Z_3 topological order in Rydberg atom arrays*, 2022, arXiv:2205.10387

CHAPTER 5

TRIMER RESONATING-VALENCE-BOND STATES

5.1 Introduction

When quantum fluctuations meet classical frustration, exotic strongly correlated states can arise. Paradigmatic examples are resonating valence bond (RVB) states of hard dimers. They are defined as equal-weight quantum superpositions of all dimer coverings with one dimer touching each vertex of a lattice. These many-body states are the ground states of local Hamiltonians with peculiar properties, such as a ground state degeneracy that depends on the topology of the system and deconfined excitations that come in pairs [229]. When their correlation length is finite, a stable, topologically ordered, quantum phase of matter exists with RVB states as its representatives [230]. This kind of topological order is characterized by a local $\mathbb{Z}_2$ symmetry closely related to the Gauss' law in the gauge theory description of these phases, and it is expected to emerge in dimer models defined on non-bipartite lattices [229].

In this work, we consider RVB states of hard trimers (tRVB). A trimer is an object made up of two nearest-neighbor edges of a lattice that share a common vertex [cf. Fig. 5.1.1(a)]. 'Hard trimers cannot touch each other, such that each vertex of the lattice can be covered by at most one trimer, yielding what we refer to as the trimer constraint. Maximally-packed trimer configurations are obtained by demanding that exactly one trimer covers each vertex. These configurations are then promoted to orthogonal quantum states, and the tRVB state is their equal-weight quantum superposition. On certain lattices, tRVB states are known to be gapped and to possess a form of topological order with emergent $\mathbb{Z}_3$ gauge symmetry [231–233], and thus to be good representatives of a quantum phase with $\mathbb{Z}_3$ topological order. However, a general condition on the lattice geometry for which these states are gapped and have topological character is still lacking, and physical realizations of this phase are little known [234]. Here, we identify a necessary condition for having a gapped tRVB state with $\mathbb{Z}_3$ topological order, similar to the condition of non-bipartite lattices for dimer models. Moreover, we provide a trimer model where signatures of the above-mentioned topological phase are identified. This model is physically relevant for experimental platforms based on Rydberg atom arrays,

as we demonstrate by proposing and analyzing a viable implementation of the trimer constraint in this setup.

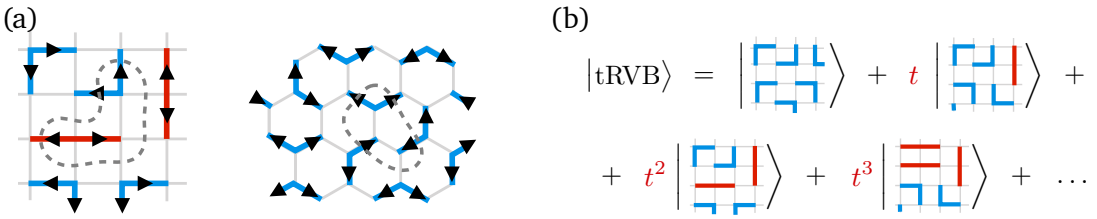

Figure 5.1.1: (a) Maximal trimer configuration with arrows pointing from the center to the two external vertices of each trimer, on the square and honeycomb lattice. The net flux for each vertex is $2 \bmod 3$. The region enclosed by the dashed line has $N_s = 3$ vertices and a net flux $3 = 2N_s \bmod 3$. (b) One-parameter family of tRVB states on the square lattice. The parameter $t = \tan\theta$ weights the presence of straight trimers, such that for $\theta = 0$ ($\pi/2$) the tRVB state is solely made of bent (straight) trimers.

Firstly, we focus on the square lattice, where we demonstrate the emergence of the trimer coverings Hilbert space as a particular limit of a $\mathbb{Z}_3$ lattice gauge theory (LGT). We introduce a tensor network (TN) [16, 17, 235] representation that describes a one-parameter family of tRVB states [Fig. 5.1.1(b)]. Utilizing exact and approximate TN methods, we show that all the tRVB states considered have $\mathbb{Z}_3$ topological order except for a fine-tuned point, where we establish the presence of a $\mathrm{U}(1) \times \mathrm{U}(1)$ local symmetry that leads to long-range correlations. We show that topological properties are stable against dilution of the maximally-packed trimer configurations by studying a tensor-network perturbation that encodes all hard trimer configurations with *at most* one trimer on each vertex. Furthermore, we discuss a general mechanism that explains the enhancement of the local $\mathbb{Z}_3$ conservation law of Fig. 5.1.1(a) to a $\mathrm{U}(1) \times \mathrm{U}(1)$ law, yielding long-range correlations and ultimately spoiling $\mathbb{Z}_3$ topological order. We support our conclusions with further examples of gapless and gapped tRVB states, on the triangular and honeycomb lattices.

Secondly, we consider a diluted trimer model on the square lattice with a single type of trimers, namely the bent blue trimers in Fig. 5.1.1(a). The corresponding tRVB state [Fig. 5.1.1(b) for $t = 0$] will be shown to be a gapped $\mathbb{Z}_3$ topological liquid, thus motivating the choice of this geometry. The model Hamiltonian has a control parameter that tunes the density of trimers. We compute the ground state wavefunction via exact diagonalization on periodic clusters and show that a $\mathbb{Z}_3$ topologically ordered phase arises at finite density. We show that the blockade effect induced by van der Waals interactions in Rydberg atom arrays can be used to engineer the (bent) trimer constraint on the square lattice, by mapping the four possible trimer orientations on a square into four different excited Rydberg atoms. The effective Rydberg model is equivalent to the diluted trimer model upon neglecting some trimer configurations [cf. Fig. 5.4.3(a)]. We prove numerically that removing these configurations from the superposition does not spoil the $\mathbb{Z}_3$ topological nature of the fully-packed tRVB state. We find that, despite signatures of a topological phase being elusive in the ground state of the Rydberg Hamiltonian, a semi-adiabatic dynamical preparation bolsters the topological character of the prepared state.

The chapter is structured as follows. In Sec. 5.2 we introduce a one-parameter family of tRVB states on the square lattice, its TN representation, and a one-parameter perturbation that lower the density of trimers, preserving the TN form. We study the state phase diagram of this two-parameters family and demonstrate the presence of a stable $\mathbb{Z}_3$ topologically ordered phase. In Sec. 5.3 we relate gapped tRVB states to the $\mathbb{Z}_3$ toric code, from which we can define string operators and non-local excitations. We discuss the condition for which a $\mathrm{U}(1) \times \mathrm{U}(1)$ gauge theory emerges in trimer models, and verify it by considering tRVB states on various lattice geometries. In Sec. 5.4 we introduce the model of diluted bent trimers on the square lattice, analyze its ground state properties on finite periodic systems, and show that a narrow topological phase emerges. We outline the implementation of this model in Rydberg atom arrays, point out the differences between the trimer and Rydberg models and discuss the consequences. Finally, we analyze dynamical preparation protocols to realize $\mathbb{Z}_3$ topologically ordered states in experiments.

5.2 tRVB states on the square lattice

Trimers on the square lattice can either be bent or straight [cf. blue and red trimers in Fig. 5.1.1(a)]. Therefore, we can define a one parameter family of tRVB states on this lattice by weighting each covering c with coefficients that depend on the number of bent and straight trimers ($N_\perp(c)$ and $N_\parallel(c)$ respectively) in the covering. In particular, we introduce the parameter $\theta \in [0, \pi/2]$ such that the coefficient of a maximally-packed configuration c is

$$\mathcal{W}(c) = (\cos\theta)^{N_\perp(c)} (\sin\theta)^{N_\parallel(c)}. \tag{5.1}$$

The tRVB state then reads

$$|\mathrm{tRVB}(\theta)\rangle = \frac{1}{\mathcal{N}(\theta)} \sum_{\{c\}} \mathcal{W}(c)\ |c\rangle\,, \tag{5.2}$$

where $\mathcal{N}(\theta) = \sqrt{\sum_{\{c\}} [\mathcal{W}(c)]^2}$ is a normalization factor. The angle θ changes the relative weight of bent versus straight trimers [see Fig. 5.1.1(a)]: in the limit $\theta = 0$ ($\theta = \pi/2$) only bent (straight) trimers contribute.

In this section, we analyze the topological properties of this state with tensor network methods. After studying the one-parameter family in Eq. (5.2), we add another parameter by considering a diluted TN deformation obtained by destroying trimers with a certain probability. We map out the state phase diagram and demonstrate the stability of the topological phase against dilution.

The tensor network representation of the tRVB model

We turn our attention to the classical statistical-mechanics model whose partition function is the sum of the squared weights in Eq. (5.1) of all maximally-packed trimer configurations on the square lattice. This partition function can be interpreted as the norm of the quantum state in Eq. (5.2). Its tensor-network representation was previously introduced

in Ref. [231]: the partition function Z can be written as the tiling of rank-4 tensors

$Z =$ 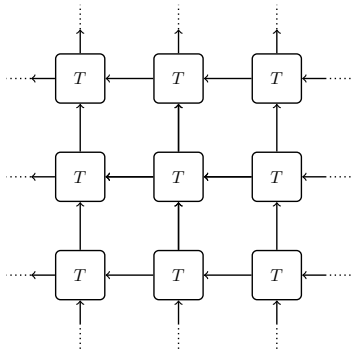 (5.3)

The rank-4 tensor T is constructed in such a way that, once the tensor is contracted with its neighbors, only the valid trimer configurations survive. As will be later discussed in Sec. 5.3, it is beneficial to consider an equivalent representation of this model, where trimer configurations are mapped to possible ways to position arrows on the links such that there is a local constraint —or $\mathbb{Z}_3$ conservation law— around each edge. As shown in Fig. 5.1.1(a), a given trimer configuration has a one-to-one mapping to a single arrow configuration obtained by assigning arrows to the links covered by the trimers, in such a way that each arrow goes from the center of the trimer to the external vertices. In a fully-packed configuration, each vertex has either two outgoing arrows or one ingoing arrow. Because the net outgoing flux for each vertex is 2 (where the flux is measured $\mathrm{mod}\,3$), we obtain that a region of N_s vertices has flux $2N_s \bmod 3$. This $\mathbb{Z}_3$ rule for the flux suggests that the tRVB state can be described as a $\mathbb{Z}_3$ gauge theory and can be a gapped $\mathbb{Z}_3$ quantum spin liquid.

The tensor T is then constructed by labeling each leg with indices $\{0, +1, -1\}$, where 0 means no arrow, and $+1$ (-1) corresponds to an arrow aligned (anti-aligned) with the direction of the leg. The non-zero entries are

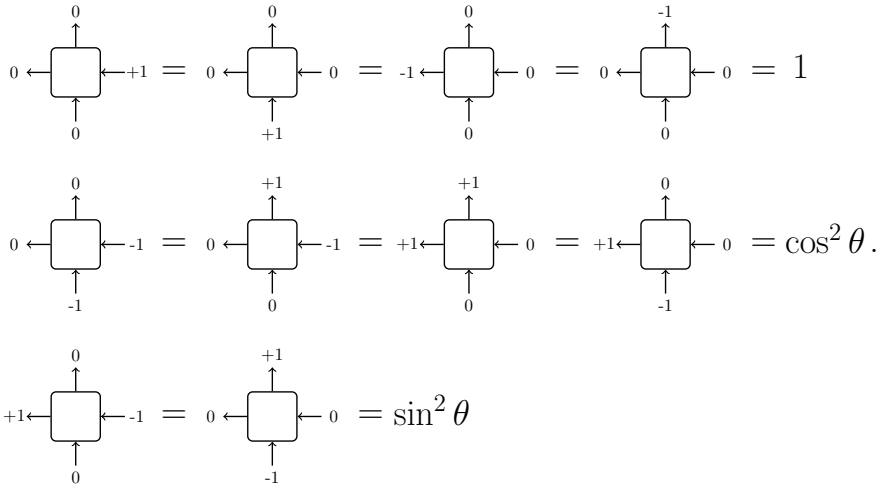

(5.4)

The $\mathbb{Z}_3$ symmetry of the underlying gauge theory is reflected in the tensor. Indeed the symmetry operator σ, whose matrix representation [1] is later defined in Eq. (5.12), acts

[1] The operator is represented in the basis $\{0, +1, -1\}$ defined above.

on the tensor as

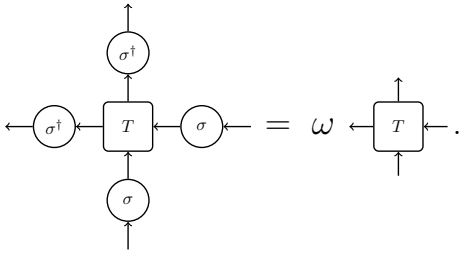

(5.5)

We remark that if one wishes to remove the factor $\omega = e^{i2\pi/3}$ from Eq. (5.5) it is sufficient to block three consecutive tensors and construct a $\mathbb{Z}_3$-invariant tensor. When interpreting the partition function encoded in the tensor Eq. (5.4) as the norm of the tRVB state, each leg of the tensor is interpreted as the product between the bra and ket virtual layers of the quantum state.

The properties of the tRVB wavefunction can be extracted by analyzing the row-wise *transfer operator*

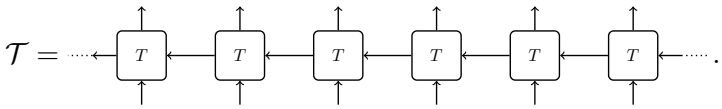

(5.6)

By computing the leading eigenvalues (ordered by magnitude) $\lambda_0, \lambda_1, \dots$ of the transfer operator of length L (with periodic boundary conditions), we obtain the correlation length ξ as

$$\xi = 1/\ln\left|\frac{\lambda_0}{\lambda_1}\right| . \tag{5.7}$$

This quantity bounds all correlation functions in the height direction of the infinitely-tall cylinder of circumference L. The $\mathbb{Z}_3$ virtual symmetry in Eq. (5.5) can be used to label the eigenvalues of the transfer operator as $\lambda_n^{\mathcal{Q}}$, where $\mathcal{Q} = 0, \pm 1$ is the $\mathbb{Z}_3$ charge and $n = 0, 1 \dots$ is eigenvalue index starting from the largest in magnitude. As expected for a topologically ordered state, this symmetry is spontaneously broken, yielding an approximate 3-fold degeneracy for the largest eigenvalues from the three $\mathbb{Z}_3$ symmetry sectors: the gap between the logarithm of these eigenvalues closes exponentially in L [236]. In fact, the spectrum $E = -\log\lambda$ is analogous to the spectrum of a Hamiltonian with spontaneous symmetry breaking. To compute the correlation length at finite L we thus consider the two largest eigenvalues in the $\mathcal{Q} = 0$ sector. The results of numerical diagonalizations on finite cylinders are presented in Fig. 5.2.1(a). These finite-size results are compared to the correlation lengths obtained from the corner-transfer matrix renormalization group (CTMRG) [108, 237–241] exploiting the reflection symmetry along the tensor diagonal [242], as well as from the variational uniform matrix product state algorithm (VUMPS) [97]. From the numerical results, we conclude that the correlation length diverges only in the limit $\theta \to \pi/2$, while it remains finite below that value. As we will discuss in the next section, long-range correlations concur with the emergence of a $\mathrm{U}(1) \times \mathrm{U}(1)$ local symmetry for $\theta = \pi/2$.

The leading eigenvector of the transfer operator on a cylinder represents the diagonal reduced density operator ρ of the infinite half-cylinder, from which we can as well obtain the entanglement entropy $S = -\operatorname{Tr}(\rho \ln \rho)$ of this bipartition. The scaling with the circumference length L of the entanglement entropy obeys

$$S_L \sim \alpha L - \gamma, \tag{5.8}$$

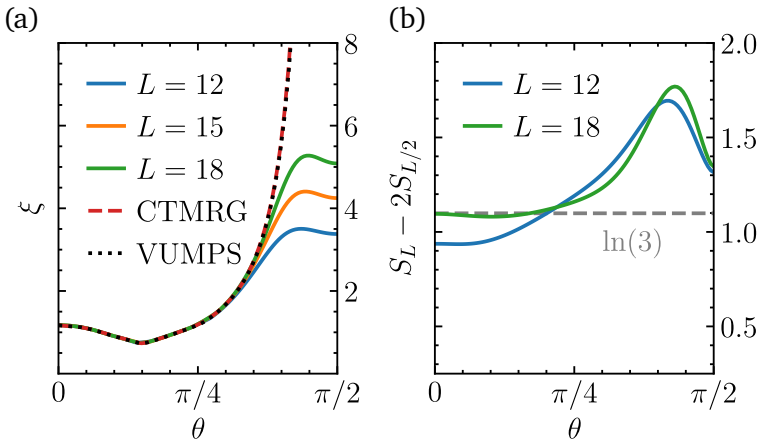

Figure 5.2.1: (a) Correlation length ξ as a function of θ, computed using infinite cylinders of circumference L, as well as infinite-size methods (see main text). (b) Topological entanglement entropy $\gamma \simeq S_L - 2S_{L/2}$ extracted from finite-size cylinders.

where γ is a well-known topological correction [243, 244]. $\gamma \simeq \ln 3$ implies that the state is in a gapped $\mathbb{Z}_3$ topological phase. In Fig. 5.2.1(b) we plot the topological entanglement entropy obtained from the subtraction $\gamma = S_L - 2S_{L/2}$, as a function of θ. While γ appears to approach a finite value compatible with $\ln 3$ for $\theta \neq \pi/2$, a bump occurs in the proximity of this point. In fact, in the presence of continuous local symmetries such as $\mathrm{U}(1) \times \mathrm{U}(1)$ the topological correction is expected to scale logarithmically with L [245].

Stability under dilution of the tRVB state

We now study a deformation of the tRVB state obtained by diluting fully-packed trimer coverings. This deformation will be relevant for Sec. 5.4, where we will discuss how to implement trimer models in Rydberg atom arrays. In these setups, the total occupation can fluctuate, so it is important to consider imperfect trimer coverings.

Similarly to recent work on dimer models [246], we consider the following variational ansatz, which depends on two real parameters $0 \leq \theta \leq \pi/2$ and $z \in \mathbb{R}$

$$|\Phi(\theta, z)\rangle \propto \bigotimes_{i,j} \left(\mathbb{1} + z^2 \Sigma_{ij}^- \right) |\mathrm{tRVB}(\theta)\rangle \ , \tag{5.9}$$

where Σ_{ij}^- is the operator that removes a trimer on the edges i and j, and z^2 corresponds to the weight of a removed trimer. In essence, we add to the fully-packed trimer configurations other trimer configurations that can be obtained from the former by removing trimers without moving the remaining ones. Each removed trimer is weighted by z^2. In the limit $z \to \infty$, the state is simply the vacuum, while at $z \to 0$ we recover the tRVB state, which we showed to be in a topological phase. Similarly to $|\mathrm{tRVB}\rangle$, the state $|\Phi\rangle$ has a simple projected entangled-pair state (PEPS) [17] representation of bond

dimension 4

$|\Phi\rangle =$ 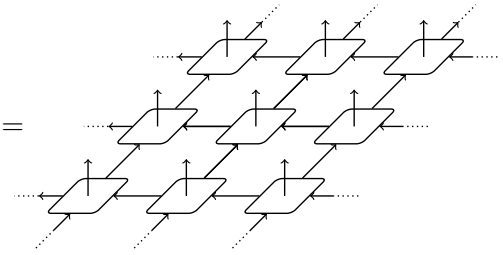 . (5.10)

Its construction is relegated to App. 5.A.

In Fig. 5.2.2, we study the link density n [2] and the correlation length of the state as we vary θ and z using CTMRG. Remarkably, the topological phase survives up to values of order one of the dilution strength z, and is fairly insensitive to the mixing angle θ. The transition between the topological and trivial phases appears to be continuous, as witnessed by a diverging correlation length at the critical point [Fig. 5.2.2(b)]. We do not address the characterization of the universality class of this phase transition as the critical exponents we could extract from the available data exhibit strong dependence on the CTMRG environment bond dimension D, even for the largest D we employed. We note that topological and trivial phases are distinguished by two different degeneracies of the PEPS cylinder transfer matrix. The spectrum of the transfer matrix is 3-fold degenerate in the former and 9-fold degenerate in the latter. The 9-fold degeneracy reflects the full breaking of the $\mathbb{Z}_3 \times \mathbb{Z}_3$ virtual symmetry of the PEPS double tensor, which implies the condensation of magnetic and the confinement of electric excitations [see Sec. 5.3] in the gauge theory picture [236].

5.3 tRVB states and lattice gauge theories

To understand the emergence of $\mathbb{Z}_3$ topological order in the tRVB state, it is useful to shed light on its connection with a gauge theory. To this end, in Sec. 5.3 we compare the tRVB state to the ground state of a $\mathbb{Z}_3$ toric code.

We argued in Sec. 5.2 that the presence of a $\mathbb{Z}_3$ local conservation law of the flux suggests an emergent description as a $\mathbb{Z}_3$ gauge theory, and hence the tRVB state is a good candidate for being a gapped $\mathbb{Z}_3$ quantum spin liquid. However, as we show below, it may happen that for some trimer models the $\mathbb{Z}_3$ local symmetry is enhanced to a $\mathrm{U}(1)\times\mathrm{U}(1)$ symmetry, in which case the state is gapless [3]. A similar scenario occurs for RVB states of dimer models, that are known to host gapped $\mathbb{Z}_2$ spin liquids only on non-bipartite lattices; on bipartite lattices, they are described by a $\mathrm{U}(1)$ gauge theory, that does not support a stable topologically ordered phase. In Sec. 5.3 we will formulate a similar criterion for trimer models.

[2] The link density n counts the ratio of links occupied by a trimer over the total number of links. On the square lattice the link density of a fully-packed configuration is $1/3$.

[3] As we discuss below, there are exceptions in which, despite the $\mathrm{U}(1) \times \mathrm{U}(1)$ local, the tRVB state is a gapped symmetry broken state.

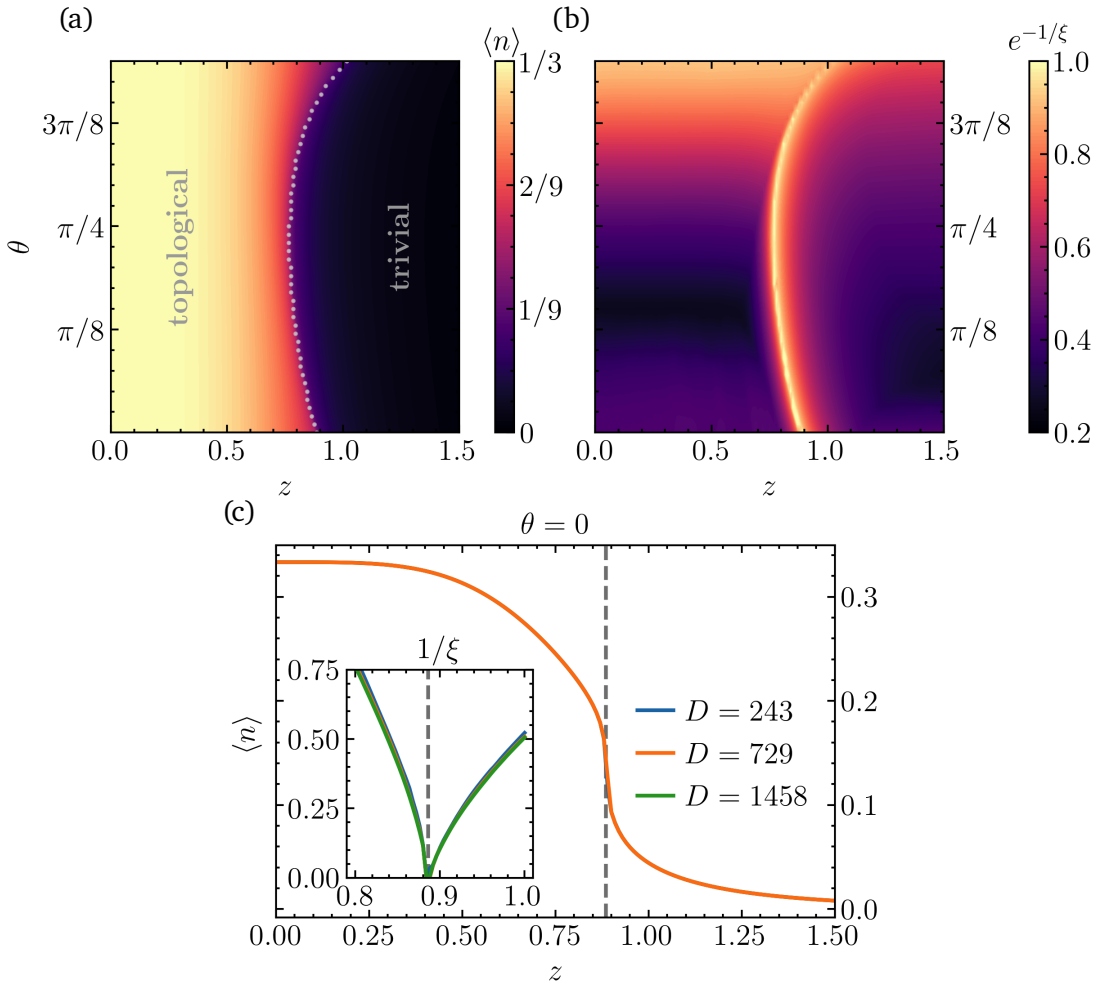

Figure 5.2.2: (a) Link density of the diluted tRVB state $|\Phi(\theta, z)\rangle$, obtained from CTMRG with an environment bond dimension $D = 729$. The grey dots indicate where its numerical derivative with respect to z has an extremum. (b) Correlation length ξ obtained from the transfer matrix of the diluted tRVB state computed with CTMRG. Note that ξ diverges at the phase boundary and at $\theta \to \pi/2$. (c) Details for $\theta = 0$: the density displays a non-analyticity at $z_c = 0.88(6)$ (dashed line), which corresponds to a divergence of the correlation length (inset).

The $\mathbb{Z}_3$ toric code

A state that is very similar to the tRVB state and has $\mathbb{Z}_3$ topological order is the ground state of the $\mathbb{Z}_3$ generalization of Kitaev's toric code [247]. We now review this model and show the similarities and differences between its ground state and the tRVB state.

To define the $\mathbb{Z}_3$ toric code, we introduce clock variables on the links of our lattice; on each link we define the operators σ and τ, that satisfy the following properties:

$$\sigma\tau = \omega\tau\sigma, \qquad \sigma^3 = \mathbb{1}, \qquad \tau^3 = \mathbb{1}, \tag{5.11}$$

where $\omega = e^{2i\pi/3}$. These variables are the $\mathbb{Z}_3$ generalizations of the Pauli matrices σ^z

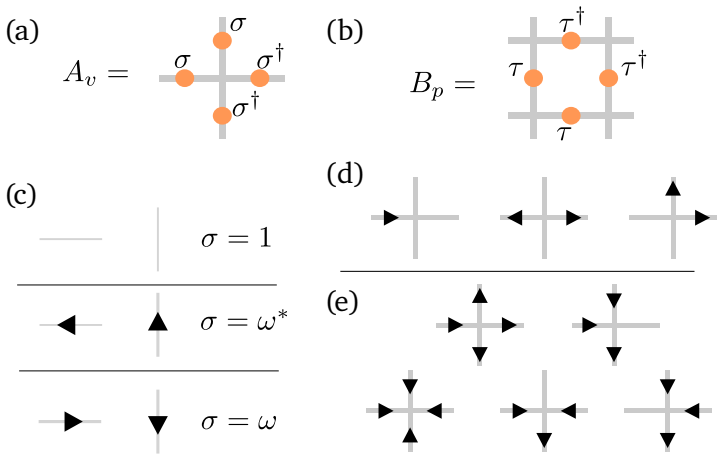

Figure 5.3.1: Definitions of operators (a) A_v and (b) B_p. (c) Mapping from a trimer configuration to a state in the σ basis. (d) Configurations for a vertex in the trimer model. The 10 total configurations are obtained from these under rotations. (e) Configurations that satisfy Gauss' law but do not correspond to trimer configurations. The full set of unallowed configurations (17 in total) is obtained from these under rotations.

and σ^x, and their most common matrix representation is

$$\sigma = \begin{pmatrix} 1 & 0 & 0 \\ 0 & \omega & 0 \\ 0 & 0 & \omega^* \end{pmatrix}, \qquad \tau = \begin{pmatrix} 0 & 0 & 1 \\ 1 & 0 & 0 \\ 0 & 1 & 0 \end{pmatrix}. \tag{5.12}$$

We now define the star and plaquette operators as in Figs. 5.3.1(a) and 5.3.1(b). Similarly to the case of the $\mathbb{Z}_2$ toric code, these operators all commute: $[A_v, B_p] = 0$ for every vertex v and plaquette p. We now define the state $|\psi_{\text{TC}}\rangle$ as the equal-weight superposition of all the states in the σ basis that satisfy the Gauss' law $A_v = \omega$ for all vertices. Note that this choice differs from the typical case with $A_v = 1$ and corresponds to the presence of a background charge on each vertex of the lattice. Nevertheless, the physical properties that we are interested in are not altered by this background charge, as a unitary transformation can be defined to eliminate it. The state defined here has the property that $B_p |\psi_{\text{TC}}\rangle = |\psi_{\text{TC}}\rangle$ for every plaquette p, and is the ground state of the following Hamiltonian

$$H_{\text{TC}} = -\sum_v (\omega^* A_v + \omega A_v^\dagger) - \sum_p (B_p + B_p^\dagger). \tag{5.13}$$

Because star and plaquette operators commute, it is easy to identify the excitations of the model: we call an excitation with $A_v = \omega^*$ ($A_v = 1$) a charge (anticharge), while an excitation with $B_p = \omega$ ($B_p = \omega^*$) is a vison (antivison). Both "electric" (charge/anticharge) and "magnetic" (vison/antivison) excitations are gapped.

We now elucidate the connection between the tRVB state and $|\psi_{\text{TC}}\rangle$. We can map each configuration of fully-packed trimers to a configuration in the σ basis as shown in Fig. 5.3.1(c). It is easily shown that this configuration satisfies Gauss' law. However, not all the configurations of the $\mathbb{Z}_3$ toric code that satisfy Gauss' law correspond to a trimer configuration: as shown in Fig. 5.3.1(d), only 10 of the 27 configurations of a vertex correspond to allowed vertex configurations of the trimer model. Despite this difference,

the tRVB state may still have $\mathbb{Z}_3$ topological order like $|\psi_{\mathrm{TC}}\rangle$ if the missing configurations are recovered under renormalization: for $0 \leq \theta < \pi/2$ the renormalization-group flow from the state $|\mathrm{tRVB}(\theta)\rangle$ ultimately leads to the toric code ground state, which is a fixed point under blocking, with correlation length $\xi = 0$. Another approach to establish that the tRVB state and the toric code ground state describe the same phase consists in showing that no phase transitions occur when interpolating between the two states. This operation can as well be interpreted as a smooth interpolation between the two parent Hamiltonians, since $\mathbb{Z}_3$ injectivity is preserved [236, 248]. We interpolate between the states $|\psi_{\mathrm{TC}}\rangle$ and $|\mathrm{tRVB}\rangle$ by progressively decreasing the weight of the forbidden configurations in Fig. 5.3.1(e). In Fig. 5.3.2(c) we plot the correlation length ξ obtained from CTMRG during the interpolation. The gradual increase of ξ for any $0 \leq \theta < \pi/2$ indicates the absence of phase transitions. We note that what we observed here differs from what happens in the dimer model of the kagome lattice, where the RVB state *is* a fixed point of $\mathbb{Z}_2$ topological order, and can be directly mapped into the toric code ground state [249].

Finally, the connection with the $\mathbb{Z}_3$ toric code allows one to define string operators that are useful for detecting topological order, namely Wilson lines and 't Hooft lines. The latter can be defined as in Fig. 5.3.2(a). Because of Gauss' law, the value of the 't Hooft line around a closed loop is equal to $\omega^{N_v+n_q-n_{\bar{q}}}$, where N_v is the number of vertices, and n_q, $n_{\bar{q}}$ are respectively the numbers of charges and anticharges enclosed by the loop. Similarly, Wilson loops detect the number of visons/antivisons in a region. Moreover, a 't Hooft (Wilson) line creates a vison/antivison (charge/anticharge) pair at the two ends of the line.

We now consider the same string operators on the trimer model. The diagonal operator ('t Hooft line) is still well defined. Closed 't Hooft loops count the number of charges/anticharges in a closed region. Note that, if we consider a diluted tRVB state, we allow only for the presence of monomers on vertices, i.e. anticharges having $A_v = 1$. In this case, a pair of monomers represents a charge. In contrast with the 't Hooft line, the off-diagonal operator (Wilson line) is not well defined on the trimer model, as it can map a valid trimer configuration to one that contains one of the vertices in Fig. 5.3.1(e). However, as shown in Fig. 5.3.2(b), on some states it is possible to define an operator that acts similarly to a Wilson line, and creates a monomer at one end of the line, and a pair of monomers at the other end. The charges and anticharges obtained in this way are deconfined if the state has topological order.

Knowing the operatorial form of Wilson and 't Hooft lines provides (non-local) order parameters [250, 251] that can be used to assert the presence of $\mathbb{Z}_3$ topological order, as exploited in [252] for $\mathbb{Z}_2$ topological spin liquids in Rydberg atom arrays. Although in Sec. 5.4 we will not undertake the calculation of these order parameters because of the limited system sizes, we point out that they might be an effective probe for experimental realizations of trimer models.

Tripartite trimer models and $\mathrm{U}(1) \times \mathrm{U}(1)$ lattice gauge theories

As shown in Fig. 5.2.1, the correlation length of the model diverges for $\theta = \pi/2$, implying that the tRVB state containing only straight trimers is gapless. We now explain this result, by proving that for straight trimers the $\mathbb{Z}_3$ symmetry is enhanced to a $\mathrm{U}(1) \times \mathrm{U}(1)$ symmetry. We define a partition of the square lattice in three sublattices A, B, and C as in Fig. 5.3.3(a). It is easy to check that a straight trimer always covers one and only

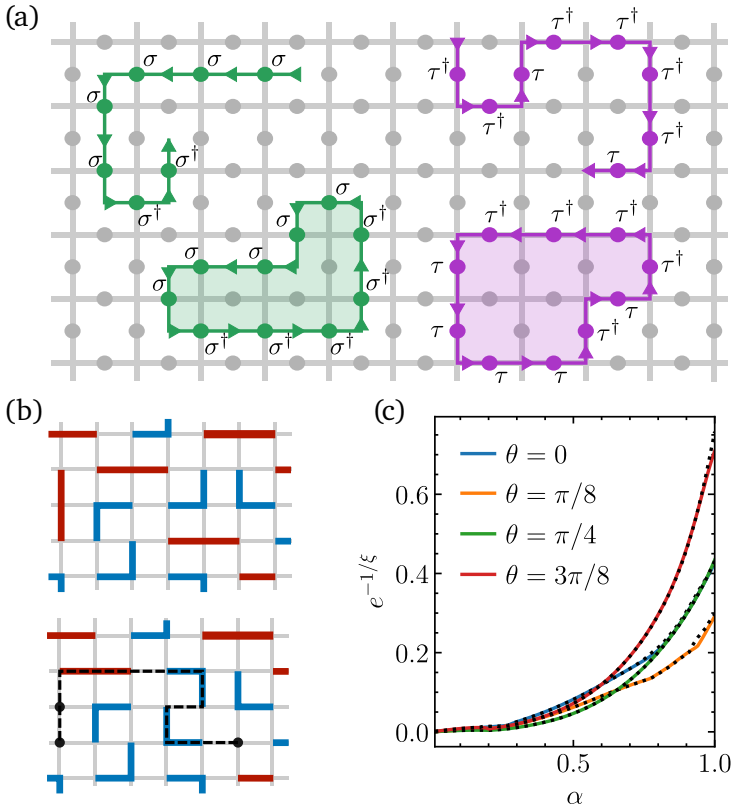

Figure 5.3.2: (a) String operators in the $\mathbb{Z}_3$ toric code: 't Hooft lines and 't Hooft loops (green), Wilson lines and Wilson loops (purple). (b) Creation of a charge-anticharge pair on a trimer configuration with a string operator: a monomer is an anticharge, and a charge consists of a pair of monomers. (c) The correlation length remains finite when interpolating between the $\mathbb{Z}_3$ toric code ($\alpha = 0$) and the tRVB state ($\alpha = 1$) at different mixing angles θ of the $\mathbb{Z}_3$-charged tensor $T = (1-\alpha)T_{\mathrm{TC}} + \alpha T_{\mathrm{tRVB}}(\theta)$. Finite-size results on a cylinder of $L = 18$ (solid lines) agree with the CTMRG results (dotted lines).

one site per type. A similar scenario occurs for dimer models on bipartite lattices: each dimer covers one site of each type, and the symmetry is enhanced from $\mathbb{Z}_2$ to $\mathrm{U}(1)$. Here, we will show that the emergent symmetry for straight trimers is $\mathrm{U}(1) \times \mathrm{U}(1)$. To prove it, we define two electric fields. The first electric field flows from the A to the B site of each trimer [Fig. 5.3.3(b)], and the second electric field flows from the A to the C site [Fig. 5.3.3(c)]. We then obtain two independent conservation laws, one for each electric field: consider a region with N_A, N_B, N_C vertices of the three types. The net flux going out of the region is $N_A - N_B$ for the first electric field and $N_A - N_C$ for the second electric field. Therefore, the tRVB state has a local symmetry $\mathrm{U}(1) \times \mathrm{U}(1)$ and must be gapless, as shown by Polyakov [253].

The argument presented above can be generalized to any trimer model on a two-dimensional lattice. We posit that a trimer model is tripartite if three sublattices can be defined, such that a trimer always covers one site for each sublattice. Note that this definition depends both on the lattice and on the class of trimers considered. If a trimer model is tripartite, the tRVB state has a local $\mathrm{U}(1)\times\mathrm{U}(1)$ symmetry. In the absence of

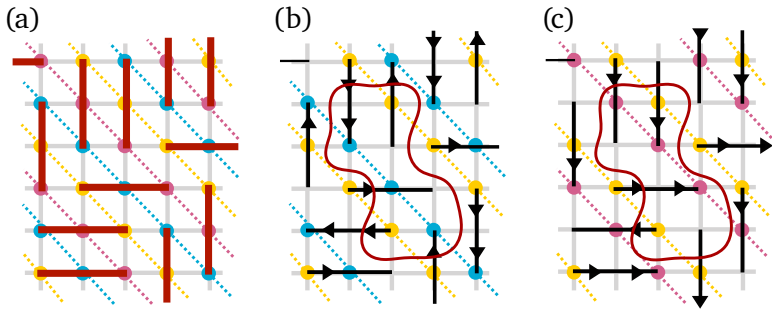

Figure 5.3.3: (a) Partition of the square lattice in the three sublattices A (yellow), B (blue) and C (pink). A straight trimer always covers one site of type A, one of type B and one of type C. (b) First U(1) symmetry: electric field lines go from the A site to the B site for each trimer. The net flux going out of the region enclosed by the red line is $-1 = N_A - N_B$. (c) Second U(1) symmetry: electric field lines go from the A site to the C site for each trimer. The net flux going out of the region enclosed by the red line is $-1 = N_A - N_C$.

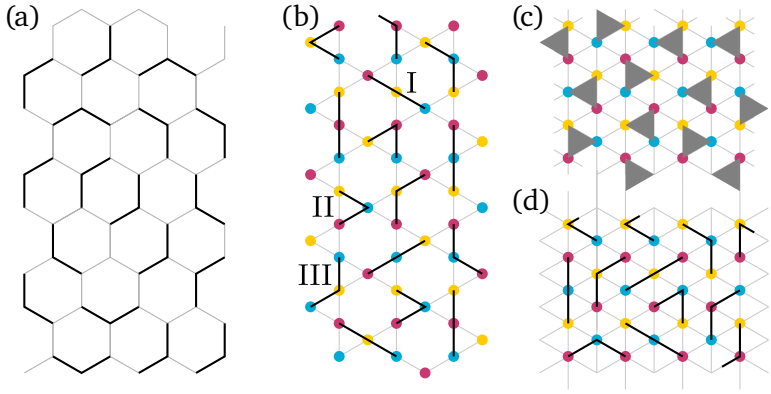

Figure 5.3.4: (a) Trimer model on the honeycomb: the lattice is not tripartite. (b)–(c) Two possible tripartitions of the trimer model on the kagome lattice. We define trimers of type I (straight), II (bent, with angle $60°$), and III (with angle $120°$). (b) The lattice is tripartite if no type III trimers are included. (c) Similarly, the lattice is tripartite if no type I trimers are included. (d) Trimer model on the triangular lattice: the lattice is tripartite for triangular trimers. (e) The triangular lattice is tripartite for trimers of type I and II, not tripartite for trimers of type III.

lattice symmetry breaking, the emergence of this continuous local symmetry leads to a gapless spin liquid state akin to RVB states in dimer models on bipartite lattices. We can thus conclude that a necessary condition for having a gapped $\mathbb{Z}_3$ spin liquid from a tRVB state is that the trimer model is *not* tripartite. We remark that this condition is not sufficient, as demonstrated by the examples that we provide below.

Let us first consider the tRVB state on the honeycomb lattice [Fig. 5.3.4(a)]. This trimer model is not tripartite, so this state on the honeycomb lattice can be a gapped state with $\mathbb{Z}_3$ topological order. The numerics in Fig. 5.3.5 confirm that this is the case. In Fig. 5.3.5(b) we show that the correlation length of the tRVB state on a finite cylinder converges to a finite value as the circumference increases. In Fig. 5.3.5(b) we show

that the entanglement entropy of a half-infinite cylinder exhibits a $-\ln 3$ correction to its area law scaling. Finally, the blue hexagons in Fig. 5.3.5(c) demonstrate that the logarithmic gap between the leading eigenvalues of the neutral and charged sectors closes exponentially, pointing to the spontaneous breaking of $\mathbb{Z}_3$ virtual symmetry.

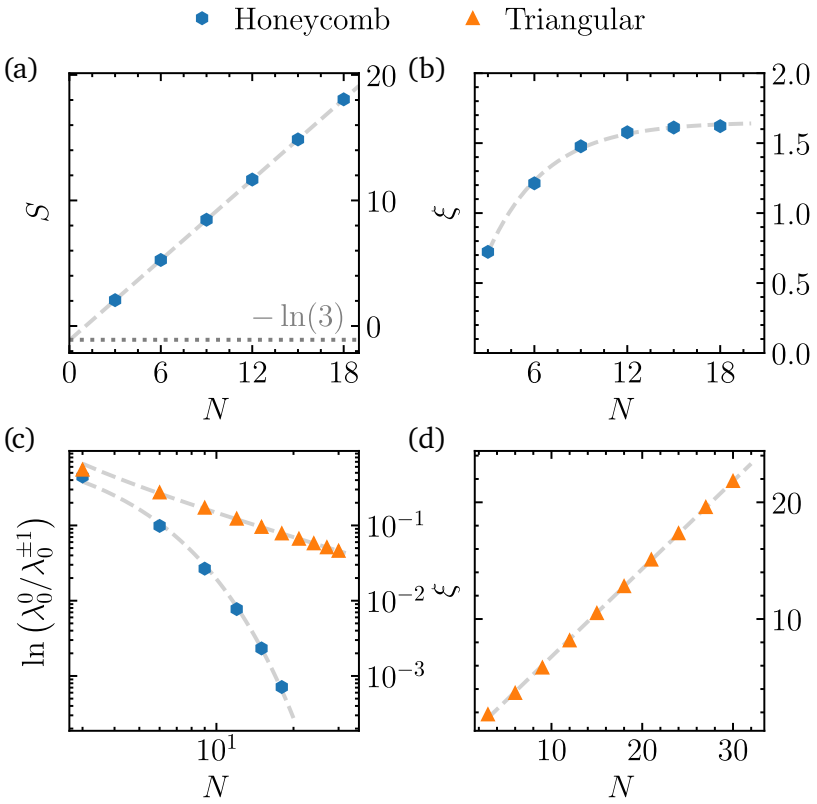

Figure 5.3.5: (a) Scaling of the entanglement entropy of the tRVB state on the honeycomb lattice as a function of the number of tensors N around the cylinder. We extract a topological correction $\gamma \simeq \ln 3$. (b) Correlation length of the tRVB state on the honeycomb lattice. (c) Logarithmic gap between the leading eigenvalues of the $\mathcal{Q} = 0$ and $\mathcal{Q} = \pm 1$ sectors for the tRVB state on the honeycomb (blue hexagons) and triangular (orange triangles). On the triangular lattice, only triangular trimers are considered. Transfer matrix eigenvalues are labeled as $\lambda_n^{\mathcal{Q}}$ where $\mathcal{Q}$ is the $\mathbb{Z}_3$ symmetry sector and $n = 0, 1 \ldots$ is the position in the spectrum starting from the largest in magnitude. (d) Correlation length of the tRVB on the triangular lattice. Similar to dimer models on bipartite lattices, it grows linearly with the number of tensors N along the circumference. The TN description of these models can be found in App. 5.A.

Let us now turn our attention to the kagome lattice. In this case, various types of trimers can be defined. If we consider the tripartition of the lattice shown in Fig. 5.3.4(b), we note that some types of trimers (I and II) cover sites of different types, while trimers of type III do not. Therefore, we deduce that type III trimers are needed to have a $\mathbb{Z}_3$ spin liquid phase. Similarly, from the tripartition in Fig. 5.3.4(c), we find that type II trimers are also needed. This result is in agreement with Ref. [233], where it was shown that

a gapped tRVB state with topological order is found only when all types of trimers are included. This lattice provides a counterexample that shows how our "non-tripartibility" condition is not sufficient for gapped $\mathbb{Z}_3$ topological order. In fact, in Ref. [233] it was proven that the tRVB state with trimers of type I and III possesses a $\mathrm{U}(1)$ local symmetry that spoils $\mathbb{Z}_3$ topological order although the trimer model cannot be tripartite. Trimer models on this geometry also provide an example of $\mathrm{U}(1) \times \mathrm{U}(1)$ symmetric tRVB state that is not gapless but has symmetry breaking: the tRVB state with trimers of type II only is tripartite, but *all* trimer coverings break the two-fold rotation of the lattice that maps upper into lower triangles.

Finally, let us consider the triangular lattice. As can be inferred from Fig. 5.3.4(d), the tRVB state of triangular trimers [4] (grey triangles in the figure) is $\mathrm{U}(1) \times \mathrm{U}(1)$ symmetric because the model is tripartite: this finding agrees with Ref. [254], where a $\mathrm{U}(1)\times\mathrm{U}(1)$ conservation law (for "left-" and "right-movers") was found in the classical configurations. From numerical diagonalization of the transfer matrix on finite-size cylinders, we deduce that this tRVB state is indeed gapless, as demonstrated in Fig. 5.3.5(d), where we show that for the sizes accessible with our numerics, the correlation length scales linearly with the circumference of the cylinder. We refer to App. 5.A for the explicit TN representation of this tRVB state. Using the same definitions of trimers as for the kagome lattice, we have that trimers of type I (straight) on the triangular lattice are also tripartite and expected to spoil gapped topological order, while trimers of type III do not respect the tripartition [Fig. 5.3.4(e)]. This implies that tRVB states on this lattice can have topological order only if these trimers are included. We leave a complete analysis of this family of tRVB states for future work.

5.4 Diluted trimer models and Rydberg atoms

In the previous sections we have shown that RVB states of trimers can be gapped and have topological character. When these conditions are met they are good candidates for representing a stable phase with $\mathbb{Z}_3$ topological order. It is thus natural to ask if simple Hamiltonians exist that have tRVB-like phases at zero temperature. As trimer states are TN states with finite bond dimension, they are exact ground states of local Hamiltonians with finite range. However, it is known that such Hamiltonians can be rather complex and include fairly unphysical operators [248, 249, 255]. In particular, parent Hamiltonians of tRVB states on certain lattices are discussed in Refs. [231, 233]. Here, instead, we introduce a simple trimer model on the square lattice and study its ground state phase diagram via exact methods, providing evidence of a tRVB-like phase with $\mathbb{Z}_3$ topological order. Moreover, we show that a similar model can be implemented in Rydberg atom arrays and that hallmarks of $\mathbb{Z}_3$ topological order can be observed employing semi-adiabatic dynamical preparation schemes.

An effective trimer models on the square lattice

We consider the Hilbert space spanned by all diluted trimer configurations of bent trimers on the square lattice, i.e. with at most one trimer per vertex of the square lattice, and

[4] The triangular trimers considered here do not consist of two edges sharing a common vertex, but rather of triangular plaquettes with hard constraints. Nevertheless, the discussion on the general conditions for $\mathbb{Z}_3$ or $\mathrm{U}(1)\times\mathrm{U}(1)$ gauge symmetry is applicable here in the same way.

take the following model Hamiltonian

$$H = \frac{\Omega}{2} \sum_{\square} |\square\rangle\langle\square| + \text{h.c.} - \Delta\, |\square\rangle\langle\square| + R_{\frac{\pi}{2}}. \tag{5.14}$$

$R_{\frac{\pi}{2}}$ denotes the terms that can be obtained by 90-degree rotations from those given in Eq. (5.14). The first term coherently creates and destroys bent trimers (subject to the hard trimer constraint), whereas the second, diagonal term acts like a chemical potential for trimers. The ratio Δ/Ω controls the density of trimers in the ground state. For large and negative Δ/Ω the ground state is trivial and adiabatically connected to the vacuum. For $\Delta/\Omega = +\infty$ the classical ground space is exponentially degenerate and consists of all maximally-packed trimer coverings, corresponding to a link density $\langle n \rangle = 1/3$. By treating pertubatively the off-diagonal diagonal term, it is easy to see that the first non trivial process in this subspace occurs at fourth order and produces resonances between pairs of trimer coverings differing only on two nearby squares. Therefore, at large Δ/Ω a valence bond solid (VBS) ground state is expected to emerge, with a maximal density of resonating "plaquettes", i.e., resonating pairs of nearby squares [5]. At finite Δ/Ω, quantum fluctuations act in two ways: they create defects in the trimer coverings by lowering the density and build coherent superpositions of high density components. As we showed in Sec. 5.2, topological order can survive at finite dilution, implying that a diluted tRVB state might also arise from this setup.

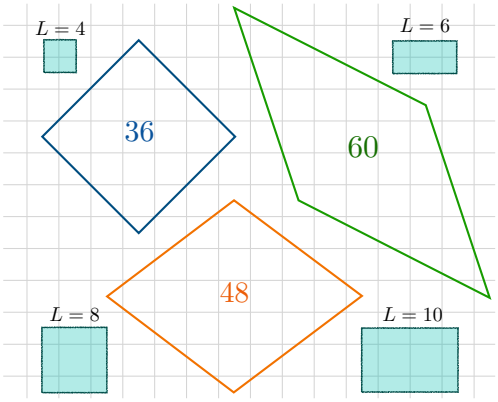

Figure 5.4.1: Periodic clusters employed for the exact diagonalization of the Hamiltonian in Eq. (5.14). 36, 48, and 60 stand for the number of edges inside the cluster. The turquoise regions are the subsystems used to compute the entanglement entropy. We measure their perimeter L in units of an edge of the square lattice.

To understand the character of the ground state at intermediate Δ/Ω we performed exact diagonalization calculations on periodic clusters of up to 60 edges of the square lattice [Fig. 5.4.1]. In Fig. 5.4.2(a) we plot the overlap between the ground state and the pure tRVB state (solid line), and the ground state fidelity with the diluted tRVB state Eq. (5.9) for $\theta = 0$ optimized over z (dashed line). The optimal values of z as a function of Δ/Ω are shown in Fig. 5.4.2(c). Remarkably the overlap displays a maximum at $\Delta/\Omega \simeq 1$,

[5] We note that the number of plaquette coverings is not finite when the system is infinite, and a quantum order by disorder scenario is likely to occur.

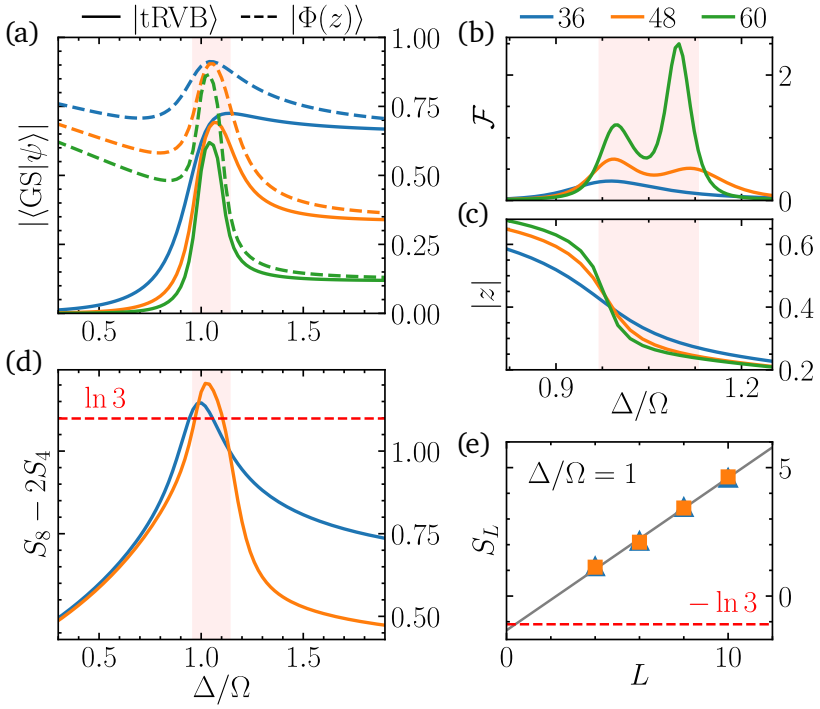

Figure 5.4.2: (a) Overlap between the ground state of the Hamiltonian Eq. (5.14) and the tRVB state (solid line), and the diluted tRVB state Eq. (5.9) optimized over z (dashed line). The shaded red region sets approximate boundaries for the topologically ordered phase, where the fidelity with the tRVB state is maximized. (b) Ground state fidelity susceptibility per link $\mathcal{F} = (1-|\langle \mathrm{GS}(\lambda)|\mathrm{GS}(\lambda+\mathrm{d}\lambda)\rangle|)/N\mathrm{d}\lambda^2$, with $\lambda = \Omega/\Delta$. Two peaks appear for the larger clusters, pointing at the presence of an intermediate phase for $0.95 \lesssim \Delta/\Omega \lesssim 1.15$. (c) Optimal value of z that maximizes the overlap between the ground state and the diluted tRVB state Eq. (5.9). $|z| \lesssim 0.4$ in the intermediate phase, a value that lies deep in the topological phase in the state phase diagram plotted in Fig. 5.2.2. (d) Ground state topological entanglement entropy computed by subtracting the entropies of the square-shaped regions in Fig. 5.4.1 with $L = 4$ and $L = 8$. (e) Scaling of the entanglement entropy of the ground state for $L = 4, 6, 8, 10$ and $\Omega/\Delta = 1$.

pointing to the presence of an intermediate tRVB-like phase. The maximum fidelity is greatly improved when optimized with the diluted tRVB state. We note that the optimal value of z near the maximum is perfectly consistent with the topologically ordered phase in the state phase diagram in Fig. 5.2.2. The occurrence of an intermediate phase is also witnessed by the presence of two peaks in the ground state fidelity susceptibility per link $\mathcal{F} = (1 - |\langle \mathrm{GS}(\lambda)|\mathrm{GS}(\lambda+\mathrm{d}\lambda)\rangle|)/N\mathrm{d}\lambda^2$, where $\lambda = \Omega/\Delta$ [6] for the 48- and 60-links clusters, as depicted in the Fig. 5.4.2(b). To confirm the nature of the intermediate phase in an unbiased way, in Fig. 5.4.2(d) we show the topological entanglement entropy extracted from $\gamma \simeq S_{2L} - 2S_L$ as functions of Δ/Ω. Here L is the length of the contour of the subsystem, in units of one edge of the square lattice, and the subsystems employed for the computation are depicted in Fig. 5.4.1. The value of γ obtained near the tRVB

[6] The parameter λ is chosen to make more distinguishable the two peaks in $\mathcal{F}$.

fidelity maximum is remarkably close to the value $\ln 3$, hinting at the emergence of $\mathbb{Z}_3$ topological order.

The trimer constraint with Rydberg atoms

We now turn to a discussion of potential realizations of trimer models and tRVB states with experiments based on Rydberg atom arrays. In these systems, neutral atoms are individually trapped and arranged in a desired lattice configuration using optical tweezers [36, 37]. Spin models can then be realized by manipulating the internal degrees of freedom of each atom with an external laser field [256–261]. Specifically, we consider a situation where a laser induces a coherent coupling from the atomic ground state $|g\rangle$ to a highly excited Rydberg state $|r\rangle$. The frequency mismatch between the laser frequency and the transition frequency between those two states, i.e. the laser detuning, is denoted by Δ. The coupling strength for this transition, i.e. the Rabi frequency, is denoted by Ω, and is proportional to the laser amplitude. Importantly, two atoms that are both in the Rydberg state interact via a Van der Waals process, whose strength decays with the sixth power of the atomic separation. As a result, the Hamiltonian governing the dynamics of this system is given by [262]

$$H_{\mathrm{Ryd}} = \frac{\Omega}{2}\sum_i \sigma_i^x - \Delta\sum_i n_i + C\sum_{i>j}\frac{n_i n_j}{|\vec{x}_i - \vec{x}_j|^6} \quad , \tag{5.15}$$

where, $\vec{x}_i$ is the position of atom i, and we defined $\sigma_i^x = |g\rangle_i\langle r| + |r\rangle_i\langle g|$ and $n_i = |r\rangle_i\langle r|$. The parameter C depends on the Rydberg state. The interplay between the laser parameters and the geometry of the atom arrangement gives rise to a variety of phenomena [263–268]. Most of them are based on the Rydberg blockade effect, that prohibits the simultaneous excitation of two atoms located at a distance $r < R_b = (V/\Omega)^{1/6}$. Below we show that this effect can be used to implement trimer constraints in Rydberg atom arrays. For example, it is easy to prove that the hard trimer constraint for triangular trimers on the triangular lattice in Fig. 5.3.4(d) is equivalent to a Rydberg blockade constraint on a honeycomb lattice: the atoms sit on the centers of the original triangular lattice and a Rydberg excitation represents a triangular plaquette; the blockade radius R_b is chosen such that two atoms cannot be simultaneously excited if and only if they belong to the same hexagon. We now show that the Rydberg blockade effect also allows one to realize a bent trimer model on the square lattice very similar to the one outlined above. A sketch of the implementation is depicted in Fig. 5.4.3. Rydberg atoms are placed on the corners of a square lattice such that an excited atom is mapped to a bent trimer. The basic idea is to exploit the blockade radius to mimic the hard trimer constraint. However, while the latter is anisotropic, the blockade effect is not, as long as the Rydberg state is rotational invariant. Nevertheless, we can avoid the use of anisotropic Rydberg states by dividing the atoms into two groups, according to the sublattice of the square to which they are closer. The two groups are then arranged onto two planes at a distance h. Consequently, atoms between different planes will be blockaded if their planar distance is less than $\sqrt{R_b^2 - h^2}$, where R_b is the blockade radius. By properly choosing h and the atoms positions inside the plaquettes of the square lattice, it is possible to realize a trimer constraint, as demonstrated by Fig. 5.4.3(b). This trimer constraint is such that some trimer configurations are locally prohibited. The latter are

trimer coverings that include two trimers with the same orientation that are “wedged” diagonally as in Fig. 5.4.3(b).

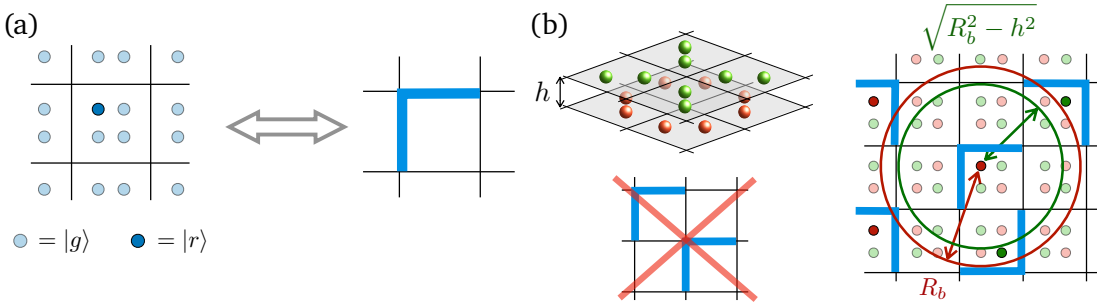

Figure 5.4.3: (a) Mapping between Rydberg atoms and bent trimers on the square lattice. Atoms are placed at each corner of the square lattice such that an excited atom is mapped to a bent trimer on that corner. (b) Atoms are split into two groups (green and red) depending on the sublattice of the square lattice bipartition to which the corresponding corner belongs. The groups are arranged onto two planes at distance h such that the 2D blockade radius between atoms of different colors is $\sqrt{R_b^2 - h^2}$, where R_b is the 3D blockade radius. Tuning h and the distance of the atoms from the vertexes allows realizing a constraint equivalent to the trimer constraint where the “wedged" trimer configurations on the bottom left are blockaded (and its 90-degree rotations).

Before addressing the Rydberg model, we study the effect of removing these coverings from the fully-packed tRVB state. In Figs. 5.4.4(c) and 5.4.4(d) we plot the lowest logarithmic gaps in the spectrum of the cylinder transfer matrix of the corresponding TN state as functions of the cylinder circumference L. The TN representation is outlined in App. 5.A. Despite a level crossing occuring at finite L, the gap between the neutral and charged sectors eventually closes exponentially (green circles), whereas the neutral gap (blue circles) appears to be increasing for the available Ls. From infinite-size calculations we can infer that this gap converges to $\simeq 0.6$, yielding a correlation length $\xi \simeq 1.7$. We note that this value is larger than the correlation length of the unrestricted trimer state $\xi \simeq 1.1$ [cf. Fig. 5.2.1(a)]. This fact is expected, as removing these configurations pushes away the tRVB state from the $\mathbb{Z}_3$ toric code fixed point, for which $\xi = 0$. These results demonstrate that $\mathbb{Z}_3$ topological order is preserved. Although we did not study TN perturbations that lower the density of trimers, we expect a diluted version of this tRVB state to host a topologically ordered phase.

We now focus on the Rydberg model arising from the implementation explained above. For simplicity, we neglect interactions beyond the blockade, so that the effective Hamiltonian is the same as Eq. (5.14), with the caveat that all the states containing wedged trimers as in Fig. 5.4.3(b) are not included in the Hilbert space of diluted trimer coverings. The exact diagonalization of this restricted trimer model displays no evidence of an intermediate topological phase in the ground state, rather a single phase transition between a disordered phase and a plaquette phase can be identified. Therefore, we conclude that if such a phase exists it is extremely narrow. In fact, the topological entanglement entropy extracted from the finite size cluster 48 in Fig. 5.4.1 exhibits a peak approaching $\gamma = \ln 3$ that is much sharper than in the unrestricted model, as we

show in Fig. 5.4.4(b). The black lines are the ground state curves for γ in the restricted (solid line) and unrestricted (dashed line) trimer models. However, below we provide numerical evidence that this witness of $\mathbb{Z}_3$ topological order is stabilized by a dynamical preparation protocol regularly used in experiments [265].

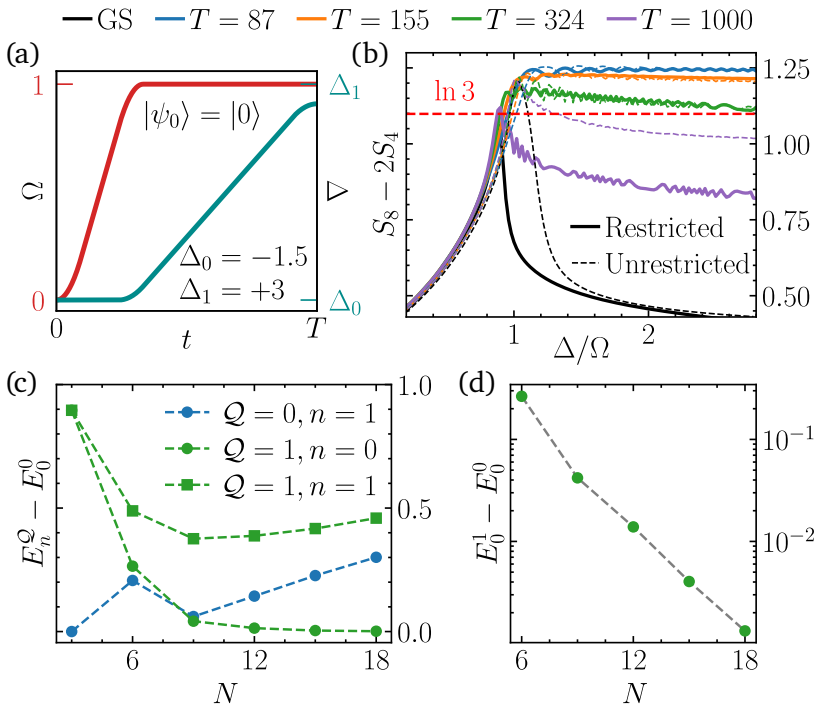

Figure 5.4.4: (a) The protocol employed for the semi-adiabatic dynamical preparation. The vacuum $|0\rangle$ is evolved with a time-dependent Hamiltonian with $\Delta(t)$ and $\Omega(t)$ as depicted in the figure. First, Ω is switched on from 0 to 1 at constant $\Delta = \Delta_0$ with a smoothed linear ramp. Δ is then increased linearly from $\Delta_0 = -1.5$ to $\Delta_1 = +3$ of constant Ω. The total sweep duration is T. (b) Topological entanglement entropy of the dynamically prepared state, for different preparation times. The black line corresponds to the ground state of the Hamiltonian Eq. (5.14) ($T = \infty$). Solid and dashed lines are obtained in the effective Rydberg model where the "wedged" trimer configuration of Fig. 5.4.3(b) are not included in the Hilbert space and the unrestricted diluted trimer model, respectively. Results are obtained on the periodic cluster 48 of Fig. 5.4.1. (c) $E = -\log\lambda$, where λ are the eigenvalues of the cylinder transfer matrix of the tensor network representation of the restricted tRVB state of bent trimers on the square lattice. N is the number of tensors along the circumference, $\mathcal{Q}$ is the $\mathbb{Z}_3$ virtual charge ($\mathcal{Q} = \pm 1$ sectors are exactly degenerate), n is the eigenvalue index in the sector with charge $\mathcal{Q}$. (d) Exponential scaling of the gap between the smallest Es in the neutral and charged sectors, signaling spontaneous symmetry breaking of the $\mathbb{Z}_3$ virtual symmetry of the tensor.

The initial state is the vacuum, subsequently evolved with the time-dependent Hamiltonian $H(t) = H(\Omega(t), \Delta(t))$. To prepare the ground state of $H(t)$ the variation of the time-dependent couplings has to be perfectly adiabatic. In real experiments, this is very hard in practice, due to limited coherence time. Thus it is often preferable to consider

non-adiabatic state preparation schemes. In fact, as demonstrated in Ref. [246, 265], non-adiabatic effects can even enhance topological order in the prepared state with respect to the ground state. In the following, we show that a similar result is observed here. Specifically, we study the dynamical preparation process depicted in Fig. 5.4.4(a). The vacuum state $|0\rangle$ is evolved with the time-dependent Hamiltonian $H(\Omega(t), \Delta(t))$, where $\Delta(0) = -2.5$, $\Omega(t) = 0$, such that $|0\rangle$ is the ground state at $t = 0$. A first (smoothed) linear ramp turns on the effective Rabi frequency until the final value $\Omega = 1$ is reached. The latter sets our units of energy and time. A second ramp is used to drive the detuning from $\Delta(0) = -1.5$ to $\Delta(T) = 3$, where T is the total sweep time, and the final value of Δ is chosen to be well beyond the peaks in tRVB overlap and topological entanglement entropy of the ground state. The slopes of the two ramps decrease with increasing T and are fixed by requiring that the switching on of Ω (Δ) takes $T/3$ ($2T/3$). In both the restricted and unrestricted models a phase transition is crossed during the second ramp.

In Fig. 5.4.4 we plot the topological entanglement entropy of the state during the preparation sweep, for different total sweep times T, for the 48 cluster in Fig. 5.4.1, that corresponds to 96 atoms in the mapping of Fig. 5.4.3(a). The result indicates that topological properties are stabilized in the prepared state when the preparation is *not* adiabatic, i.e. for short and intermediate T. Remarkably, the peaks in the topological entropy correction disappear in this regime, and the latter points to a topological state when $\Delta/\Omega \gtrsim 1$. For the largest Ts the ground state curve is recovered ($T = \infty$). We note that this phenomenon occurs in both the restricted and unrestricted models [cf. dash and solid lines in Fig. 5.4.4(b)].

We remark that it might be possible to engineer other implementations of the Hamiltonian in Eq. (5.14) that do not require a restriction of the diluted trimer Hilbert space.

5.5 Outlook

We showed that maximally-packed trimer states can be simple representatives of quantum spin liquids with $\mathbb{Z}_3$ topological order. By mapping trimer configurations into the Hilbert space of a lattice gauge theory, we identified a condition on the lattice geometry and trimer model that leads to the emergence of a $\mathrm{U}(1) \times \mathrm{U}(1)$ symmetry and a tRVB state with infinite correlation length. We verified this condition by performing numerical checks on several trimer models with TN methods. We demonstrated that when tRVB states are gapped, $\mathbb{Z}_3$ topological order is stable against fluctuations in the number of trimers. We did so by studying a TN perturbation that represents a diluted tRVB state on the square lattice and showing that it hosts a wide topologically ordered phase in the state phase diagram. Finally, we considered a simple model Hamiltonian on the square lattice that exhibits signatures of a tRVB-like phase, where the ground state is well approximated by the $\mathbb{Z}_3$ topologically ordered diluted TN perturbation previously studied. We provided an implementation of a very similar model by exploiting the blockade effect in Rydberg atom arrays, and show that hallmarks of a $\mathbb{Z}_3$ quantum spin liquid can be observed in non-adiabatic dynamical preparation schemes.

Our findings open new future directions for the quantum simulation of topological phases of matter. The necessary condition for having $\mathbb{Z}_3$ topological order that we formulated depends solely on the geometry of the model and can therefore guide the search for quantum spin liquids in various experimental implementations, including—but not limited to—Rydberg atom arrays. In this respect, it would be interesting to study more

extensively the realization of tRVB states both as ground states of realistic Hamiltonians and as dynamically-prepared non-equilibrium states. In addition, our approach can be naturally extended from trimer- to polymer-RVB states, which can support the emergence of $\mathbb{Z}_n$ topological order. A systematic study of such states can similarly be performed efficiently with tensor network methods and is left for future work. Finally, an interesting direction is the related problem of quantum spin liquid phases in $\mathrm{SU}(3)$ and $\mathrm{SU}(N)$ symmetric models. In certain models, trimers (polymers) can be interpreted as simplified versions of $\mathrm{SU}(3)$ ($\mathrm{SU}(N)$) spin singlets; it remains an open question to what extent this interpretation can be used to infer the properties of RVB states of singlets.

Appendices

5.A Details on the tensor-network representations

tRVB model on the square lattice

Symmetries

The tensor defined in Eq. (5.4) enjoys a reflection symmetry along the diagonal, which can be exploited in the CTMRG algorithm. The corresponding transfer operator is not self-adjoint, which requires one to compute both fixed points for the VUMPS algorithm. However, the fixed point in one direction can be readily converted into the the fixed point into the other direction, since

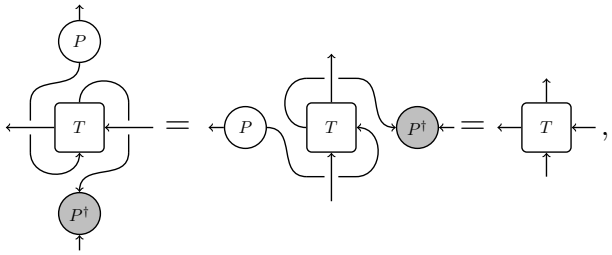

(5.16)

where P is the operator that permutes the ± 1 indices.

Diluted tRVB PEPS

The PEPS representation for the diluted tRVB in Eq. (5.9) is constructed by introducing two species of trimers; one that appear on the physical layer and ones that do not. Graphically, we have the following construction:

$|\Phi\rangle =$ 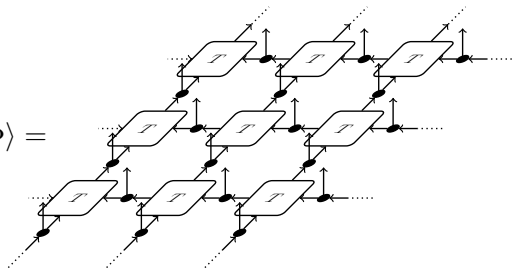 .

(5.17)

We label the indices of the tensor $\tilde{T}$ with $\{0, +1, -1, +\tilde{1}, -\tilde{1}\}$. We now have two pairs of uncoupled charges, each of which have the similar diagrams as Eq. (5.4). In order to preserve the correspondence with the partition function in Eq. (5.3), we must also take the square root of each weight. The black dot on each link represents a projector, which signals the presence of one type of trimer on the physical layer, and gives a fugacity contribution z to the second type

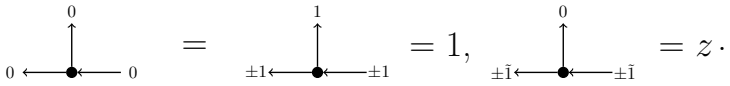

(5.18)

The corresponding PEPS tensor, formed by contracting one $\tilde{T}$ and two projectors, has bond dimension $D = 5$. It should be noted that the double-layer tensor—coming from

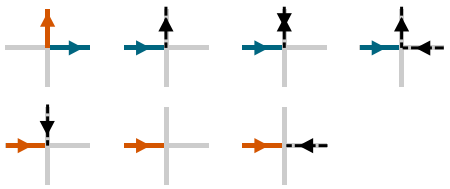

Figure 5.A.1: Allowed diagrams at each vertex for the restricted tRVB model, up to rotations of $\pi/2$.

the contraction of the norm $\langle\Phi|\Phi\rangle$—can be reduced to dimension 9 (instead of the naïvely expected 5^2). We observe this by performing Gaussian elimination on the tensor, which is exact up to numerical precision.

Restricted tRVB model

The mapping to Rydberg atoms in Sec. 5.4 suggests the ansatz state in which we restrict the trimer configurations to not have any "wedged" configurations, as shown in Fig. 5.4.3. We start from the arrow representation in Fig. 5.3.1(d), but we introduce new color labels

. (5.19)

Referring to Fig. 5.A.1, we start by labelling the two outgoing arrows of a bent trimer with different colors (blue and orange). To enforce the additional constraint, we introduce a dashed arrow which continues anticlockwise from the blue arrow. Notice that the arrow does not convey any charge information, as all dashed lines correspond to a $\mathbb{Z}_3$-charge 0. A vertex with the middle of the trimer cannot couple to it directly since it requires two gray lines. The other diagrams then account for the possible ways of closing the dashed lines. Accounting for rotations, in total there are 28 distinct diagrams.

The construction of the tensor network from Fig. 5.A.1 is straightforward, and is similar to Eq. (5.4). We must however remember that the mapping from the arrow representation to the index of the tensor is different if a leg of the tensor is ingoing or outgoing. Each leg of the double-layer tensor is then eight-dimensional.

tRVB model on the honeycomb lattice

On the honeycomb lattice there is only one type of trimer. On each vertex of the lattice we can place the tensor

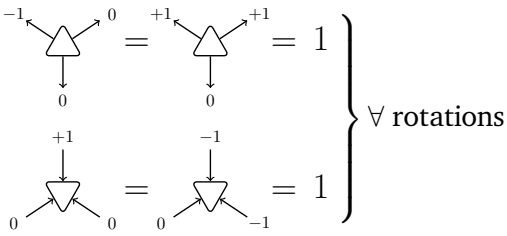

$\forall$ rotations (5.20)

to obtain the corresponding partition function. To convert the problem into a TN on the square lattice, we define the tensor

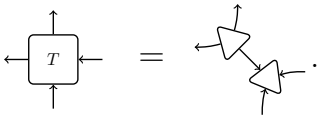

(5.21)

Similarly to the case of square lattice in Eq. (5.5), this tensor obeys a similar transformation: $(\sigma^\dagger \otimes \sigma^\dagger \otimes \sigma \otimes \sigma)T = \omega^2 T$.

tRVB model on the triangular lattice

On the triangular lattice an efficient TN representation can be found in the dual-lattice picture, where a site is defined on each triangular face, similarly to the way in which one would propose a Rydberg implementation. In this picture, only one site around each original vertex of the triangular lattice can be occupied. Correspondingly, in the TN picture we define a δ-tensor on each face, representing the site

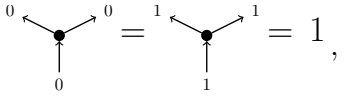

(5.22)

which is connected to three rank-6 constraint tensors

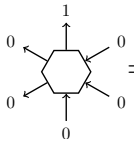

$\forall$ rotations. (5.23)

We can then bring the problem back to a TN contraction on the square lattice by first defining a decomposition of the constraint tensor

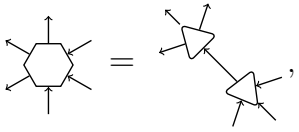

(5.24)

and performing the contraction

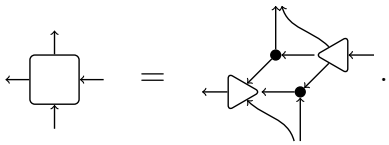

(5.25)

A conclusion is the place where you got tired of thinking.

M. H. Fisher [270]

CHAPTER 6

CONCLUSIONS AND OUTLOOK

The *leitmotif* of this thesis is the language of tensor networks. Using this framework, we have contributed to new methods for the study of many-body physics, and have applied well-established methods to study interesting physical systems. After having introduced the basic notions and having provided a brief overview of the field in Chapter 2, some works performed during this PhD have been presented. While the problems tackled are quite different, they are all difficult to solve with conventional methods. All touch upon open questions in quantum many-body systems, and hold an intrinsic interest of their own, such as describing equilibrium states, especially in case of frustration, long-range interactions or higher dimensions, understanding non-equilibrium dynamics and examining non-trivial states of matter which do not have any classical counterpart.

In Chapter 3, we focused on equilibrium physics by constructing an alternative to the Gibbs ensemble. This ensemble can reproduce the local physics of the corresponding thermal state, and can be constructed variationally using tensor networks. Indeed, we investigated the numerical optimization of one-dimensional tensor networks for this purpose. More generally, this method is applicable in cases where the von Neumann entropy is hard to estimate but the Rényi entropies are readily available. This could be applicable for example to neural network representations of quantum states [269]. As we mentioned in Chapter 1, connections between machine learning techniques and tensor networks have been explored in the last years. This connection works both ways. On one hand, the techniques developed for deep neural networks are being applied to construct powerful computational ansätze for many-body quantum systems [31, 269]. This is a promising direction for tackling challenging problems in higher dimensions, where tensor networks may be too costly to be competitive. On the other hand, the tensor network framework is being introduced to the machine learning community, and the connections with entanglement may assist in devising better methods and architectures in machine learning (see for example Refs. [30, 32]).

In Chapter 4, we explored tensor-network applications to a non-equilibrium setting. We studied the entanglement in the temporal direction in discrete integrable dynamics, and argued that integrable systems generally display a logarithmic growth. This sheds

light on the case of integrable dynamics, and unveils the unexpected role of interactions. Fully characterizing the origin of this slow growth of entanglement will lead to a better undestanding of the dynamics of integrable systems, but may also have consequences for more efficient numerical simulations. Indeed, as discussed in Sec. 2.5, conventional tensor-network schemes are limited by the linear growth of the spatial entanglement. At the same time, the long-time limit of local observables is typically described by thermal ensembles, which are themselves efficiently representable by tensor networks. This somewhat contradictory situation has sparked an ongoing effort to find new ways of avoiding the entanglement barrier and predicting the long-time behavior of local quantities, as this would be of great interest to probe and understand the onset of thermalization.

In Chapter 5, we explored the state composed of the superposition of all trimer configurations on different lattices. We demonstrated that these quantum states can host topological order, and connected them to $\mathbb{Z}_3$ lattice gauge theories. Building upon these results, we provided a simple model Hamiltonian with a topological trimer ground state, and devised an implementation of this model in Rydberg atom setups. Using exact numerical methods, we studied the experimental preparation of this state and showed that its topological nature can be captured on small-scale systems. Therefore, beyond the theoretical interest, these findings pave the way to the experimental realization of more complex forms of topological order. The latter is a crucial step towards the development of a fault-tolerant quantum computer.

More specific and technical conclusions can be found at the end of each respective chapter. Having come close to the end, we can take some distance and reflect on this work and the field in a broader context. Broadly speaking, this work lies at the intersection of many different branches of theoretical physics, chiefly condensed matter, quantum information theory and statistical physics. The modest contributions reported in this thesis can be seen as part of an emerging field, in which entanglement is not simply viewed as a feature of quantum physics, but as a tool to probe many-body phenomena. The realization of the existence of an area law of entaglement in gapped quantum systems has furnished firm theoretical justification for tensor network states. At the same time, it hints towards a holographic principle, and possible applications of tensor networks to study quantum field theory and quantum gravity. Although it is not clear if the expectations and promises that are attributed to tensor networks will all be fulfilled, the field can already boast several achievements, both from a numerical, as well as an analytical point of view.

On the numerical side, tensor networks have become the state-of-the-art tool to variationally approximate ground states in one dimension and, in the last years, a competitive method in two dimensions. Many technical aspects can still be improved; it remains to be seen what will yield practical speedups. Obtaining results in higher dimensions is much more challenging, as tensor network (at least the generalizations of MPS and PEPS) still suffer from their own form of a *curse of dimensionality*: as the connectivity increases, so does the number of parameters inside the tensors. While we expect that tensor networks may become a go-to numerical method for two-dimensional physics in the coming years, it is unlikely that this will be the case for three or more dimensions.

In parallel, tensor networks have become a tool for theoretically manipulating quantum systems and obtaining analytical results. Many theoretical achievements, such as

the classification of symmetry protected phases in one dimension can be understood in the language of tensor networks. In recent years, MPOs are being explored as algebraic elements, and interesting connections with fusion categories [271–273] and weak Hopf algebras [13] are being discovered. We would also like to conjecture that new theoretical insights are going to provide the input for new improved numerical algorithms. It is likely that many more exciting discoveries are just around the corner.

Bibliography

[1] G. Giudice, A. Çakan, J. I. Cirac, and M. C. Bañuls, *Rényi free energy and variational approximations to thermal states*, Physical Review B **103**, 205128 (2021).

[2] G. Giudice, G. Giudici, M. Sonner, J. Thoenniss, A. Lerose, D. A. Abanin, and L. Piroli, *Temporal Entanglement, Quasiparticles, and the Role of Interactions*, Physical Review Letters **128**, 220401 (2022).

[3] G. Giudice, F. M. Surace, H. Pichler, and G. Giudici, *Trimer states with Z_3 topological order in Rydberg atom arrays*, 2022, arXiv:2205.10387.

[4] E. Mascarenhas, G. Giudice, and V. Savona, *A Nonequilibrium quantum phase transition in strongly coupled spin chains*, Quantum **1**, 40 (2017).

[5] G. Giudici, A. Angelone, G. Magnifico, Z. Zeng, G. Giudice, T. Mendes-Santos, and M. Dalmonte, *Diagnosing Potts criticality and two-stage melting in one-dimensional hard-boson models*, Physical Review B **99**, 094434 (2019).

[6] N. Pancotti, G. Giudice, J. I. Cirac, J. P. Garrahan, and M. C. Bañuls, *Quantum East Model: Localization, Nonthermal Eigenstates, and Slow Dynamics*, Physical Review X **10**, 021051 (2020).

[7] P. A. M. Dirac, *Quantum mechanics of many-electron systems*, Proceedings of the Royal Society of London. Series A, Containing Papers of a Mathematical and Physical Character **123**, 714–733 (1929).

[8] A. L. Fetter and J. D. Walecka, *Quantum theory of many-particle systems* (Dover Publications, Mineola, N.Y, 2003).

[9] F. Franchini, *An introduction to integrable techniques for one-dimensional quantum systems*, Vol. 940, Lecture Notes in Physics (Springer International Publishing, Cham, 2017).

[10] V. Murg, V. E. Korepin, and F. Verstraete, *Algebraic Bethe ansatz and tensor networks*, Physical Review B **86**, 045125 (2012).

[11] J. Haegeman and F. Verstraete, *Diagonalizing Transfer Matrices and Matrix Product Operators: A Medley of Exact and Computational Methods*, Annual Review of Condensed Matter Physics **8**, 355–406 (2017).

[12] H. Dreyer, *Symmetries & tensor networks in two-dimensional quantum physics*, PhD thesis (Ludwig-Maximilians-Universität München, 2020).

[13] A. Molnar, A. R. de Alarcón, J. Garre-Rubio, N. Schuch, J. I. Cirac, and D. Pérez-García, *Matrix product operator algebras I: representations of weak Hopf algebras and projected entangled pair states*, 2022, arXiv:2204.05940.

[14] A. W. Sandvik, A. Avella, and F. Mancini, *Computational studies of quantum spin systems*, in Lectures on the Physics of Strongly Correlated Systems XIV (2010), pp. 135–338.

[15] M. Troyer and U.-J. Wiese, *Computational Complexity and Fundamental Limitations to Fermionic Quantum Monte Carlo Simulations*, Physical Review Letters **94**, 170201 (2005).

[16] J. C. Bridgeman and C. T. Chubb, *Hand-waving and interpretive dance: an introductory course on tensor networks*, Journal of Physics A: Mathematical and Theoretical **50**, 223001 (2017).

[17] J. I. Cirac, D. Pérez-García, N. Schuch, and F. Verstraete, *Matrix product states and projected entangled pair states: Concepts, symmetries, theorems*, Reviews of Modern Physics **93**, 045003 (2021).

[18] K. Okunishi, T. Nishino, and H. Ueda, *Developments in the Tensor Network — from Statistical Mechanics to Quantum Entanglement*, Journal of the Physical Society of Japan **91**, 062001 (2022).

[19] R. J. Baxter, *Dimers on a Rectangular Lattice*, Journal of Mathematical Physics **9**, 650–654 (1968).

[20] S. R. White, *Density matrix formulation for quantum renormalization groups*, Physical Review Letters **69**, 2863–2866 (1992).

[21] S. R. White, *Density-matrix algorithms for quantum renormalization groups*, Physical Review B **48**, 10345–10356 (1993).

[22] M. Fannes, B. Nachtergaele, and R. F. Werner, *Exact Antiferromagnetic Ground States of Quantum Spin Chains*, Europhysics Letters (EPL) **10**, 633–637 (1989).

[23] M. Fannes, B. Nachtergaele, and R. F. Werner, *Finitely correlated states on quantum spin chains*, Communications in Mathematical Physics **144**, 443–490 (1992).

[24] S. Östlund and S. Rommer, *Thermodynamic Limit of Density Matrix Renormalization*, Physical Review Letters **75**, 3537–3540 (1995).

[25] E. Schrödinger, *Discussion of Probability Relations between Separated Systems*, Mathematical Proceedings of the Cambridge Philosophical Society **31**, 555–563 (1935).

[26] T. G. Kolda and B. W. Bader, *Tensor Decompositions and Applications*, SIAM Review **51**, 455–500 (2009).

[27] I. V. Oseledets, *Tensor-Train Decomposition*, SIAM Journal on Scientific Computing **33**, 2295–2317 (2011).

[28] B. Derrida, M. R. Evans, V. Hakim, and V. Pasquier, *Exact solution of a 1D asymmetric exclusion model using a matrix formulation*, Journal of Physics A: Mathematical and General **26**, 1493–1517 (1993).

[29] P. Cvitanović, *Group theory: birdtracks, Lie's, and exceptional groups* (Princeton University Press, Princeton, N.J, 2008).

[30] E. Stoudenmire and D. J. Schwab, *Supervised learning with tensor networks*, in Advances in neural information processing systems, Vol. 29, edited by D. Lee, M. Sugiyama, U. Luxburg, I. Guyon, and R. Garnett (2016).

[31] G. Carleo, I. Cirac, K. Cranmer, L. Daudet, M. Schuld, N. Tishby, L. Vogt-Maranto, and L. Zdeborová, *Machine learning and the physical sciences*, Reviews of Modern Physics **91**, 045002 (2019).

[32] I. Glasser, N. Pancotti, and J. I. Cirac, *From Probabilistic Graphical Models to Generalized Tensor Networks for Supervised Learning*, IEEE Access **8**, 68169–68182 (2020).

[33] J. G. Bednorz and K. A. Müller, *Possible high Tc superconductivity in the Ba–La–Cu–O system*, Zeitschrift für Physik B Condensed Matter **64**, 189–193 (1986).

[34] B. Keimer, S. A. Kivelson, M. R. Norman, S. Uchida, and J. Zaanen, *From quantum matter to high-temperature superconductivity in copper oxides*, Nature **518**, 179–186 (2015).

[35] D. C. Tsui, H. L. Stormer, and A. C. Gossard, *Two-Dimensional Magnetotransport in the Extreme Quantum Limit*, Physical Review Letters **48**, 1559–1562 (1982).

[36] M. Endres, H. Bernien, A. Keesling, H. Levine, E. R. Anschuetz, A. Krajenbrink, C. Senko, V. Vuletic, M. Greiner, and M. D. Lukin, *Atom-by-atom assembly of defect-free one-dimensional cold atom arrays*, Science **354**, 1024–1027 (2016).

[37] D. Barredo, S. de Léséleuc, V. Lienhard, T. Lahaye, and A. Browaeys, *An atom-by-atom assembler of defect-free arbitrary two-dimensional atomic arrays*, Science **354**, 1021–1023 (2016).

[38] M. B. Hastings and T. Koma, *Spectral gap and exponential decay of correlations*, Communications in Mathematical Physics **265**, 781–804 (2006).

[39] R. Orús, *A practical introduction to tensor networks: matrix product states and projected entangled pair states*, Annals of Physics **349**, 117–158 (2014).

[40] М. Я. Бессараб, *Лев Ландау* (Октопус, 2008), Original text: Метод важнее открытия, ибо правильный метод исследования приведет к новым, еще более ценным открытиям.

[41] J.-P. Serre, *Linear Representations of Finite Groups*, Vol. 42, Graduate Texts in Mathematics (Springer New York, New York, NY, 1977).

[42] J. Haegeman, https://jutho.github.io/TensorKit.jl/.

[43] G. Sierra and T. Nishino, *The density matrix renormalization group method applied to interaction round a face Hamiltonians*, Nuclear Physics B **495**, 505–532 (1997).

[44] I. P. McCulloch and M. Gulácsi, *The non-Abelian density matrix renormalization group algorithm*, Europhysics Letters (EPL) **57**, 852–858 (2002).

[45] I. P. McCulloch, *From density-matrix renormalization group to matrix product states*, Journal of Statistical Mechanics: Theory and Experiment **2007**, P10014–P10014 (2007).

[46] S. Singh, R. N. C. Pfeifer, and G. Vidal, *Tensor network decompositions in the presence of a global symmetry*, Physical Review A **82**, 050301 (2010).

[47] S. Singh, R. N. C. Pfeifer, and G. Vidal, *Tensor network states and algorithms in the presence of a global U(1) symmetry*, Physical Review B **83**, 115125 (2011).

[48] B. Bauer, P. Corboz, R. Orús, and M. Troyer, *Implementing global Abelian symmetries in projected entangled-pair state algorithms*, Physical Review B **83**, 125106 (2011).

[49] S. Singh and G. Vidal, *Tensor network states and algorithms in the presence of a global SU(2) symmetry*, Physical Review B **86**, 195114 (2012).

[50] A. Weichselbaum, *Non-abelian symmetries in tensor networks: A quantum symmetry space approach*, Annals of Physics **327**, 2972–3047 (2012).

[51] L. S. Blackford, A. Petitet, R. Pozo, K. Remington, R. C. Whaley, J. Demmel, J. Dongarra, I. Duff, S. Hammarling, G. Henry, et al., *An updated set of basic linear algebra subprograms (BLAS)*, ACM Transactions on Mathematical Software **28**, 135–151 (2002).

[52] V. Strassen, *Gaussian elimination is not optimal*, Numerische Mathematik **13**, 354–356 (1969).

[53] N. Schuch, M. M. Wolf, F. Verstraete, and J. I. Cirac, *Computational Complexity of Projected Entangled Pair States*, Physical Review Letters **98**, 140506 (2007).

[54] C. Damm, M. Holzer, and P. McKenzie, *The complexity of tensor calculus*, Computational Complexity **11**, 54–89 (2002).

[55] R. N. C. Pfeifer, J. Haegeman, and F. Verstraete, *Faster identification of optimal contraction sequences for tensor networks*, Physical Review E **90**, 033315 (2014).

[56] J. Gray and S. Kourtis, *Hyper-optimized tensor network contraction*, Quantum **5**, 410 (2021).

[57] C. Eckart and G. Young, *The approximation of one matrix by another of lower rank*, Psychometrika **1**, 211–218 (1936).

[58] L. Mirsky, *Symmetric gauge functions and unitarily invariant norms*, The Quarterly Journal of Mathematics **11**, 50–59 (1960).

[59] E. Schmidt, *Zur Theorie der linearen und nicht linearen Integralgleichungen Zweite Abhandlung: Auflösung der allgemeinen linearen Integralgleichung*, Mathematische Annalen **64**, 161–174 (1907).

[60] G. W. Stewart, *On the Early History of the Singular Value Decomposition*, SIAM Review **35**, 551–566 (1993).

[61] H. Andrews and C. Patterson, *Singular Value Decomposition (SVD) Image Coding*, IEEE Transactions on Communications **24**, 425–432 (1976).

[62] R. Hennessy, https://unsplash.com/photos/xUUZcpQlqpM, Retrieved from Wikimedia Commons.

[63] P. Silvi, F. Tschirsich, M. Gerster, J. Jünemann, D. Jaschke, M. Rizzi, and S. Montangero, *The Tensor Networks Anthology: Simulation techniques for many-body quantum lattice systems*, SciPost Physics Lecture Notes, 8 (2019).

[64] P. Silvi, V. Giovannetti, S. Montangero, M. Rizzi, J. I. Cirac, and R. Fazio, *Homogeneous binary trees as ground states of quantum critical Hamiltonians*, Physical Review A **81**, 062335 (2010).

[65] G. Evenbly and G. Vidal, *Algorithms for Entanglement Renormalization: Boundaries, Impurities and Interfaces*, Journal of Statistical Physics **157**, 931–978 (2014).

[66] T. Barthel, M. Kliesch, and J. Eisert, *Real-Space Renormalization Yields Finite Correlations*, Physical Review Letters **105**, 010502 (2010).

[67] U. Schollwöck, *The density-matrix renormalization group in the age of matrix product states*, Annals of Physics **326**, 96–192 (2011).

[68] J. I. Cirac, *Entanglement in many-body quantum systems*, 2012, arXiv:1205.3742.

[69] M. B. Hastings, *An area law for one-dimensional quantum systems*, Journal of Statistical Mechanics: Theory and Experiment **2007**, P08024–P08024 (2007).

[70] A. Anshu, I. Arad, and D. Gosset, *An area law for 2d frustration-free spin systems*, in Proceedings of the 54th Annual ACM SIGACT Symposium on Theory of Computing (June 2022), pp. 12–18.

[71] F. Verstraete and J. I. Cirac, *Matrix product states represent ground states faithfully*, Physical Review B **73**, 094423 (2006).

[72] M. B. Hastings, *Solving gapped Hamiltonians locally*, Physical Review B **73**, 085115 (2006).

[73] Y. Huang, *Computing energy density in one dimension*, 2015, arXiv:1505.00772.

[74] R. P. Feynman, *Difficulties in Applying the Variational Principle to Quantum Field Theories*, in *Variational Calculations In Quantum Field Theory* (World Scientific, Singapore, July 1988), pp. 28–40.

[75] F. Verstraete, J. J. García-Ripoll, and J. I. Cirac, *Matrix product density operators: simulation of finite-temperature and dissipative systems*, Physical Review Letters **93**, 207204 (2004).

[76] M. Zwolak and G. Vidal, *Mixed-state dynamics in one-dimensional quantum lattice systems: a time-dependent superoperator renormalization algorithm*, Physical Review Letters **93**, 207205 (2004).

[77] B. Pirvu, V. Murg, J. I. Cirac, and F. Verstraete, *Matrix product operator representations*, New Journal of Physics **12**, 025012 (2010).

[78] G. M. Crosswhite and D. Bacon, *Finite automata for caching in matrix product algorithms*, Physical Review A **78**, 012356 (2008).

[79] M. M. Wolf, F. Verstraete, M. B. Hastings, and J. I. Cirac, *Area laws in quantum systems: mutual information and correlations*, Physical Review Letters **100**, 070502 (2008).

[80] T. Kuwahara, Á. M. Alhambra, and A. Anshu, *Improved thermal area law and quasilinear time algorithm for quantum Gibbs states*, Physical Review X **11**, 011047 (2021).

[81] A. Molnar, N. Schuch, F. Verstraete, and J. I. Cirac, *Approximating Gibbs states of local Hamiltonians efficiently with projected entangled pair states*, Physical Review B **91**, 045138 (2015).

[82] L. Onsager, *Crystal Statistics. I. A Two-Dimensional Model with an Order-Disorder Transition*, Physical Review **65**, 117–149 (1944).

[83] D. Perez-Garcia, F. Verstraete, J. Cirac, and M. Wolf, *PEPS as unique ground states of local Hamiltonians*, Quantum Information and Computation **8**, 650–663 (2008).

[84] P.-A. Absil, R. Mahony, and R. Sepulchre, *Optimization algorithms on matrix manifolds* (Princeton University Press, Princeton, N.J., 2008).

[85] J. Haegeman, M. Mariën, T. J. Osborne, and F. Verstraete, *Geometry of matrix product states: Metric, parallel transport, and curvature*, Journal of Mathematical Physics **55**, 021902 (2014).

[86] M. Hauru, M. Van Damme, and J. Haegeman, *Riemannian optimization of isometric tensor networks*, SciPost Physics **10**, 040 (2021).

[87] J. Haegeman, C. Lubich, I. Oseledets, B. Vandereycken, and F. Verstraete, *Unifying time evolution and optimization with matrix product states*, Physical Review B **94**, 165116 (2016).

[88] L. Vanderstraeten, J. Haegeman, and F. Verstraete, *Tangent-space methods for uniform matrix product states*, SciPost Physics Lecture Notes, 7 (2019).

[89] A. Edelman, T. A. Arias, and S. T. Smith, *The geometry of algorithms with orthogonality constraints*, SIAM Journal on Matrix Analysis and Applications **20**, 303–353 (1998).

[90] D. C. Liu and J. Nocedal, *On the limited memory BFGS method for large scale optimization*, Mathematical Programming **45**, 503–528 (1989).

[91] J. Nocedal and S. J. Wright, eds., *Numerical optimization*, Springer Series in Operations Research and Financial Engineering (Springer-Verlag, New York, 1999).

[92] R. Orús, *Tensor networks for complex quantum systems*, Nature Reviews Physics **1**, 538–550 (2019).

[93] M. C. Bañuls, *Tensor Network Algorithms: a Route Map*, 2022, arXiv:2205.10345.

[94] J. Dukelsky, M. A. Martín-Delgado, T. Nishino, and G. Sierra, *Equivalence of the variational matrix product method and the density matrix renormalization group applied to spin chains*, Europhysics Letters (EPL) **43**, 457–462 (1998).

[95] I. P. McCulloch, *Infinite size density matrix renormalization group, revisited*, 2008, arXiv:0804.2509.

[96] G. M. Crosswhite, A. C. Doherty, and G. Vidal, *Applying matrix product operators to model systems with long-range interactions*, Physical Review B **78**, 035116 (2008).

[97] V. Zauner-Stauber, L. Vanderstraeten, M. T. Fishman, F. Verstraete, and J. Haegeman, *Variational optimization algorithms for uniform matrix product states*, Physical Review B **97**, 045145 (2018).

[98] S. Paeckel, T. Köhler, A. Swoboda, S. R. Manmana, U. Schollwöck, and C. Hubig, *Time-evolution methods for matrix-product states*, Annals of Physics **411**, 167998 (2019).

[99] G. Vidal, *Efficient classical simulation of slightly entangled quantum computations*, Physical Review Letters **91**, 147902 (2003).

[100] P. Calabrese and J. Cardy, *Evolution of entanglement entropy in one-dimensional systems*, Journal of Statistical Mechanics: Theory and Experiment **2005**, P04010 (2005).

[101] M. Fagotti and P. Calabrese, *Evolution of entanglement entropy following a quantum quench: Analytic results for the X Y chain in a transverse magnetic field*, Physical Review A **78**, 010306 (2008).

[102] T. J. Osborne, *Efficient Approximation of the Dynamics of One-Dimensional Quantum Spin Systems*, Physical Review Letters **97**, 157202 (2006).

[103] M. C. Bañuls, M. B. Hastings, F. Verstraete, and J. I. Cirac, *Matrix Product States for Dynamical Simulation of Infinite Chains*, Physical Review Letters **102**, 240603 (2009).

[104] J. Haferkamp, D. Hangleiter, J. Eisert, and M. Gluza, *Contracting projected entangled pair states is average-case hard*, Physical Review Research **2**, 013010 (2020).

[105] B.-X. Zheng, C.-M. Chung, P. Corboz, G. Ehlers, M.-P. Qin, R. M. Noack, H. Shi, S. R. White, S. Zhang, and G. K.-L. Chan, *Stripe order in the underdoped region of the two-dimensional Hubbard model*, Science **358**, 1155–1160 (2017).

[106] P. C. G. Vlaar and P. Corboz, *Simulation of three-dimensional quantum systems with projected entangled-pair states*, Physical Review B **103**, 205137 (2021).

[107] V. Murg, F. Verstraete, and J. I. Cirac, *Variational study of hard-core bosons in a two-dimensional optical lattice using projected entangled pair states*, Physical Review A **75**, 033605 (2007).

[108] T. Nishino and K. Okunishi, *Corner Transfer Matrix Renormalization Group Method*, Journal of the Physical Society of Japan **65**, 891–894 (1996).

[109] H. C. Jiang, Z. Y. Weng, and T. Xiang, *Accurate determination of tensor network state of quantum lattice models in two dimensions*, Physical Review Letters **101**, 090603 (2008).

[110] J. Jordan, R. Orús, G. Vidal, F. Verstraete, and J. I. Cirac, *Classical simulation of infinite-size quantum lattice systems in two spatial dimensions*, Physical Review Letters **101**, 250602 (2008).

[111] M. Lubasch, J. I. Cirac, and M.-C. Bañuls, *Algorithms for finite projected entangled pair states*, Physical Review B **90**, 064425 (2014).

[112] H. N. Phien, J. A. Bengua, H. D. Tuan, P. Corboz, and R. Orús, *Infinite projected entangled pair states algorithm improved: Fast full update and gauge fixing*, Physical Review B **92**, 035142 (2015).

[113] H. N. Phien, I. P. McCulloch, and G. Vidal, *Fast convergence of imaginary time evolution tensor network algorithms by recycling the environment*, Physical Review B **91**, 115137 (2015).

[114] P. Corboz, *Variational optimization with infinite projected entangled-pair states*, Physical Review B **94**, 035133 (2016).

[115] L. Vanderstraeten, J. Haegeman, P. Corboz, and F. Verstraete, *Gradient methods for variational optimization of projected entangled-pair states*, Physical Review B **94**, 155123 (2016).

[116] A. G. Baydin, B. A. Pearlmutter, A. A. Radul, and J. M. Siskind, *Automatic differentiation in machine learning: a survey*, Journal of Machine Learning Research **18**, 1–43 (2018).

[117] H.-J. Liao, J.-G. Liu, L. Wang, and T. Xiang, *Differentiable Programming Tensor Networks*, Physical Review X **9**, 031041 (2019).

[118] J. Hasik, *Towards next-generation methods to optimize two-dimensional tensor networks: Algorithmic differentiation and applications to quantum magnets*, PhD thesis (SISSA, Trieste, 2019).

[119] E. T. Jaynes, *Information theory and statistical mechanics*, Physical Review **106**, 620–630 (1957).

[120] E. T. Jaynes, *Information theory and statistical mechanics. II*, Physical Review **108**, 171–190 (1957).

[121] J. Guth Jarkovský, A. Molnár, N. Schuch, and J. I. Cirac, *Efficient description of many-body systems with matrix product density operators*, PRX Quantum **1**, 010304 (2020).

[122] A. E. Feiguin and S. R. White, *Finite-temperature density matrix renormalization using an enlarged Hilbert space*, Physical Review B **72**, 220401 (2005).

[123] B.-B. Chen, Y.-J. Liu, Z. Chen, and W. Li, *Series-expansion thermal tensor network approach for quantum lattice models*, Physical Review B **95**, 161104 (2017).

[124] B.-B. Chen, L. Chen, Z. Chen, W. Li, and A. Weichselbaum, *Exponential thermal tensor network approach for quantum lattice models*, Physical Review X **8**, 031082 (2018).

[125] S. R. White, *Minimally entangled typical quantum states at finite temperature*, Physical Review Letters **102**, 190601 (2009).

[126] E. M. Stoudenmire and S. R. White, *Minimally entangled typical thermal state algorithms*, New Journal of Physics **12**, 055026 (2010).

[127] T. Nishino, *Density matrix renormalization group method for 2D classical models*, Journal of the Physical Society of Japan **64**, 3598–3601 (1995).

[128] R. J. Bursill, T. Xiang, and G. A. Gehring, *The density matrix renormalization group for a quantum spin chain at non-zero temperature*, Journal of Physics: Condensed Matter **8**, L583–L590 (1996).

[129] X. Wang and T. Xiang, *Transfer-matrix density-matrix renormalization-group theory for thermodynamics of one-dimensional quantum systems*, Physical Review B **56**, 5061–5064 (1997).

[130] P. Czarnik, L. Cincio, and J. Dziarmaga, *Projected entangled pair states at finite temperature: imaginary time evolution with ancillas*, Physical Review B **86**, 245101 (2012).

[131] P. Czarnik and J. Dziarmaga, *Fermionic projected entangled pair states at finite temperature*, Physical Review B **90**, 035144 (2014).

[132] A. Kshetrimayum, M. Rizzi, J. Eisert, and R. Orús, *Tensor network annealing algorithm for two-dimensional thermal states*, Physical Review Letters **122**, 070502 (2019).

[133] A. Rényi, *On measures of entropy and information*, in Proceedings of the Fourth Berkeley Symposium on Mathematical Statistics and Probability, Volume 1: Contributions to the Theory of Statistics (1961).

[134] A. Bashkirov, *Maximum Rényi entropy principle for systems with power-law Hamiltonians*, Physical Review Letters **93**, 130601 (2004).

[135] D. C. Brody, I. R. Buckley, and I. C. Constantinou, *Option price calibration from Rényi entropy*, Physics Letters A **366**, 298–307 (2007).

[136] C. Bunte and A. Lapidoth, *Maximizing Rényi entropy rate*, in 2014 IEEE 28th Convention of Electrical & Electronics Engineers in Israel (IEEEI) (2014), pp. 1–4.

[137] Y. Y. Atas and E. Bogomolny, *Spectral density of a one-dimensional quantum Ising model: Gaussian and multi-Gaussian approximations*, Journal of Physics A: Mathematical and Theoretical **47**, 335201 (2014).

[138] L. D. Landau and E. M. Lifshitz, *Statistical physics, Part 1*, 3. ed, Course of Theoretical Physics Vol. 5 (Butterworth Heinemann, Oxford, 1991).

[139] H. Touchette, *Equivalence and nonequivalence of the microcanonical and canonical ensembles: a large deviations study*, PhD thesis (McGill University, Montréal, Québec, Canada, 2003).

[140] R. S. Ellis, H. Touchette, and B. Turkington, *Thermodynamic versus statistical nonequivalence of ensembles for the mean-field Blume–Emery–Griffiths model*, Physica A: Statistical Mechanics and its Applications **335**, 518–538 (2004).

[141] G. De Las Cuevas, N. Schuch, D. Pérez-García, and J. Ignacio Cirac, *Purifications of multipartite states: limitations and constructive methods*, New Journal of Physics **15**, 123021 (2013).

[142] M. Kliesch, C. Gogolin, M. J. Kastoryano, A. Riera, and J. Eisert, *Locality of temperature*, Physical Review X **4**, 031019 (2014).

[143] G. De las Cuevas, T. S. Cubitt, J. I. Cirac, M. M. Wolf, and D. Pérez-García, *Fundamental limitations in the purifications of tensor networks*, Journal of Mathematical Physics **57**, 071902 (2016).

[144] J. Cui, J. I. Cirac, and M. C. Bañuls, *Variational matrix product operators for the steady state of dissipative quantum systems*, Physical Review Letters **114**, 220601 (2015).

[145] E. Mascarenhas, H. Flayac, and V. Savona, *Matrix-product-operator approach to the nonequilibrium steady state of driven-dissipative quantum arrays*, Physical Review A **92**, 022116 (2015).

[146] A. H. Werner, D. Jaschke, P. Silvi, M. Kliesch, T. Calarco, J. Eisert, and S. Montangero, *Positive tensor network approach for simulating open quantum many-body systems*, Physical Review Letters **116**, 237201 (2016).

[147] S. Katsura, *Statistical mechanics of the anisotropic linear Heisenberg model*, Physical Review **127**, 1508–1518 (1962).

[148] T. Niemeijer, *Some exact calculations on a chain of spins*, Physica **36**, 377–419 (1967).

[149] L. Tagliacozzo, T. R. de Oliveira, S. Iblisdir, and J. I. Latorre, *Scaling of entanglement support for matrix product states*, Physical Review B **78**, 024410 (2008).

[150] F. Pollmann, S. Mukerjee, A. M. Turner, and J. E. Moore, *Theory of finite-entanglement scaling at one-dimensional quantum critical points*, Physical Review Letters **102**, 255701 (2009).

[151] B. Pirvu, G. Vidal, F. Verstraete, and L. Tagliacozzo, *Matrix product states for critical spin chains: finite-size versus finite-entanglement scaling*, Physical Review B **86**, 075117 (2012).

[152] A. M. Läuchli, *Operator content of real-space entanglement spectra at conformal critical points*, 2013, arXiv:1303.0741.

[153] T. Shi, E. Demler, and J. I. Cirac, *Variational approach for many-body systems at finite temperature*, Physical Review Letters **125**, 180602 (2020).

[154] F. Verstraete, D. Porras, and J. I. Cirac, *Density matrix renormalization group and periodic boundary conditions: a quantum information perspective*, Physical Review Letters **93**, 227205 (2004).

[155] N. Yoshioka and R. Hamazaki, *Constructing neural stationary states for open quantum many-body systems*, Physical Review B **99**, 214306 (2019).

[156] M. J. Hartmann and G. Carleo, *Neural-network approach to dissipative quantum many-body dynamics*, Physical Review Letters **122**, 250502 (2019).

[157] A. Nagy and V. Savona, *Variational quantum monte carlo method with a neural-network ansatz for open quantum systems*, Physical Review Letters **122**, 250501 (2019).

[158] F. Vicentini, A. Biella, N. Regnault, and C. Ciuti, *Variational neural-network ansatz for steady states in open quantum systems*, Physical Review Letters **122**, 250503 (2019).

[159] M. Hartmann and O. Hess, *Gaussian quantum fluctuations in interacting many particle systems*, Letters in Mathematical Physics **68**, 103–112 (2004).

[160] M. Hartmann, G. Mahler, and O. Hess, *Spectral densities and partition functions of modular quantum systems as derived from a central limit theorem*, Journal of Statistical Physics **119**, 1139–1151 (2005).

[161] J. Keating, N. Linden, and H. Wells, *Spectra and eigenstates of spin chain Hamiltonians*, Communications in Mathematical Physics **338**, 81–102 (2015).

[162] S. R. White and A. E. Feiguin, *Real-Time Evolution Using the Density Matrix Renormalization Group*, Physical Review Letters **93**, 076401 (2004).

[163] D. Perez-Garcia, F. Verstraete, M. Wolf, and J. Cirac, *Matrix product state representations*, Quantum Information and Computation **7**, 401–430 (2007).

[164] A. J. Daley, C. Kollath, U. Schollwöck, and G. Vidal, *Time-dependent density-matrix renormalization-group using adaptive effective Hilbert spaces*, Journal of Statistical Mechanics: Theory and Experiment **2004**, P04005 (2004).

[165] G. Vidal, *Classical Simulation of Infinite-Size Quantum Lattice Systems in One Spatial Dimension*, Physical Review Letters **98**, 070201 (2007).

[166] R. Orús and G. Vidal, *Infinite time-evolving block decimation algorithm beyond unitary evolution*, Physical Review B **78**, 155117 (2008).

[167] N. Schuch, M. M. Wolf, K. G. H. Vollbrecht, and J. I. Cirac, *On entropy growth and the hardness of simulating time evolution*, New Journal of Physics **10**, 033032 (2008).

[168] A. Polkovnikov, K. Sengupta, A. Silva, and M. Vengalattore, *Colloquium: Nonequilibrium dynamics of closed interacting quantum systems*, Reviews of Modern Physics **83**, 863–883 (2011).

[169] A. Müller-Hermes, J. Ignacio Cirac, and M. C. Bañuls, *Tensor network techniques for the computation of dynamical observables in one-dimensional quantum spin systems*, New Journal of Physics **14**, 075003 (2012).

[170] M. B. Hastings and R. Mahajan, *Connecting entanglement in time and space: Improving the folding algorithm*, Physical Review A **91**, 032306 (2015).

[171] M. Frías-Pérez and M. C. Bañuls, *Light cone tensor network and time evolution*, 2022, arXiv:2201.08402.

[172] A. Lerose, M. Sonner, and D. A. Abanin, *Influence Matrix Approach to Many-Body Floquet Dynamics*, Physical Review X **11**, 021040 (2021).

[173] M. Akila, D. Waltner, B. Gutkin, and T. Guhr, *Particle-time duality in the kicked Ising spin chain*, Journal of Physics A: Mathematical and Theoretical **49**, 375101 (2016).

[174] B. Bertini, P. Kos, and T. Prosen, *Entanglement Spreading in a Minimal Model of Maximal Many-Body Quantum Chaos*, Physical Review X **9**, 021033 (2019).

[175] B. Bertini, P. Kos, and T. Prosen, *Exact Correlation Functions for Dual-Unitary Lattice Models in 1 + 1 Dimensions*, Physical Review Letters **123**, 210601 (2019).

[176] B. Bertini and L. Piroli, *Scrambling in random unitary circuits: Exact results*, Physical Review B **102**, 064305 (2020).

[177] P. W. Claeys and A. Lamacraft, *Maximum velocity quantum circuits*, Physical Review Research **2**, 033032 (2020).

[178] L. Piroli, B. Bertini, J. I. Cirac, and T. Prosen, *Exact dynamics in dual-unitary quantum circuits*, Physical Review B **101**, 094304 (2020).

[179] I. Reid and B. Bertini, *Entanglement barriers in dual-unitary circuits*, Physical Review B **104**, 014301 (2021).

[180] J. Cotler, C.-M. Jian, X.-L. Qi, and F. Wilczek, *Superdensity operators for spacetime quantum mechanics*, Journal of High Energy Physics **2018**, 93 (2018).

[181] T.-C. Lu and T. Grover, *Spacetime duality between localization transitions and measurement-induced transitions*, PRX Quantum **2**, 040319 (2021).

[182] S. J. Garratt and J. T. Chalker, *Many-Body Delocalization as Symmetry Breaking*, Physical Review Letters **127**, 026802 (2021).

[183] M. Ippoliti and V. Khemani, *Postselection-Free Entanglement Dynamics via Spacetime Duality*, Physical Review Letters **126**, 060501 (2021).

[184] T.-G. Zhou, Y.-N. Zhou, P. Zhang, and H. Zhai, *Space-time duality between quantum chaos and non-Hermitian boundary effect*, Physical Review Research **4**, L022039 (2022).

[185] M. Ippoliti, T. Rakovszky, and V. Khemani, *Fractal, Logarithmic, and Volume-Law Entangled Nonthermal Steady States via Spacetime Duality*, Physical Review X **12**, 011045 (2022).

[186] E. Ye and G. K.-L. Chan, *Constructing tensor network influence functionals for general quantum dynamics*, The Journal of Chemical Physics **155**, 044104 (2021).

[187] A. Lerose, M. Sonner, and D. A. Abanin, *Scaling of temporal entanglement in proximity to integrability*, Physical Review B **104**, 035137 (2021).

[188] M. Sonner, A. Lerose, and D. A. Abanin, *Influence functional of many-body systems: Temporal entanglement and matrix-product state representation*, **435**, 168552 (2021).

[189] M. Sonner, A. Lerose, and D. A. Abanin, *Characterizing many-body localization via exact disorder-averaged quantum noise*, Physical Review B **105**, L020203 (2022).

[190] A. Lerose, M. Sonner, and D. A. Abanin, *Overcoming the entanglement barrier in quantum many-body dynamics via space-time duality*, 2022, arXiv:2201.04150.

[191] B. Bertini, P. Kos, and T. Prosen, *Exact Spectral Form Factor in a Minimal Model of Many-Body Quantum Chaos*, Physical Review Letters **121**, 264101 (2018).

[192] K. Klobas and B. Bertini, *Entanglement dynamics in Rule 54: Exact results and quasiparticle picture*, SciPost Physics **11**, 107 (2021).

[193] K. Klobas, B. Bertini, and L. Piroli, *Exact Thermalization Dynamics in the "Rule 54" Quantum Cellular Automaton*, Physical Review Letters **126**, 160602 (2021).

[194] K. Klobas and B. Bertini, *Exact relaxation to Gibbs and non-equilibrium steady states in the quantum cellular automaton Rule 54*, SciPost Physics **11**, 106 (2021).

[195] P. Calabrese, F. H. L. Essler, and G. Mussardo, *Introduction to 'Quantum Integrability in Out of Equilibrium Systems'*, Journal of Statistical Mechanics: Theory and Experiment **2016**, 064001 (2016).

[196] F. H. L. Essler and M. Fagotti, *Quench dynamics and relaxation in isolated integrable quantum spin chains*, Journal of Statistical Mechanics: Theory and Experiment **2016**, 064002 (2016).

[197] J.-S. Caux, *The Quench Action*, Journal of Statistical Mechanics: Theory and Experiment **2016**, 064006 (2016).

[198] M. Vanicat, L. Zadnik, and T. Prosen, *Integrable Trotterization: Local Conservation Laws and Boundary Driving*, Physical Review Letters **121**, 030606 (2018).

[199] M. Ljubotina, L. Zadnik, and T. Prosen, *Ballistic Spin Transport in a Periodically Driven Integrable Quantum System*, Physical Review Letters **122**, 150605 (2019).

[200] P. Calabrese and J. Cardy, *Entanglement entropy and conformal field theory*, Journal of Physics A: Mathematical and Theoretical **42**, 504005 (2009).

[201] V. Alba and P. Calabrese, *Entanglement and thermodynamics after a quantum quench in integrable systems*, Proceedings of the National Academy of Sciences **114**, 7947–7951 (2017).

[202] V. Alba and P. Calabrese, *Entanglement dynamics after quantum quenches in generic integrable systems*, SciPost Physics **4**, 017 (2018).

[203] I. L. Aleiner, *Bethe Ansatz solutions for certain Periodic Quantum Circuits*, Annals of Physics **433**, 168593 (2021).

[204] P. W. Claeys and A. Lamacraft, *Ergodic and Nonergodic Dual-Unitary Quantum Circuits with Arbitrary Local Hilbert Space Dimension*, Physical Review Letters **126**, 100603 (2021).

[205] V. E. Korepin, N. M. Bogoliubov, and A. G. Izergin, *Quantum inverse scattering method and correlation functions*, Vol. 3 (Cambridge University Press, Cambridge, England, 1997).

[206] M. A. Nielsen and I. Chuang, *Quantum computation and quantum information* (Cambridge University Press, Cambridge, England, 2002).

[207] V. Alba, J. Dubail, and M. Medenjak, *Operator entanglement in interacting integrable quantum systems: the case of the Rule 54 chain*, Physical Review Letters **122**, 250603 (2019).

[208] R. Modak, L. Piroli, and P. Calabrese, *Correlation and entanglement spreading in nested spin chains*, Journal of Statistical Mechanics: Theory and Experiment **2019**, 093106 (2019).

[209] G. Lagnese, P. Calabrese, and L. Piroli, *Entanglement dynamics of thermofield double states in integrable models*, Journal of Physics A: Mathematical and Theoretical **55**, 214003 (2022).

[210] L. Piroli, B. Pozsgay, and E. Vernier, *What is an integrable quench?*, Nuclear Physics B **925**, 362–402 (2017).

[211] B. Pozsgay, L. Piroli, and E. Vernier, *Integrable Matrix Product States from boundary integrability*, SciPost Physics **6**, 062 (2019).

[212] B. Bertini, E. Tartaglia, and P. Calabrese, *Entanglement and diagonal entropies after a quench with no pair structure*, Journal of Statistical Mechanics: Theory and Experiment **2018**, 063104 (2018).

[213] A. Bastianello and P. Calabrese, *Spreading of entanglement and correlations after a quench with intertwined quasiparticles*, SciPost Physics **5**, 033 (2018).

[214] L. Piroli, B. Pozsgay, and E. Vernier, *From the quantum transfer matrix to the quench action: the Loschmidt echo in XXZ Heisenberg spin chains*, Journal of Statistical Mechanics: Theory and Experiment **2017**, 023106 (2017).

[215] L. Piroli, B. Pozsgay, and E. Vernier, *Non-analytic behavior of the Loschmidt echo in XXZ spin chains: Exact results*, Nuclear Physics B **933**, 454–481 (2018).

[216] J. Haegeman, https://github.com/Jutho/TensorKit.jl.

[217] P. Zanardi, *Entanglement of quantum evolutions*, Physical Review A **63**, 040304 (2001).

[218] T. Prosen and I. Pižorn, *Operator space entanglement entropy in a transverse Ising chain*, Physical Review A **76**, 032316 (2007).

[219] T. Prosen and M. Žnidarič, *Is the efficiency of classical simulations of quantum dynamics related to integrability?*, Physical Review E **75**, 015202 (2007).

[220] I. Pižorn and T. Prosen, *Operator space entanglement entropy in X Y spin chains*, Physical Review B **79**, 184416 (2009).

[221] J. Dubail, *Entanglement scaling of operators: a conformal field theory approach, with a glimpse of simulability of long-time dynamics in 1 + 1d*, Journal of Physics A: Mathematical and Theoretical **50**, 234001 (2017).

[222] B. Bertini, P. Kos, and T. Prosen, *Operator Entanglement in Local Quantum Circuits I: Chaotic Dual-Unitary Circuits*, SciPost Physics **8**, 067 (2020).

[223] B. Bertini, P. Kos, and T. Prosen, *Operator Entanglement in Local Quantum Circuits II: Solitons in Chains of Qubits*, SciPost Physics **8**, 068 (2020).

[224] V. Alba, *Diffusion and operator entanglement spreading*, Physical Review B **104**, 094410 (2021).

[225] F. Verstraete and J. I. Cirac, *Continuous Matrix Product States for Quantum Fields*, Physical Review Letters **104**, 190405 (2010).

[226] W. Tang, H.-H. Tu, and L. Wang, *Continuous Matrix Product Operator Approach to Finite Temperature Quantum States*, Physical Review Letters **125**, 170604 (2020).

[227] J. I. Latorre, E. Rico, and G. Vidal, *Ground state entanglement in quantum spin chains*, Quantum Info. Comput. **4**, 48–92 (2004).

[228] S. Gopalakrishnan and A. Lamacraft, *Unitary circuits of finite depth and infinite width from quantum channels*, Physical Review B **100**, 064309 (2019).

[229] R. Moessner and K. S. Raman, *Quantum Dimer Models*, in *Introduction to Frustrated Magnetism*, Vol. 164, edited by C. Lacroix, P. Mendels, and F. Mila (Springer, Berlin, Heidelberg, 2011), pp. 437–479.

[230] R. Moessner and S. L. Sondhi, *Resonating valence bond phase in the triangular lattice quantum dimer model*, Physical Review Letters **86**, 1881–1884 (2001).

[231] H. Lee, Y.-t. Oh, J. H. Han, and H. Katsura, *Resonating valence bond states with trimer motifs*, Physical Review B **95**, 060413 (2017).

[232] X.-Y. Dong, J.-Y. Chen, and H.-H. Tu, *SU(3) trimer resonating-valence-bond state on the square lattice*, Physical Review B **98**, 205117 (2018).

[233] S. Jandura, M. Iqbal, and N. Schuch, *Quantum trimer models and topological SU(3) spin liquids on the kagome lattice*, Physical Review Research **2**, 033382 (2020).

[234] Z.-C. Yang, D. Green, H. Yu, and C. Chamon, *Z 3 Quantum Double in a Superconducting Wire Array*, PRX Quantum **2**, 030327 (2021).

[235] F. Verstraete, V. Murg, and J. Cirac, *Matrix product states, projected entangled pair states, and variational renormalization group methods for quantum spin systems*, Advances in Physics **57**, 143–224 (2008).

[236] K. Duivenvoorden, M. Iqbal, J. Haegeman, F. Verstraete, and N. Schuch, *Entanglement phases as holographic duals of anyon condensates*, Physical Review B **95**, 235119 (2017).

[237] R. J. Baxter, *Exactly solved models in statistical mechanics*, in *Series on advances in statistical mechanics* (World Scientific, May 1985), pp. 5–63.

[238] T. Nishino and K. Okunishi, *Corner Transfer Matrix Algorithm for Classical Renormalization Group*, Journal of the Physical Society of Japan **66**, 3040–3047 (1997).

[239] A. Gendiar, *Lattice models studied by numerical renormalization group approaches: Review of critical properties*, Acta Physica Slovaca **51**, 69–138 (2001).

[240] R. Orús and G. Vidal, *Simulation of two-dimensional quantum systems on an infinite lattice revisited: Corner transfer matrix for tensor contraction*, Physical Review B **80**, 094403 (2009).

[241] M. T. Fishman, L. Vanderstraeten, V. Zauner-Stauber, J. Haegeman, and F. Verstraete, *Faster methods for contracting infinite two-dimensional tensor networks*, Physical Review B **98**, 235148 (2018).

[242] C. Chatelain and A. Gendiar, *Absence of logarithmic divergence of the entanglement entropies at the phase transitions of a 2D classical hard rod model*, The European Physical Journal B **93**, 134 (2020).

[243] A. Kitaev and J. Preskill, *Topological entanglement entropy*, Physical Review Letters **96**, 110404 (2006).

[244] M. Levin and X.-G. Wen, *Detecting Topological Order in a Ground State Wave Function*, Physical Review Letters **96**, 110405 (2006).

[245] H. Dreyer, J. I. Cirac, and N. Schuch, *Projected entangled pair states with continuous virtual symmetries*, Physical Review B **98**, 115120 (2018).

[246] G. Giudici, M. D. Lukin, and H. Pichler, *Dynamical preparation of quantum spin liquids in Rydberg atom arrays*, 2022, arXiv:2201.04034.

[247] A. Y. Kitaev, *Fault-tolerant quantum computation by anyons*, Annals of Physics **303**, 2–30 (2003).

[248] N. Schuch, I. Cirac, and D. Perez-Garcia, *PEPS as ground states: degeneracy and topology*, Annals of Physics **325**, 2153–2192 (2010).

[249] N. Schuch, D. Poilblanc, J. I. Cirac, and D. Perez-Garcia, *Resonating valence bond states in the PEPS formalism*, Physical Review B **86**, 115108 (2012).

[250] J. Bricmont and J. Frölich, *An order parameter distinguishing between different phases of lattice gauge theories with matter fields*, Physics Letters B **122**, 73–77 (1983).

[251] K. Fredenhagen and M. Marcu, *Charged states in $\mathbb{Z}_2$ gauge theories*, Communications in Mathematical Physics **92**, 81–119 (1983).

[252] R. Verresen, M. D. Lukin, and A. Vishwanath, *Prediction of toric code topological order from rydberg blockade*, Physical Review X **11**, 031005 (2021).

[253] A. Polyakov, *Quark confinement and topology of gauge theories*, Nuclear Physics B **120**, 429–458 (1977).

[254] A. Verberkmoes and B. Nienhuis, *Bethe ansatz solution of triangular trimers on the triangular lattice*, Physical Review E: Statistical Physics, Plasmas, Fluids, and Related Interdisciplinary Topics **63**, 066122 (2001).

[255] G. Giudici, J. I. Cirac, and N. Schuch, *Locality optimization for parent Hamiltonians of tensor networks*, Physical Review B **106**, 035109 (2022).

[256] H. Weimer, M. Müller, I. Lesanovsky, P. Zoller, and H. P. Büchler, *A Rydberg quantum simulator*, Nature Physics **6**, 382–388 (2010).

[257] H. Labuhn, D. Barredo, S. Ravets, S. de Léséleuc, T. Macrì, T. Lahaye, and A. Browaeys, *Tunable two-dimensional arrays of single Rydberg atoms for realizing quantum Ising models*, Nature **534**, 667–670 (2016).

[258] H. Bernien, S. Schwartz, A. Keesling, H. Levine, A. Omran, H. Pichler, S. Choi, A. S. Zibrov, M. Endres, M. Greiner, V. Vuletić, and M. D. Lukin, *Probing many-body dynamics on a 51-Atom quantum simulator*, Nature **551**, 579–584 (2017).

[259] S. de Léséleuc, S. Weber, V. Lienhard, D. Barredo, H. P. Büchler, T. Lahaye, and A. Browaeys, *Accurate mapping of multilevel rydberg atoms on interacting spin-1/2 particles for the quantum simulation of Ising models*, Physical Review Letters **120**, 113602 (2018).

[260] H. Kim, Y. Park, K. Kim, H.-S. Sim, and J. Ahn, *Detailed balance of thermalization dynamics in Rydberg-atom quantum simulators*, Physical Review Letters **120**, 180502 (2018).

[261] P. Schauß, J. Zeiher, T. Fukuhara, S. Hild, M. Cheneau, T. Macrì, T. Pohl, I. Bloch, and C. Gross, *Crystallization in Ising quantum magnets*, Science **347**, 1455–1458 (2015).

[262] A. Browaeys and T. Lahaye, *Many-body physics with individually controlled Rydberg atoms*, Nature Physics **16**, 132–142 (2020).

[263] C. J. Turner, A. A. Michailidis, D. A. Abanin, M. Serbyn, and Z. Papić, *Weak ergodicity breaking from quantum many-body scars*, Nature Physics **14**, 745–749 (2018).

[264] F. M. Surace, P. P. Mazza, G. Giudici, A. Lerose, A. Gambassi, and M. Dalmonte, *Lattice Gauge Theories and String Dynamics in Rydberg Atom Quantum Simulators*, Physical Review X **10**, 021041 (2020).

[265] G. Semeghini, H. Levine, A. Keesling, S. Ebadi, T. T. Wang, D. Bluvstein, R. Verresen, H. Pichler, M. Kalinowski, R. Samajdar, A. Omran, S. Sachdev, A. Vishwanath, M. Greiner, V. Vuletić, and M. D. Lukin, *Probing topological spin liquids on a programmable quantum simulator*, Science (New York, N.Y.) **374**, 1242 (2021).

[266] S. Ebadi, T. T. Wang, H. Levine, A. Keesling, G. Semeghini, A. Omran, D. Bluvstein, R. Samajdar, H. Pichler, W. W. Ho, S. Choi, S. Sachdev, M. Greiner, V. Vuletić, and M. D. Lukin, *Quantum phases of matter on a 256-Atom programmable quantum simulator*, Nature **595**, 227–232 (2021).

[267] P. Scholl, M. Schuler, H. J. Williams, A. A. Eberharter, D. Barredo, K.-N. Schymik, V. Lienhard, L.-P. Henry, T. C. Lang, T. Lahaye, A. M. Läuchli, and A. Browaeys, *Quantum simulation of 2D antiferromagnets with hundreds of Rydberg atoms*, Nature **595**, 233–238 (2021).

[268] S. Ebadi, A. Keesling, M. Cain, T. T. Wang, H. Levine, D. Bluvstein, G. Semeghini, A. Omran, J.-G. Liu, R. Samajdar, X.-Z. Luo, B. Nash, X. Gao, B. Barak, E. Farhi, S. Sachdev, N. Gemelke, L. Zhou, S. Choi, H. Pichler, S.-T. Wang, M. Greiner, V. Vuletic, and M. D. Lukin, *Quantum optimization of maximum independent set using Rydberg atom arrays*, Science, eabo6587 (2022).

[269] G. Carleo and M. Troyer, *Solving the quantum many-body problem with artificial neural networks*, Science **355**, 602–606 (2017).

[270] D. Smith, *Encore: a continuing anthology*, Volume XIII (Encore Press, New York, 1945), From: https://en.wikiquote.org/wiki/Martin_H._Fischer.

[271] N. Bultinck, M. Mariën, D. Williamson, M. Şahinoğlu, J. Haegeman, and F. Verstraete, *Anyons and matrix product operator algebras*, Annals of Physics **378**, 183–233 (2017).

[272] M. B. Şahinoğlu, D. Williamson, N. Bultinck, M. Mariën, J. Haegeman, N. Schuch, and F. Verstraete, *Characterizing Topological Order with Matrix Product Operators*, Annales Henri Poincaré **22**, 563–592 (2021).

[273] L. Lootens, J. Fuchs, J. Haegeman, C. Schweigert, and F. Verstraete, *Matrix product operator symmetries and intertwiners in string-nets with domain walls*, SciPost Physics **10**, 053 (2021).

Acknowledgements

The works collected in this thesis are part of a long journey, which would not have been possible without the help and support of innumerable people I've met during these years. First and foremost, I would like to thank my supervisor Ignacio Cirac for his guidance during my PhD, and for giving me the freedom to pursue any direction I took interest in. His vast knowledge, insightful advice, and leadership have contributed in cultivating an amazing group. It was a priviledge and an honor to be part of it. I would also like to thank Mari Carmen Bañuls for being my mentor during this time. Thank you for your continued support, for always being available to discuss, and for reviewing this thesis. I am grateful as well to Michael Knap for kindly agreeing to act as referee for this thesis.

Almost everything I have learned in this journey is from my collaborators. In particular, I feel lucky to have crossed paths with Giuliano Giudici and Lorenzo Piroli. The gratifying collaborations taught me not only a lot about physics, but also how to become a well-rounded scientist.

This journey would not have even started without the encouragement of many people. I am indebted to Eduardo Mascarenhas and Vincenzo Savona, for leading me to discover tensor networks; to Noé Gallice, for the times shared during my studies—*t'es parti, mais on t'oublie pas*.

I would like to thank all the members of the theory group at the Max Planck Institute for Quantum Optics—past and present—for helping create a stimulating environment, where collaboration is valued over competition. For the fun conversations, the inspiring discussions, and the good times outside of work, I would like to thank in particular Flavio Baccari, Miguel Bello Gamboa, Julian Bender, Aslı Çakan, Denise Cocchiarella, Caroline de Groot, Henrik Dreyer, Albert Gasull Celades, Yimin Ge, Ivan Glasser, Alejandro Gonzáles Tudela, Tommaso Guaita, Jiří Guth Jarkovský, Anna Hackenbroich, Andrea Kluth, Johannes Knörzer, Marti Perarnau Llobet, András Molnár, Irene Papaefstathiou, Daniel Robaina Fernández, Julian Roos, David Sauerwein, Norbert Schuch, David Stephen, Antoine Sterdyniak, Cristoph Sünderhauf, Antoine Tilloy, Jordi Tura i Brugués, Dominik Wild and Erez Zohar. Special thanks goes to Patrick Emonts—the best office mate one could ever ask for—for the times shared in and out of the office.

A wholehearted *grazie* goes to *i ragazzi di Leopoldstraße* for the wonderful times in Munich, especially Nicola, for his perpetual optimism; Benzo, for being himself; Elena, for pushing me to finish this thesis; Vale, for always wanting to party; and Cosimo, for too many things to mention.

It is a pleasure to acknowledge the unwaivering support of my family: my parents, my brother, my grandfather in Italy and my grandparents in the States. Without you, I would not have been able to write a single word.

Finally, to Samantha, for walking all this way with me: *dziękuję, że jesteś*.